REPORT DOCUMENTATION PAGE

Form Approved OMB NO. 0704-0188

1. REPORT DATE (DD-MM-YYYY)	2. REPORT TYPE	3. DATES COVERED (From - To)
30-08-2023	Thesis or Dissertation	-

4. TITLE AND SUBTITLE
High Absorption per unit Thermal Mass Subwavelength Perforated Membrane as Uncooled Thermal Infrared Detector

5a. CONTRACT NUMBER
W911NF-18-1-0272

5b. GRANT NUMBER

5c. PROGRAM ELEMENT NUMBER
611102

6. AUTHORS
Avijit Das

5d. PROJECT NUMBER

5e. TASK NUMBER

5f. WORK UNIT NUMBER

7. PERFORMING ORGANIZATION NAMES AND ADDRESSES
University of Minnesota - Minneapolis
450 McNamara Alumni Center
200 Oak Street SE
Minnepolis, MN 55455 -2070

8. PERFORMING ORGANIZATION REPORT NUMBER

9. SPONSORING/MONITORING AGENCY NAME(S) AND ADDRESS (ES)
U.S. Army Research Office
P.O. Box 12211
Research Triangle Park, NC 27709-2211

10. SPONSOR/MONITOR'S ACRONYM(S)
ARO

11. SPONSOR/MONITOR'S REPORT NUMBER(S)
73234-PE.10

12. DISTRIBUTION AVAILIBILITY STATEMENT

13. SUPPLEMENTARY NOTES
The views, opinions and/or findings contained in this report are those of the author(s) and should not contrued as an official Department of the Army position, policy or decision, unless so designated by other documentation.

14. ABSTRACT

15. SUBJECT TERMS

16. SECURITY CLASSIFICATION OF:			17. LIMITATION OF ABSTRACT	15. NUMBER OF PAGES	19a. NAME OF RESPONSIBLE PERSON
a. REPORT	b. ABSTRACT	c. THIS PAGE			Joseph Talghader
					19b. TELEPHONE NUMBER 612-625-4524

REPORT DOCUMENTATION PAGE (SF298)
(Continuation Sheet)

Continuation for Block 13

Proposal/Report Number: 73234.10-PE

Report Title: High Absorption per unit Thermal Mass Subwavelength Perforated Membrane as Uncooled Thermal Infrared Detector

Report Type: Ph.D. Dissertation

Publication Type: Thesis or Dissertation

Institution: University of Minnesota

Date Received: 30-Aug-2023 Completion Date: 1/27/23 3:09AM

Title: High Absorption per unit Thermal Mass Subwavelength Perforated Membrane as Uncooled Thermal Infrared Detector

Authors: Avijit Das

Acknowledged Federal Support: **Y**

High Absorption per unit Thermal Mass Subwavelength Perforated Membrane as Uncooled Thermal Infrared Detector

A THESIS

SUBMITTED TO THE FACULTY OF THE GRADUATE SCHOOL

OF THE UNIVERSITY OF MINNESOTA

BY

Avijit Das

IN PARTIAL FULFILLMENT OF THE REQUIREMENTS

FOR THE DEGREE OF

Doctor OF Philosophy

Joseph J. Talghader

Jan, 2023

Acknowledgements

This thesis has become possible due to the contributions of some special people.

First and foremost, my sincere gratitude to my advisor Prof. Joseph Talghader (Joey) for guiding and supervising me for the last few years. As an advisor, Joey not only helped me become more creative and resourceful as a professional researcher but also broadened my insights for personal development. This Ph.D. journey would never be possible without his support.

I would like to thank Yu-Jen Lee, who was my predecessor on the infrared project, with whom I shared my good and bad days doing experiments in the lab and publishing papers eventually. I found him a very hard-working person, who never got tired until having the results.

I share the credit for most of my work with my mentor and research scientist Merlin Mah. Merlin is extremely dedicated and persevering in his work, and he helped me in almost every possible way. I am really indebted to his technical suggestions and especially the 3D-printed customized mounts for the infrared thermal detector experiment.

I am also grateful to my fellow researcher John Hunt, who always came up with insightful suggestions about any technical problem.

Many colleagues from outside our research group have helped. I would like to cordially thank Prof. Sarah Swisher of the Department of Electrical Engineering at the University of Minnesota, for allowing me to use the 'Tube-furnace' tool in her research lab during fabricating my infrared detector. In addition, I am grateful to Prof. Maryam

Jalali-Mousavi of Texas A&M Corpus Christi for providing the polyimide solution, without which successful fabrication might not be possible. I also acknowledge Mr. Kevin Roberts, a scientist of Minnesota Nanofabrication Center (MNC), for helping me with the electron beam (E-beam) lithography and for all the valuable suggestions.

I would not have been able to spend these years in graduate school with joy and happiness if not for my fellow graduate students and friends at and around the office. I wish to thank Tianqi Luo, Phyo Lin, Zach Tebow, Connor Hashemi, Andrew Brown, Phil Armstrong, Neel Chatterjee, Prafful Golani, Sanjoy Basak, Minal Nahin, and Mohammad Shohel for putting smiles on my face every day. They were always there to help whenever I needed them.

Last but not least, this thesis would never be possible to finish without the funding support from the Army Research Office (ARO) and Joint Directed Energy Transition Office (DE-JTO), which are gratefully acknowledged.

Dedication

To my father, who couldn't survive COVID to see me graduate. He always inspired me to earn my Ph.D. May His soul rest in peace.
To my mom and sister, without whom I probably couldn't finish my thesis, and to the Almighty, who is the most merciful and gracious.

"For those who have conquered the mind, it is their friend. For those who have failed to do so, the mind works like an enemy."

Shrimad Bhagavad Gita, 6-6

Abstract

In the first project, a theoretical and experimental investigation of photon diffusion is discussed in highly absorbing microscale graphite. A Nd:YAG continuous wave laser is used to heat the graphite samples with thicknesses of 40 μm and 100 μm. Optical intensities of 10 kW cm^{-2} and 20 kW cm^{-2} are used in laser heating. The graphite samples are heated to temperatures of thousands of kelvins within milliseconds, which are recorded by a 2-color, high-speed pyrometer. To compare the observed temperatures, the differential equation of heat conduction is solved across the samples with proper initial and boundary conditions. In addition to lattice vibrations, photon diffusion is incorporated into the analytical model of thermal conductivity for solving the heat equation. The numerical simulations showed close matching between experiment and theory only when including the photon diffusion equations and existing material properties data found in the previously published works with no fitting constants. The results indicate that the commonly overlooked mechanism of photon diffusion dominates the heat transfer of many microscale structures near their evaporation temperatures. In addition, the treatment explains the discrepancies between thermal conductivity measurements and theory that were previously described in the scientific literature.

In the second project, a subwavelength perforated metamaterial absorber is developed for a maximum absorption-to-thermal mass ratio to construct an uncooled thermal infrared ($\lambda\sim8-12$ μm) detector operating at a time constant of $\sim$7.4 ms, faster than the video frame rates, with a noise equivalent temperature difference (NETD) of 4.5 mK and a detectivity of $3.8\times10^{9}\text{cm}\sqrt{Hz}/\text{W}$. The designed metamaterial absorber consists of Ti, SiN_x, and Ni nanoscale films with an overall fill factor of $\sim$28%, where subwavelength interference and Fabry Perot resonance induce an absorption per unit mass of approximately $1.3-27.6$ times higher than the previously reported infrared absorbers. We read out the fabricated detector optically via Mach Zehnder interferometer.

Contents

List of Tables

List of Figures

Chapter 1

Heat transfer via photon diffusion

The heat transfer and cooling of electronic and optical materials is generally treated as a combination of conduction, convection, and radiation; however, while these three mechanisms certainly dominate microscale systems near room temperature ($\sim$ 300 K), they fail at extremely high temperatures. Under these conditions, near the evaporation temperature of many solids, photon diffusion dominates the heat transfer. In photon diffusion, thermal emission occurs throughout a material, but the photons produced are quickly reabsorbed and reemitted repeatedly while traversing the material [1]. This sequence of events creates a random walk of photons that can be modeled as a diffusion process, as shown in Fig. 1.1. Photon diffusion has long been known to dominate the heat transfer in the photospheres of stars [2, 3] and planetary interiors [4, 5, 6] (Fig. 1.2), but it has seldom been applied to solid materials, except in diathermanous materials such as glasses, where heat transfer can occur via radiation through a transparent material but does not significantly heat the material itself [7, 8, 9]. This is unfortunate because there are many situations, such as particle combustion, laser machining, and even runaway device failure, where extremely high temperatures are reached, and traditional heat transfer models fail completely. It is noted that the term *photon diffusion* is often used to describe light scattering in biological tissues [10, 11, 12] and also studied to analyze the

nonradiative energy transfer(i.e. Förster resonance energy transfer) in donor–acceptor fluorophore molecules [13, 14, 15]. However these applications do not imply photon diffusion as a heat transfer mechanism and therefore, are not further discussed in the thesis.

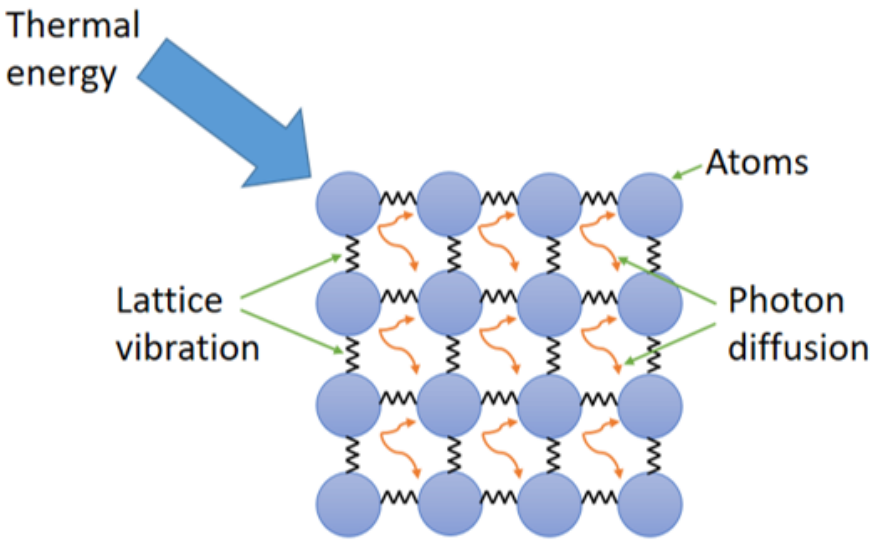

Figure 1.1: Schematic illustration of heat transfer in an array of solid atoms closely placed to one another. In addition to lattice vibrations (or phonons), random diffusive walk of photons also contribute to heat transfer when the temperature is enormously high.

In glass, radiant heat transfer was first reported by Kellett [7]. He mathematically explained the phenomenon of photon heat transfer inside diathermanous media like glasses. Later on, Genzel showed a quantification of photon heat conduction in terms of *photon thermal conductivity* for different glasses [8]. The photon conductivity explained the relation between radiative heat flux and temperature gradient and was subsequently used for other materials. In ceramics, Lee and Kingery reported the theoretical and experimental measurements of photon conductivity for alumina, silica and Vycorbrand glass (V−1) [9]. They investigated the photon driven heat conduction from

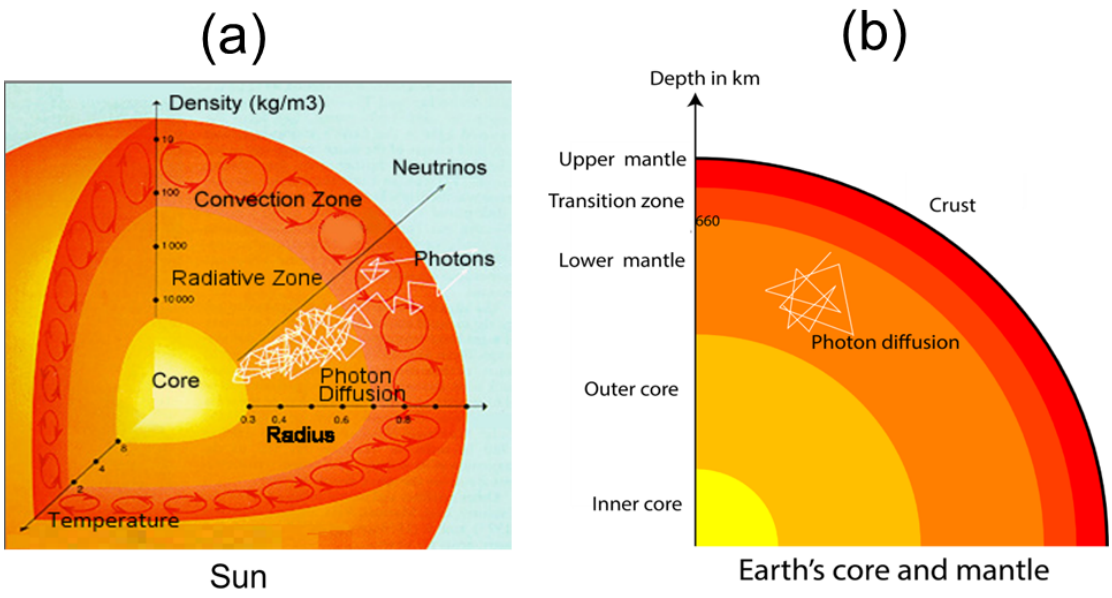

Figure 1.2: Dominance of photon diffusion for heat transfer in astrophysical environments such as (a) the photospheres of stars and (b) the hot interiors of planets.

room temperature to 1500 K. In planetary rocks and minerals, photon conduction was extensively studied by Aronson *et al* [16] and Clauser [17]. Aronson *et al* calculated the photon conductivity for a number of minerals by measuring the refractive index and absorption coefficient at high temperatures. Clauser reported a significant increase in the thermal conductivity (due to photon diffusion) of volcanic rocks at high temperatures (above 1473 K). In recent times, Keppler *et al* discussed the variation of the photon conductivity of Earth's lower mantle mineral (i.e. silicate perovskite) with pressures as high as 125 GPa [18]. However, all of the materials discussed above are either largely transparent or otherwise restricted to very large volumes. There is very little, if any, work reported on photon diffusion dominating thermal heat transfer on the microscale or in highly absorbing solids. Recently, the experiments of Mitra *et al* implied the dominance of photon diffusion for heat conduction in highly absorbing stainless steel particles under laser acceleration [19] (Fig. 1.3). This work, however, was indirect and encourages a direct measurement of heat transfer in the high-temperature microscale

regime.

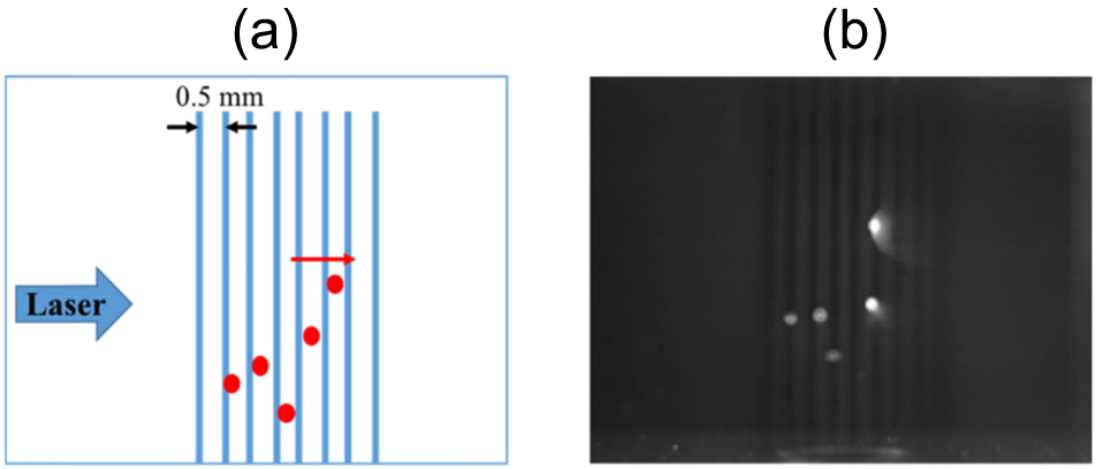

Figure 1.3: Photon diffusion for heat transfer in laser accelerated microscale particles [19].(a) A conceptual representation of particles in front of an etched "ruler" as they enter and are accelerated by a laser beam. (b) Stainless steel particles (d=37−41 μm) accelerated by a 17 kW CW ytterbium-doped IPG laser. Particle acceleration can be correctly predicted when photon diffusion is considered for heat transfer within the particles.

It was our aim to investigate the effect of photon diffusion on the heat transfer of highly absorbing microscale solids. Chapter 2 will provide the details of our experiments and our development of theory for the heat transfer in a microscale sample, which validates the contribution of photon diffusion near the evaporation temperature.

Chapter 2

Photon diffusion in microscale solids

2.1 Introduction

We found the first quantitative evidence that photon diffusion can dominate heat transfer in microscale solids. In this regard, we used a continuous wave (CW) laser with intensities of 10 kW cm^{-2} and 20 kW cm^{-2} to heat high absorption graphite samples. We measured the transient temperatures of the heated samples using a high-speed pyrometer. In addition, we numerically solved the heat transfer equation across the graphite samples considering both lattice and photon contributions to the heat conduction. Close matching was achieved between the experiment and theory. Remarkably, the models only included fundamental photon diffusion theory and existing material properties for graphite found in published articles. No fitting constants were required to achieve matching.

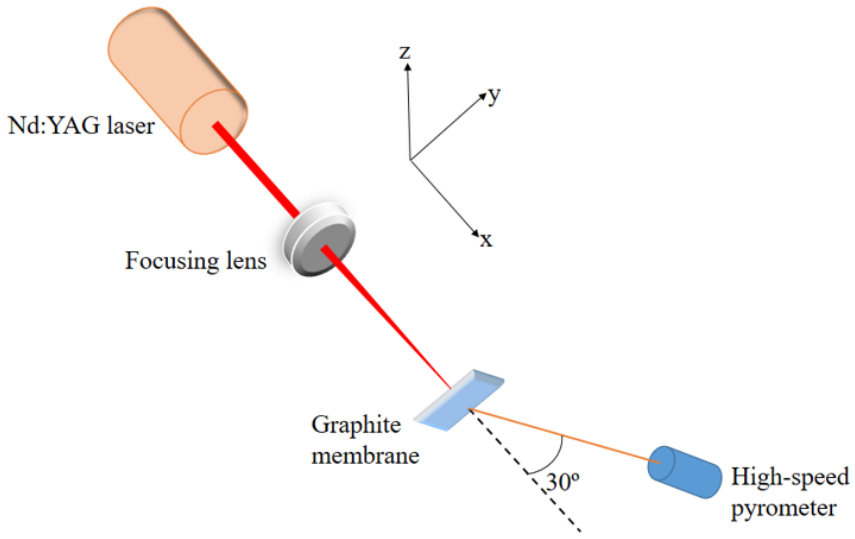

Figure 2.1: Schematic illustration of the experimental setup. The collimated light coming from the Nd:YAG laser goes through the focusing lens and converges onto the graphite sheet producing a spot size of ∼1 mm. The light beam propagates along the x−direction and the graphite sheet is placed along the y−z plane, normal to the light beam. A high-speed, 2−color (ratio) pyrometer measures the transient temperature increase of the graphite sheet. To prevent laser damage to the pyrometer, it is placed at an angle of 30° inclined to the beam direction.

2.2 Experimental setup

Laser heating experiments were performed at our main lab in the University of Minnesota, where a 175 W CW neodymium-doped yttrium aluminum garnet (Nd:YAG) laser was used to heat up the graphite samples. This laser was operated at a wavelength of 1064 nm. The output of the laser was collimated and focused to produce a 1 mm beam spot. Output intensities of 10 kW cm^{-2} and 20 kW cm^{-2} were used for laser heating within the 1mm spot size. The basic experimental setup is shown in Fig. 2.1. The collimated beam coming out of the Nd:YAG laser propagated along the x−direction and was focused through a convex lens onto a thermal graphite sample. The lens was

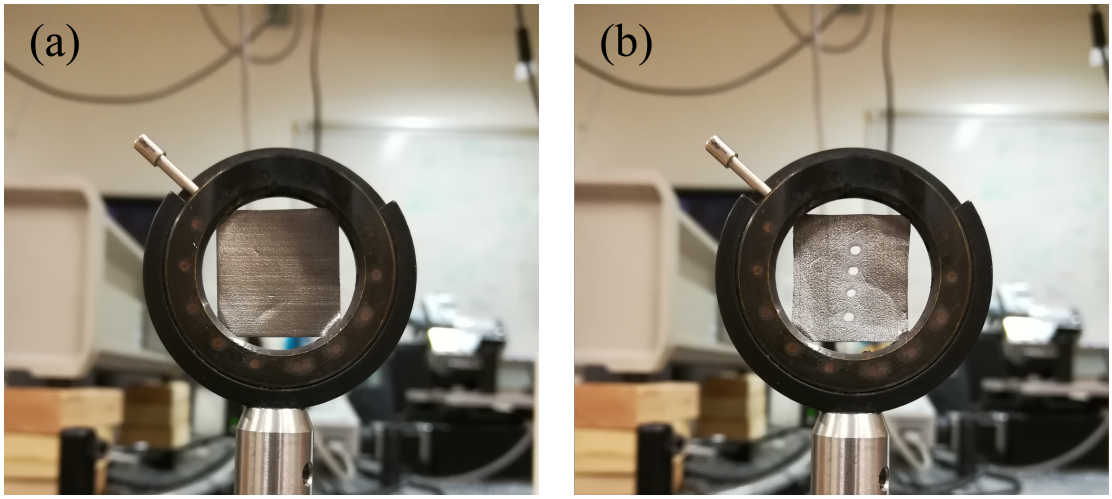

Figure 2.2: (a) a 100 μm thick graphite sheet membrane suspended in a hollow sample aperture before laser illumination. (b) After 4 s of illumination, the graphite sheet completely sublimates in the area of the incident laser beam. Four vertical holes, each of $\sim$1mm diameter, are created with 1$-$2 mm gaps between them. This clearly suggests that the sheet edge support does not affect the instantaneous heat transfer of the graphite sheet along its thickness.

placed 25 cm away from the laser and 16 cm away from the graphite sample. An exfoliated flexible graphite sheet from MinSeal was used as the graphite sample. The flexible sheet was manufactured from mineral graphite. Two sheet thicknesses were tested: 40 μm and 100 μm. The thicknesses of the sheets were quite uniform, with relatively small uncertainties of $\sim$2%. Each sheet was cut into 2 cm$\times$2 cm square pieces, and a piece was suspended in the hollow aperture of a sample holder (i.e. optical mount) along the y$-$z plane, normal to the laser beam direction (Fig. 2.2). Under CW illumination, the transient temperatures of the heated graphite sheet were measured using a high-speed pyrometer. The pyrometer was a 2$-$color, digital infrared device from Process Sensors and had a spectral response of 1.45 μm$-$1.8 μm. Since the pyrometer was not responsive to the operating wavelength (1.064 μm) of the Nd:YAG laser, no optical filter was used to block the Nd:YAG radiation. To protect from any damage incurred by the direct

illumination of the Nd:YAG, the pyrometer was placed at an angle of 30° with respect to the x−direction. Extreme care was taken to focus the Nd:YAG beam spot and pyrometer alignment laser spot at the same point on two opposite faces of the graphite sheet. A slight misplacement of these spots would incur errors in the temperature measurements. After focusing, the pyrometer took transient temperature readings in the range of 1100 K−3000K (measurement limit) with a response time of 3 ms. During the experiment, we found the graphite sheet to sublimate within ∼3−4 s after the Nd:YAG illumination began. Fig. 2.2(a) shows a 100 μm thick graphite sheet (2 cm×2 cm membrane) before laser illumination, and Fig. 2.2(b) shows the complete sublimation of the graphite sheet in the areas of the incident laser beam (1 mm beam spot) after 4 s of laser illumination. Therefore, to avoid significant material evaporation we limited all laser shots to 1–2 s.

2.3 Theoretical development

2.3.1 Thermal model of heat transfer

In Fig. 2.3, we illustrate the concept of laser heating in a microscale graphite sheet. A graphite sheet with thickness L is placed normal to the propagation direction of a Nd:YAG beam. The thickness of the sheet is along the x−axis, and the surface area is across the y−z plane. The laser beam illuminates the front surface (x = 0) of the graphite sheet, producing an incident intensity Q_{in} across a 1 mm beam spot. This initiates thermal heat conduction into the graphite sheet. However, the thickness of the sheet (40 μm or 100 μm) is so small compared to the surface area (2 cm×2 cm) and the 1 mm beam spot that, we can ignore heat transfer across the surface (y−z plane) and consider one−dimensional (1D) heat penetration only along the thickness (x−axis), as seen in Fig. 2.3 [20]. In addition, we can ignore any heat conduction between the graphite and the sheet edge supports, as the incident beam is far away from those supports, and heat penetration along the thickness is unaffected by the sample holder (Fig. 2.2(b)). After illumination, the heat flux is absorbed and then radiated from the

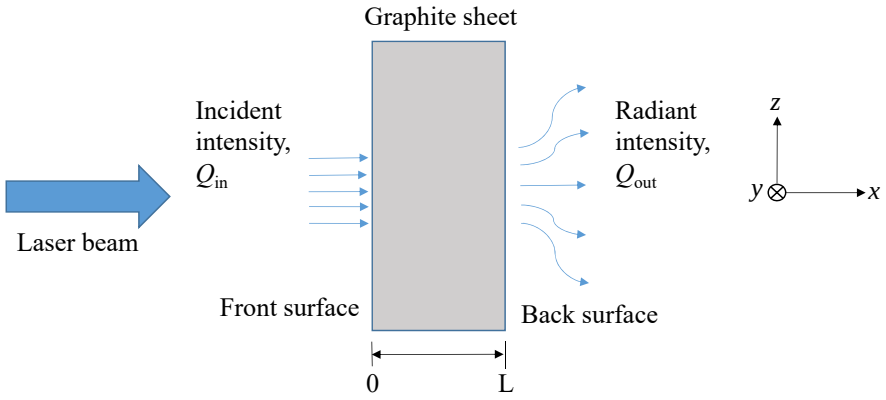

Figure 2.3: Schematic illustration of the 1D heat transfer in the graphite sheet. An Nd:YAG laser beam produces an incident intensity, Q_{in} on the front surface (x = 0). The incident flux is absorbed and then radiated from the back surface (x =L), producing a radiant intensity, Q_{out}.

back surface (x =L) of the graphite sheet, producing a radiant heat intensity Q_{out}. It is noted that we assume the scattering and hence, reflectivity from the front surface (x=0) to be quite small, and the absorption of incident heat flux to be very high due to high power laser illumination [21, 22]. However, to find out the increase in temperature T at any time (t > 0) or distance (0 < x < L), the heat equation needs to be solved along the x−direction and can be expressed as [23, 24],

$$\rho C_{\text{P}} \frac{\partial T}{\partial t} = K \frac{\partial^2 T}{\partial x^2}, \tag{2.1}$$

where ρ is the density, C_{P} is the specific heat at constant pressure, and K is thermal conductivity of graphite. To solve Eq. (2.1), proper boundary conditions must be applied on the front and back surfaces of the sheet, which requires modeling Q_{in} and Q_{out}. Q_{in}

Table 2.1: Parameters used in the numerical simulation

Notation and meaning	**Value of the parameter and unit**
L, thickness of the graphite sheet	40 μm and 100 μm
Q_{in}, optical intensity	10 kW/cm^2 and 20 kW/cm^2
σ, Stefan Boltzmann constant	5.67$\times$10^{-8} W/m^2-K^4
ϵ , emissivity of graphite	0.9
n, refractive index of graphite	3.25 [33]
T_{en}, temperature of surrounding environment	300 K
T_0, room temperature (initial condition)	300 K
α, mean absorption coefficient of graphite	1/270 nm^{-1} at λ=1064 nm [34]
ρ, density of graphite	1.8 g/cm^3 [34]

can be modeled using a one-dimensional form of Fourier's Law as [25],

$$Q_{\text{in}} = -K\frac{dT}{dx}, \tag{2.2}$$

where $\mathrm{d}T/\mathrm{d}x$ is the temperature gradient along the thickness of the graphite sheet. On the other hand, Q_{out} can be modeled using the Stefan-Boltzmann Law as [26, 27],

$$Q_{\text{out}} = \varepsilon\sigma T^4 - \varepsilon\sigma T_{\text{en}}^4, \tag{2.3}$$

where ϵ is the emissivity of graphite, σ is the Stefan$-$Boltzmann constant, and T_{en} is the temperature of the surrounding environment. All these parameters are mentioned with their respective values in Table. 2.1. It is noted that Eq. (2.3) is valid for a graphite sheet as graphite is a well-known high-absorbing material [28] and is commercially used in blackbody walls [29, 30] and infrared filaments [31, 32]. However, the purchased commercial graphite had a reported emissivity of 0.9 in the datasheet. Moreover, during the experiment, the graphite sheet was absorbing heat at 1.064 μm, and at high temperatures (e.g., 2000 K), the peak emission would be at longer wavelengths than 1.064 μm. Therefore, ε of 0.9 would be more appropriate for our experiment.

2.3.2 Thermal properties of graphite

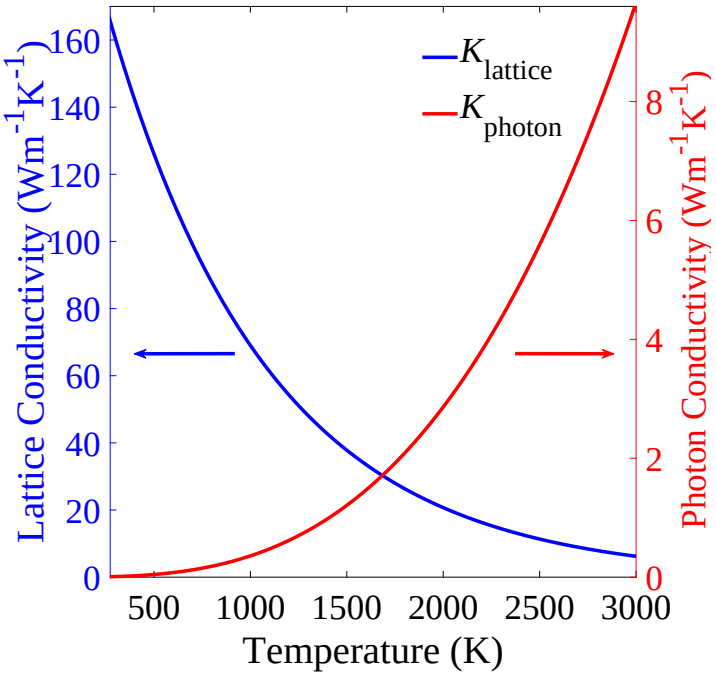

Figure 2.4: Lattice and photon thermal conductivity of graphite with temperatures, as calculated from Eqs. (2.4) and (2.5), respectively.

Heat conduction in the microscale graphite sheet of course depends on the two major thermal properties of the material: thermal conductivity K and specific heat C_{P}. Over the past few decades, these properties have been analyzed and explained in the literature, along with their dependence on temperature [35, 36]. However, analytical expressions are required to describe the temperature dependence and hence, are included in the thermal model which will be discussed in this section.

In graphite at very low temperatures (i.e. 50 K), heat conduction primarily depends on specific heat [37]. The thermal conductivity gradually increases with increasing temperature up to a maximum point. The temperature of this maximum point (also known as peak temperature) may vary from 80 K to 200 K, depending upon the crystalline structure of the graphite [37, 38]. However, above the peak temperature and up to ∼1800 K, heat conduction is dominated by lattice vibrations, or phonons, which show an inverse temperature dependence [37, 39, 40]. The phonon-phonon and phonon-defect scattering in a nonmetallic crystal, such as poly-crystalline graphite can be understood from the temperature dependence of the Lorenz function, which is directly proportional to the thermal conductivity. The Lorenz function shows a gradual decrease with increasing temperature, which justifies the inverse temperature dependence of phonon dominant thermal conductivity of graphite [40]. A number of articles have verified this temperature dependence by reporting experimental data specifically for poly-crystalline (i.e. Acheson) graphite in the range of 273 K to 1800 K [40, 41]. These experimental values of lattice or phonon dominant conductivity can be curve-plotted, and an empirical analytical expression can be formed as,

$$K_{\text{lattice}} = 230.114e^{-0.001204T}, \tag{2.4}$$

where temperature T must be greater than or equal to 273 K. As room temperature is considered the initial condition in our model, analytical modeling of K_{lattice} below 273 K is not required. Note that exfoliated graphite is typically poly-crystalline [42, 43, 44], and has similar physical and thermal properties as of Acheson graphite [45, 46]. Therefore, the experimental conductivity values of Acheson graphite can be used to model $K_{\}rmlattice}$. In addition, due to the empirical fitting of K_{lattice}, some errors might arise from the experimental measurements. From [40, 41], these errors are found $\pm 1 - \pm 4$ $\text{Wm}^{-1}\text{K}^{-1}$ (normalized RMS error of ∼3.8%) for temperatures up to 1800 K which are quite small, and indicate that the analytical expression of K_{lattice} is a good empirical

model for lattice conductivity with adjusted R^2 of 98.2%. However, these small errors can be attributed to slight variations in the experimental measurements of the phonon conductivity, which originates from the random distribution of the crystal defects (i.e. grain boundaries, dislocations) in the poly-crystalline graphite [47].

At relatively high temperatures (above ∼1800 K), photon diffusion is likely to contribute to the heat transfer through the graphite sheet in addition to lattice vibrations [48, 49]. The rate of diffusion (in other words, emission or absorption) of photons largely depends on the optical constants, i.e. refractive index and photon mean free path of graphite. The photon mean free path is comparatively smaller than the graphite sheet, therefore the path of photons resembles a random diffusion walk across the thickness of the sheet. In the literature, photon diffusion has been incorporated into thermal conduction as 'photon thermal conductivity'. In general, the photon conductivity for graphite can be expressed as [2],

$$K_{\text{photon}} = \frac{16n^2\sigma T^3}{3\alpha}, \tag{2.5}$$

where n is the refractive index and α is the mean absorption coefficient of graphite. These parameters may vary with temperature; however, the variations are found to be quite negligible ($\sim 0.43\% - 0.54\%$ for n and ∼0.34%–1.2% for α) [50]. Therefore, the temperature variations of n and α are discarded in our thermal model.

Fig. 2.4 presents a comparison between the lattice and photon thermal conductivities, as calculated from Eqs. (2.4) and (2.5) respectively. With increasing temperatures, K_{lattice} decreases, and K_{photon} increases mainly due to their opposite temperature dependence. It is noted that the lattice conductivity calculated from K_{lattice} closely matches with the *ab initio* calculations derived for poly-crystalline graphite (small grains) [51], with a normalized RMS error of ∼4.5%. This further verifies the accuracy of the empirical modeling of K_{lattice}. An expression for K_{photon} is already derived from first principle calculations [52, 53].

At very high temperatures, the total thermal conductivity of graphite can be assumed as the summation of the lattice and photon conductivities [9], that is

$$K_{\mathrm{T}} = K_{\mathrm{lattice}} + K_{\mathrm{photon}}, \tag{2.6}$$

Note that electrons in poly-crystalline graphite do not contribute significantly to the total thermal conductivity even at elevated temperatures. Using the Wiedemann-Franz law [54] (which applies to a free electron gas such as the conduction electrons of graphite at high temperature) and experimental measurements of the electrical conductivity of poly-crystalline Acheson graphite [40], the electron thermal conductivity is found to be ∼5.58% of the lattice conductivity and ∼5.55% of the photon diffusion conductivity even at elevated temperature (i.e., 2800 K). Therefore, the electron contribution to the thermal conductivity is neglected in Eq. (2.6).

At temperatures above 700 K, graphite is likely to oxidize in ambient air. Here the graphite reacts with oxygen and produces carbon monoxide (CO) and carbon dioxide (CO_2). This chemical reaction can release additional exothermic heat with an amount proportional to the oxidation reaction rate. In previous literature, the oxidation rate was found to be dependent on the air velocity when the temperature exceeds 1150 K [55], with a proportional to temperature increase in the oxidation rate at elevated temperatures (1150 K and above) when the air velocity is fixed [55]. Since the standard air velocity of the indoor environment (i.e., office, research space) lies between 15 cm s^{-1} to 22 cm s^{-1} [56, 57], we considered this range to calculate the oxidation rates at temperatures 1150 K and above. With the calculated rates, however, we analyzed the exothermic heat intensity produced on the graphite samples with the formation of CO and CO_2 gases. Even at elevated temperature (i.e., 2800 K), the exothermic heat intensities were found only ∼0.0115%−0.0119% of the 10 kW cm^{-2} laser intensity when CO forms, and ∼0.0433%–0.0448% of the 10 kW cm^{-2} laser intensity when CO_2 forms (please see Appendix B). It is obvious that the exothermic heat intensities are quite

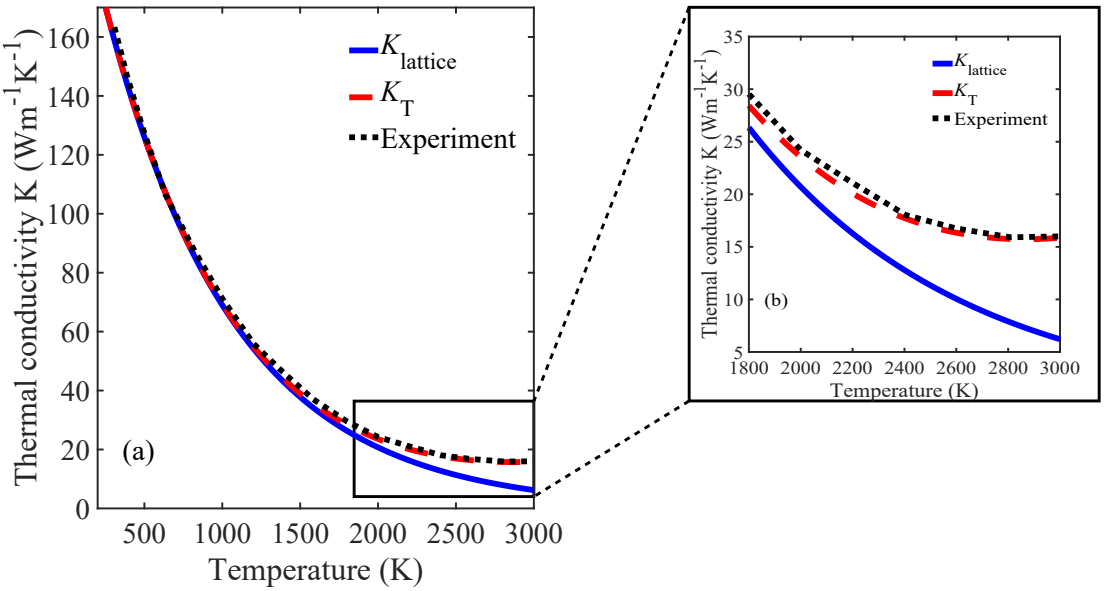

Figure 2.5: (a) Thermal conductivity of graphite with temperatures in the range of 273 K to 3000 K. Eqs. (2.4) and (2.6) are simulated for K_{lattice} and K_{T}, respectively. Experimental data are taken from [40]. (b) Thermal conductivity values at high temperatures (1800 K−3000 K) are presented in an inset, showing the deviation between the theory and experiment. It is noted that the deviations between K_{lattice} and the experiment were not covered in previous articles and only our addition of the photon diffusion contribution to the thermal conductivity (K_{T}) closely fits the experimental data.

negligible compared to the incident laser intensities (10 kW cm^{-2} and 20 kW cm^{-2}) used in the experiment. Therefore, the exothermic heat release, and hence the oxidation effects are not included in our thermal model. Moreover, the heat transfer between air and graphite is ignored, as it is quite negligible (∼1.2%) compared to the heat transfer along the thickness of the graphite sheet even at high temperatures [58].

To further illustrate the validity of Eq. (2.6), we simulated thermal conductivity from Eqs. (2.4) and (2.6) for a wide range of temperatures (273 K−3000 K). Fig. (2.5)(a) presents the simulated results along with the experimental data taken from [40], which had unexplained discrepancies between its thermal conductivity models and data. It

is noted that both theoretical and experimental conductivities show a gradual decrease with increasing temperature. At temperatures below 1800 K, K_{lattice} is dominant and predicts the experimental results of the thermal conductivity quite well. However, at temperatures above 1800 K, experimental data start to deviate significantly from the analytical values of K_{lattice}. To further illustrate this scenario, thermal conductivities at high temperatures (1800 K$-$3000 K) are zoomed in Fig. (2.5)(b). It is observed that with increasing temperatures, experimental data show a comparatively smaller decrease than K_{lattice}, resulting in an increasing relative error up to $\sim$53%. However, we included K_{photon} in the total thermal conductivity K_{T} and found a close match with the experimental data points, providing much smaller relative error up to $\sim$2.7%. We note that at relatively high temperatures, i.e., above 1800 K, K_{photon} becomes significant and starts to dominate over K_{lattice} mainly due to the large T^3 dependence of K_{photon}. This addition appears to fully explain the previous disagreement between prior theory and modeling for high-temperature graphite.

In order to model the specific heat C_{P}, experimental measurements can be adapted from a number of research articles [59, 60, 61, 62, 63, 64]. Due to a large number of types of graphite (i.e., natural, artificial, reactor-grade, synthetic, etc), not all of these measurements relate to polycrystalline graphite. However, due to the nature of heat capacity and the reasonably similar densities of the different types of graphite, the specific heat is often assumed to be the same for all types [65]. Therefore, experimental evaluations for different ranges of temperatures have been combined, and a polynomial expression can be formed by curve-fitting the measurements as

$$\begin{aligned} C_{\text{P}} &= 2251.58 + 3.81 \times 10^{-2}T - 3.77 \times 10^{5}T^{-1} - 1.82 \times 10^{8}T^{-2} \\ &+6.66 \times 10^{10}T^{-3} - 6 \times 10^{12}T^{-4} \end{aligned} , \tag{2.7}$$

where temperature T lies in the range of 200 K to 3000 K. It is noted that Eq. (2.7) is an empirical fit to experimental data measured by other research groups; therefore, there are some errors associated from the experimental measurements of the specific

heat. From [65], the associated errors are found as $\pm 15 - \pm 27$ J kg^{-1} K^{-1} for temperatures below 1000 K, and $\pm 29 - \pm 53$ J kg^{-1} K^{-1} for temperatures above 1000 K. However, these errors are quite small compared to the analytical values of C_{P} which makes Eq. (2.7) a good empirical fit for specific heat, with adjusted R^2 of 95.3% and 90.8% for temperatures below 1000 K and above 1000 K, respectively.

2.4 Results and discussion

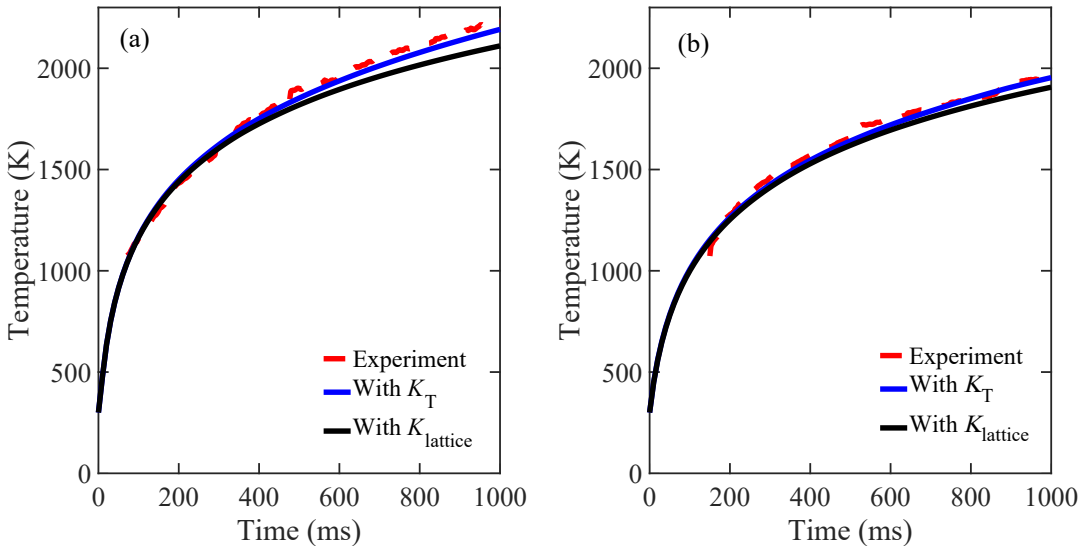

Figure 2.6: Transient temperature profile for (a) 40 μm and (b) 100 μm thick graphite sheets with optical intensity of 10 kW cm^{-2}.

To understand the heat transfer across the microscale graphite sheet, we solved the partial differential equation Eq. (2.1) with boundary conditions stated in Eqs. (2.2) and (2.3). Analytical expressions of K_{T} and K_{lattice} were used from equations Eqs. (2.4)$-$(2.7). For numerical simulation, we used the partial differential equation (PDE) toolbox in MATLAB. The PDE toolbox used numerical differentiation formulas (NDFs) of orders 1 to 5 to solve the heat equation [66]. Relative error tolerance was kept at 10^5; therefore,

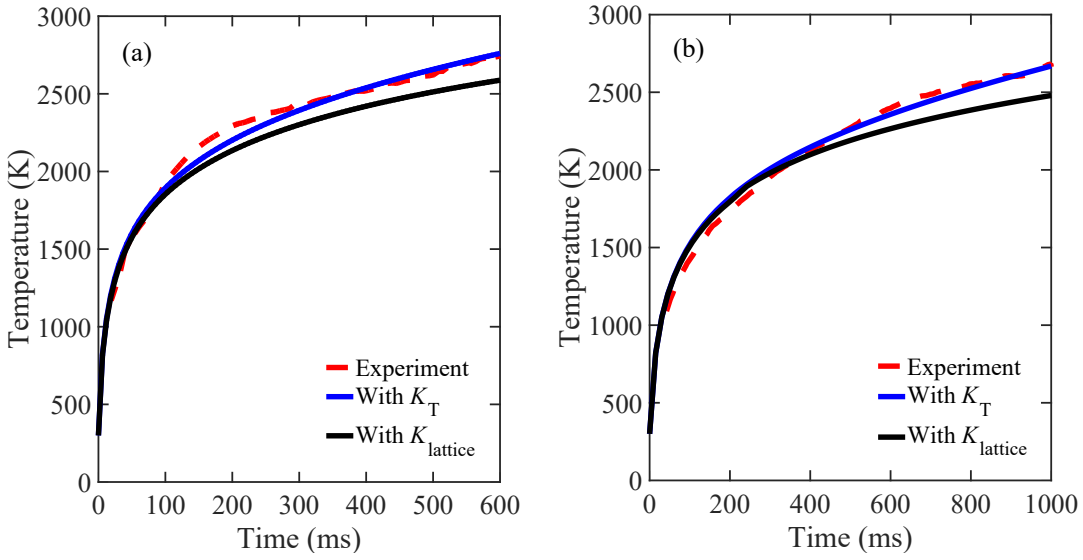

Figure 2.7: Transient temperature profile for (a) 40 μm and (b) 100 μm thick graphite sheets with optical intensity of 20 kW cm^{-2}.

the local discretization error was below this tolerance. We simulated the transient temperatures under the laser intensities of 10 kW cm^{-2} and 20 kW cm^{-2}. To illustrate the effect of photon diffusion, we added K_{lattice} and K_{photon} to form the effective thermal conductivity K_{T}. We used both K_{lattice} and K_{T} in our simulation, and compared the simulated results with our experimental measurements. To ensure the accuracy and precision of our experimental data, we measured three sets of transient temperatures for each experiment and then took the average to estimate the actual set of temperature measurements. The relative uncertainty of the temperature measurements was found to be $\sim$0.2%$-$0.5% which was quite negligible. As all the experimental measurements were taken from the back surface of the graphite sheet, the numerical simulations were also performed at x = L, as seen in Fig. (2.3).

Figure 2.6 shows the comparison of experimental and simulation results for 40 μm and 100 μm graphite sheets with a laser intensity of 10 kW cm^{-2}. With the same illumination duration of 1000 ms, temperatures (theoretical and experimental) in the

40 μm sheet show slightly larger increases than temperatures in the 100 μm sheet. In addition, temperatures simulated with K_{T} surpass those simulated with K_{lattice} after reaching ~1800 K, mainly due to the increasing effect of K_{phootn}. Therefore, conduction by photons produces a distinct temperature difference between the simulated results at 1000 ms. From Figs. 2.6(a) and 2.6(b), the difference is found as ~85 K and ~40 K for 40 μm and 100 μm sheets, respectively. However, in both cases, temperatures simulated with K_{T} can consistently predict the experimental measurements, implying the contribution of photon diffusion to heat conduction.

To further investigate the effect of photon diffusion, the laser intensity was increased to 20 kW cm^{-2}. Fig. 2.7 shows the simulated and experimented transient temperatures for both 40 μm and 100 μm graphite sheets with the intensity of 20 kW cm^{-2}. We note that during the experiments, temperatures in the 40 μm sheet increased much faster than those in the 100 μm sheet and surpassed the measurement limit of our pyrometer (3000 K) within 800 ms. Therefore, instead of taking the same duration of 1000 ms for both thicknesses, we used different durations of illumination. In Figs. 2.7(a) and 2.7(b), we show time durations of 600 ms and 1000 ms for 40 μm and 100 μm sheets, respectively. Due to the increased laser intensity in this set of experiments, the effects of photon diffusion can be seen more rapidly than in Fig. 2.6. Therefore, the difference between the simulated temperatures with K_{T} and K_{lattice} becomes larger than before. For the 40 μm sheet, the simulation difference is observed as ~170 K at 600 ms, whereas for the 100 μm sheet, the difference is found to be ~179 K at 1000 ms. We note that for the 40 μm sheet, the difference would likely have been much larger than 170 K if measurements could have been performed at 1000 ms. However, the difference already proves the significance of photon diffusion at larger intensity. To further validate this idea, experimental measurements also show reasonable agreement with the temperature simulations performed with K_{T}, as shown in Fig. 2.7.

2.5 Summary

A detailed theoretical and experimental analysis was performed to study the effects of photon diffusion on heat transfer in microscale graphite sheets. A Nd:YAG CW laser with laser intensities of 10 kW cm^{-2} and 20 kW cm^{-2} was used to heat 40 μm and 100 μm thick graphite sheets. Temperatures were found to rise to extreme levels (2000 K and above) within milliseconds, and these temperatures were recorded by a 2-color, high-speed pyrometer. To compare the experimental measurements, a thermal model of heat conduction was developed across the thickness of the graphite sheet. Necessary thermal properties, thermal conductivity, and specific heat were analytically modeled to solve the heat equation across the sheet. When both photon diffusion and lattice vibrations were incorporated in the thermal conductivity of graphite, the results matched well with previous experimental data. However, to have a better understanding, the transient temperatures were numerically solved in two ways; one with only lattice conductivity and the other with combined lattice and photon conductivity. Significant temperature differences were observed between the two simulations with time. However, temperatures simulated with the combined conductivity were found to be in good agreement with our experimental measurements, as expected from our earlier analysis of thermal conductivity. This validates the contribution of photon diffusion to heat conduction in high-absorbing microscale graphite.

Chapter 3

Infrared detectors

3.1 Introduction

For the past few decades, there has been increasing interest in the infrared (IR) spectrum of electromagnetic radiation, especially for its relevant applications ranging from thermal imaging for military cameras [68, 69, 70, 71, 72] to biomedical (e.g., thermography [73, 74] and disease detection [75, 76]) and industrial appliances (e.g., monitoring of bio-process [77]). In our ambient environment, the thermal radiation from all forms of matter reaches its peak in the long-wave infrared (LWIR, $\lambda \sim 8{-}14$ μm) regime, which makes this range suitable for most IR applications [78, 79]. The significance of the LWIR can be realized from the spectral radiance of a black body at 300 K (shown in Fig. 3.1), which can be calculated from Planck's law as,

$$B_R(\lambda, T) = \frac{2\pi hc^2}{\lambda^5} \frac{1}{e^{(hc/\lambda k_{\mathrm{B}} T)} - 1}, \tag{3.1}$$

where B_{R} (λ, T) is the spectral radiant emittance, h is Planck's constant, c is the speed of light, λ is the wavelength, k_{B} is Boltzmann's constant, and T is the temperature.

In general, the highest theoretically possible IR detector performance is achieved at the background limit, where photons emitted from the target dominate the total amount

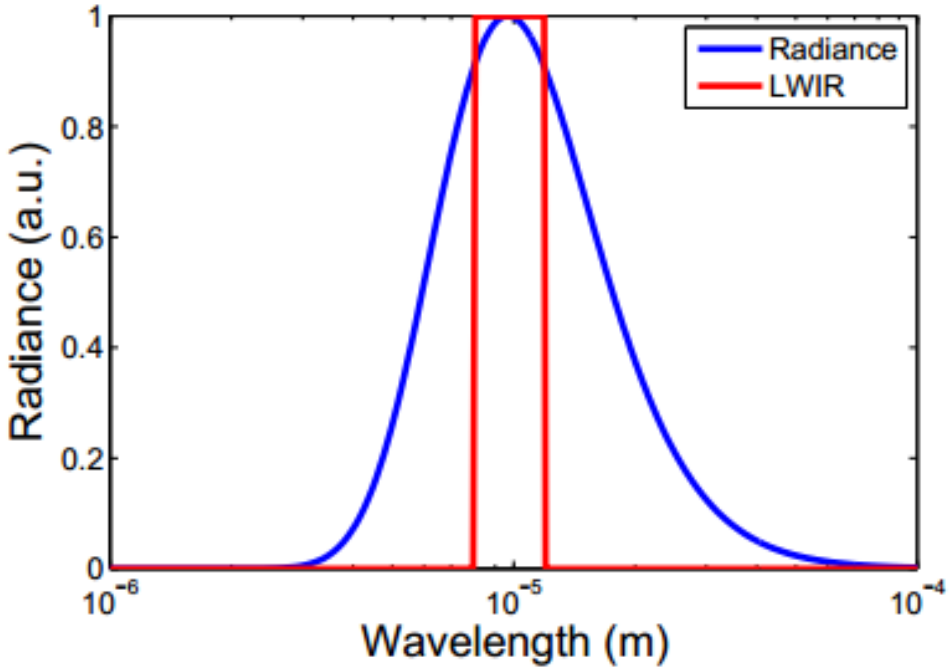

Figure 3.1: Spectral radiance of a 300K blackbody (blue) with the LWIR highlighted (red) [67].

of noise. In the LWIR region, this limit is usually achieved using cryogenically cooled photon detectors, where electrons interact within the material to absorb IR radiation. In spite of the high detectivity and fast data acquisition, the major drawback of photon detectors lies in the requirement of cooling the focal plane array (FPA) down to cryogenic temperatures. It has long been a goal to reach the background-limit without cooling, but within photon detectors, thermal energy overwhelms the narrow bandgaps of the semiconductors, which makes the uncooled operation almost impossible.

3.2 State of the art uncooled technologies

Uncooled LWIR thermal camera technology is primarily dominated by microbolometer arrays, which were developed in the 1970's and 80's by Honeywell [81] and later licensed

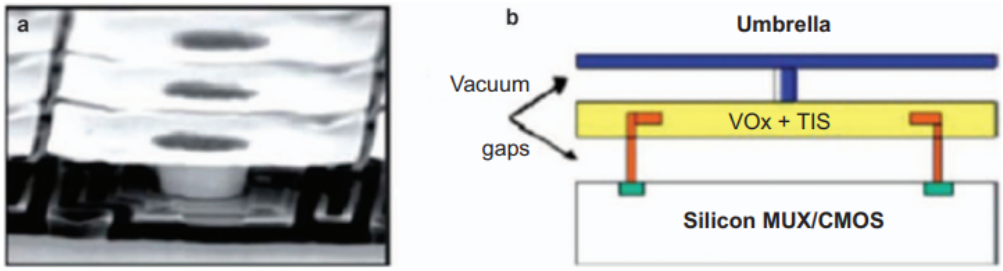

Figure 3.2: Scanning electron microscope (SEM) image (a) and schematic (b) of a microbolometer using the 'umbrella design' from DRS Inc [80].

to several suppliers including DRS, FLIR, Raytheon, etc [82, 83]. Microbolometers are basically thermally isolated resistors that absorb LWIR light, heat the device, alter the device resistance, and allow a bias current to produce a signal-dependent voltage difference. The basic design of uncooled microbolometers has evolved in the last few decades, with an objective of shrinking the pixel size to ensure lower cost and greater pixel density. Allowing signal absorption through an umbrella configuration realizes higher fill factor pixels with a fast speed of response [84]. Fig. 3.2 shows an SEM image and schematic of a microbolometer with umbrella design from DRS [80].

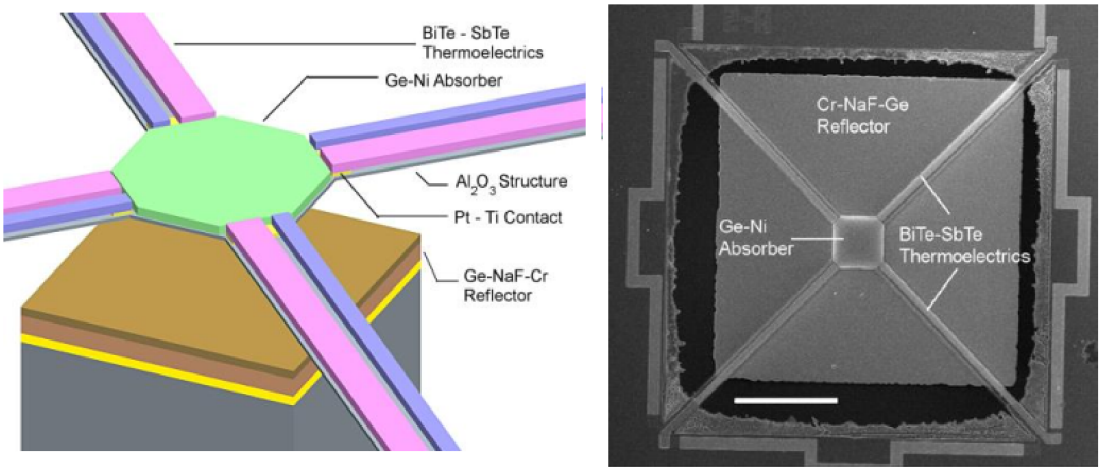

Figure 3.3: Schematic diagram and SEM image of a thermopile detector from the Talghader Lab [85].

Another type of device that dominates the uncooled LWIR technology is thermoelectric detectors such as thermopiles [86, 85, 87]. As shown in Fig. 3.3, a thermopile shows similarity in structure and operation to a microbolometer but differs in its electrical readout. Instead of using temperature-sensitive resistors, thermocouples are used which absorb the LWIR radiation and produce a temperature-dependent voltage based on the Seebeck effect. This has a major advantage over a microbolometer in terms of noise. There are multiple sources of noise in a microbolometer, including Johnson, $1/f$, and thermal conductance noise. Among these, Johnson and $1/f$ originate from electrical sources and are not fundamental to thermal detection. They degrade the minimum measurable signal, often measured using a parameter called the noise equivalent temperature difference (NETD). A thermopile does not need a bias current to measure the temperature-sensitive voltage, and hence it eliminates the source of $1/f$ noise. In theory, this makes a thermopile more sensitive than a microbolometer. However, a major disadvantage arises in a thermopile while sensing the extremely small voltages (e.g., μVs) produced by thermocouples. Each pixel needs a dedicated preamplifier to boost the μV signal before reaching the destined circuitry, which increases the complexity and expense. Nevertheless, significant research is still ongoing for the development of high-sensitive thermoelectric detectors. For example, the most sensitive thermopile detectors, to date, have been designed, fabricated, and characterized in the Talghader group at the University of Minnesota [85, 87], and they show a maximum detectivity of $3{\times}10^9$ cm$\sqrt{Hz}$/W.

Apart from microbolometers and thermopiles, some uncooled detectors utilize the temperature sensitivity of the resonant frequency of a mechanical oscillator, either in the form of a block of mass [88, 89] (e.g., quartz) or a micro-/nano-mechanical resonator (shown in Fig. 3.4) [90, 91]. In either case, the resonant frequency changes upon LWIR absorption (i.e., temperature increase), which can be read out by tracking the resonance shift. Although a number of researchers published promising results for these types of detectors, their commercial popularity has yet to achieve. One probable reason is the

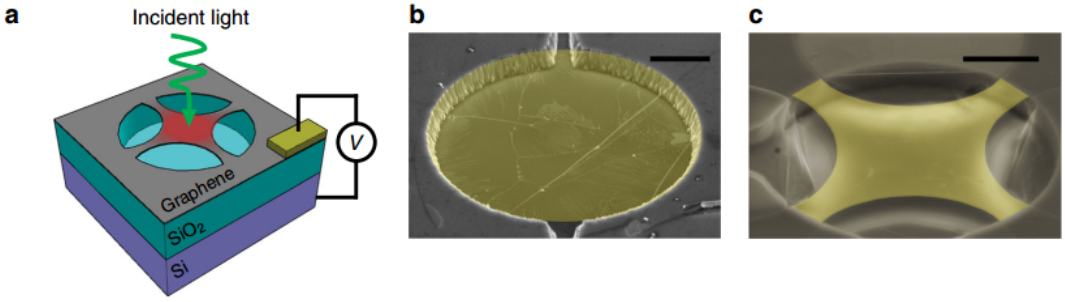

Figure 3.4: (a) Schematic illustration of a graphene nanomechanical resonator as a thermal detector. A driving voltage actuates the motion creating mechanical resonance. Upon LWIR absorption, the graphene membrane experiences stress and shifts the mechanical resonance. An SEM image (false color) of a suspended graphene membrane with shapes of a (b) drumhead and (c) trampoline. [85].

small detector size which is a requirement for the fast thermal response but drives the resonant frequencies to very high values and thus, complicates the readout circuitry. In addition, the fabrication process for a micro-/nano-mechanical oscillator is challenging.

To improve the sensitivity by eliminating the electrical readout, a number of optical read out technologies have been developed, including cantilever detectors [93, 94, 95, 96, 97] and thermo optic cavity detectors [98, 99]. Typically in a cantilever detector (shown in Fig. 3.5), a thermal expansion bimorph is equipped with a micromechanical plate to deflect it out of the plane upon LWIR absorption. A laser is integrated with the plate such that the small changes in the plate deflection are optically read out using changes in the reflection angle of the laser (either by a camera or a position-sensitive detector). Moreover, a thermo-optic detector utilizes a near−infrared cavity made from multilayer coatings as a pixel absorber, which produces a thermo-optic shift in the cavity resonance when the LWIR gets absorbed and causes a temperature-dependent change in the cavity indices of refraction. In spite of eliminating electrical noise, both of these optical IR detectors are often plagued by a large thermal mass, which degrades the

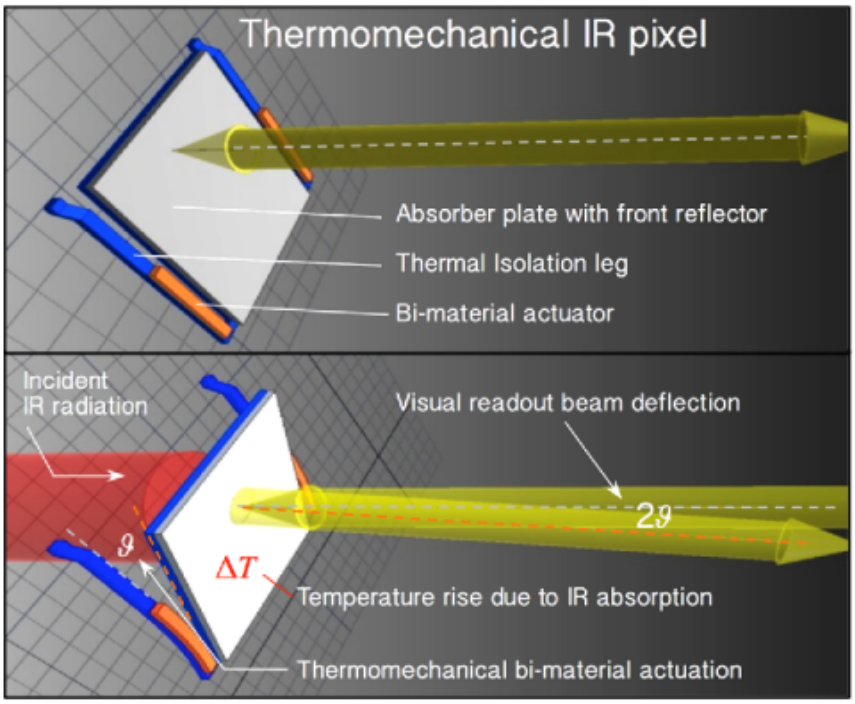

Figure 3.5: A schematic illustration of a microcantilever as an optical IR sensor. The plate exhibits a deflection due to a temperature rise upon LWIR absorption, which is optically read out through a visible readout beam [92]

thermal performance by increasing either the thermal time constant (slow response) or thermal conductance (small response).

3.3 Overview of our work

In general, optimum performance in an optical detector can be achieved if the thermal mass is at exactly the level necessary to prevent temperature fluctuations from dominating the noise. Once this level is reached, a device should have the largest possible absorption area for its thermal mass. One method to maximize the area of a minimum thermal mass infrared detector is to create a perforated structure whose subwavelength periodicity allows it to absorb at high levels throughout the broadband LWIR spectrum.

In this thesis, we demonstrated that a subwavelength perforated membrane designed for a maximum absorption-to-thermal mass can be utilized to construct a highly sensitive uncooled thermal long-wave infrared (LWIR) detector integrated with an optical readout. The organization of our work is described as follows:

- In Chapter 4, we described the design of a broadband LWIR ($\lambda \sim 8-12$ μm) absorber made from metal-dielectric (Ti-SiN$_x$) subwavelength perforated grids. The designed absorber consists of mostly open space (perforations) with an overall fill factor of $\sim$32%, where guided mode coupling realizes an average absorption per unit thermal mass of $\sim 6.8\times10^{12}$ kg^{-1}.

- In Chapter 5, we developed a highly sensitive infrared thermal detector operating at room temperature. We modified the design of the detector absorber to a subwavelength perforated Ti-SiN$_x$-Ni (metamaterial) membrane, which realizes $\sim$18% higher absorption per unit thermal mass than the previously discussed Ti-SiN$_x$ structure. With $\sim$22% lesser thermal mass and 28% overall fill factor, the perforated metamaterial structure shows an average absorption per unit thermal mass of $\sim 7.8\times10^{12}$ kg^{-1}, which is $\sim 1.3-27.6$ times higher than the previously reported infrared absorbers. We described the overall fabrication method of our infrared structure. Key processes of the fabrication include deposition and hard-bake of a sacrificial polyimide, and patterning the nano-scale grids using electron-beam (Ebeam) lithography. We also outlined the various engineering challenges during fabrication. Finally, we analyzed the fabricated device as an uncooled thermal infrared detector using an optical readout technique, i.e., Mach Zehnder interferometry. Mach Zehnder is a commonly known technology chosen because of its ease of integration, as shown in fiber optic communications, and its potential to read an entire array of detectors simultaneously. We showed how the fabricated structure can be integrated with a Mach Zehnder setup, and interference fringes can be analyzed to measure the temperature change. From experiments, we analyzed

the overall performance of our detector in terms of noise equivalent temperature difference (NETD), the thermal time constant, responsivity, and detectivity.

Chapter 4

High Absorption per unit Mass Broadband Infrared Absorber

4.1 Introduction

Achieving near-perfect long-wave infrared (LWIR) absorption with wide bandwidth has become a critical goal in the design and implementation of infrared thermal and imaging devices [85, 100, 101, 102]. Nowadays it has become possible to design LWIR broadband absorbers with ultra-thin subwavelength thicknesses [103, 104, 105, 106]. Furthermore, nearly perfect absorbers have also been studied for their use in bio-sensing [107, 108], photodetection [109], and thermal-emission-based cooling [110, 111, 112, 113].

In recent years, relevant research has focused on the design and development of perfect LWIR absorbers with small amounts of material [114, 115, 116]. Maximizing absorption in a system with low thermal mass is crucial, e.g., in microbolometers and other thermal detectors. In a traditional microbolometer, one attempts to reduce mass to achieve a lower thermal time constant (in other words, faster response) [85, 117]. For high performance radiation-limited thermal detectors, the concept is a bit more subtle. The minimum mass of a detector is limited by the magnitude of intrinsic thermal

fluctuations that can be tolerated on the device; therefore, any mass below this is counterproductive. With this given thermal mass, one then wishes to maximize the area of the detector so that the thermal conductance, which is dependent on the area for radiation-limited devices, can be maximized, reducing the time constant.

To achieve high LWIR absorption with a small amount of material, a number of structures can be investigated, such as metamaterial composites [118, 119, 120, 121, 122], metal-dielectric multilayers [123, 124, 125], and plasmonic metamaterials [126, 127]. In general, metamaterials are composed of three distinct layers: (a) bottom continuous metal film, (b) insulator spacing layer, and (c) top subwavelength metal grids. In such a metal–insulator–metal (M-I-M) configuration, a common approach to achieve broadband absorption is to tailor the size of the top planar metal grids in a single unit cell. Each metal grid supports a single resonant band (impedance matching with incident medium), therefore multiple patches in a unit cell results in a superposition of multiple resonance bands [122]. In addition to increasing the absorption area, this approach has a couple of drawbacks: (1) larger volume of material in a period and (2) the magnetic response may not be simultaneously tuned for all resonator patches in a single unit, resulting in an imperfect impedance matching and hence, imperfect optical absorption [128, 129]. Another approach is to pattern the top layer with alternating metal-dielectric (i.e., metal– insulator, M-I) thin films vertically stacked in a graded fashion, resulting in anisotropic sawtooth [123] or trapezoidal pyramids [124]. The vertically stacked films allow multiple resonant frequencies to be spaced adjacent to one another with smaller intervals among the resonance bands than the planar resonators, resulting in a reduction of the quality factor over a wide bandwidth. However, maximum absorption with low-quality factor can only be achieved when a large number of metal–dielectric films can be stacked in a period, eventually increasing the total volume and decreasing absorption per unit mass. For example, a graded trapezoidal pyramid requires a thickness of 6 μm to maintain perfect broadband absorption in the range of wavelengths from 10 μm to 30

μm [106]. Other metamaterial approaches for perfect broadband LWIR absorption include hyperbolic metamaterials (doped–undoped semiconductor stacks) [130, 131] and unpatterned metal–dielectric pairs [125], which require even larger amounts of material per pixel or period than M-I-M structures. In the case of plasmonic structures, perfect LWIR absorption is typically observed over a narrow bandwidth, which can be attributed to their highly dispersive resonance characteristics [103, 107]. A few works have reported broadband LWIR absorption through the superposition of multiple resonance bands at the cost of larger volumes of plasmonic metamaterials [126, 127], yielding again larger amounts of material. There is hardly if any work reported for broadband absorption over the LWIR transparency window that realizes high absorption with a minimum amount of material.

In this thesis, we designed a broadband LWIR perforated structure that utilizes two-dimensional (2D) subwavelength gratings to maximize absorption per unit thermal mass. Lossy metal (Ti) and dielectric (SiN_x) layers are used to form the subwavelength gratings. Using effective medium theory and guided mode techniques, we analyzed the structure to realize light absorption at high levels throughout the LWIR spectrum (i.e, $\lambda \sim 8-12$ μm). A multilayer transfer matrix method and the numerical finite difference time domain (FDTD) technique were used to analyze the broadband absorption. In addition, we provided a comparative analysis of our structure in terms of absorption per unit mass.

4.2 Theoretical design

Figure 4.1 presents a schematic illustration of our subwavelength perforated broadband absorber. The structure consists of an array of square pitches with a periodicity P of 8 μm. Each pitch contains 49 nano-scale grid units (i.e., solid pitch length L), with each grid having a period g of 1 μm and a perforation size w of 0.8 μm (i. e., perforation ratio, w/g=0.8). An air gap s of 1 μm is utilized around the solid absorber pitches designed to

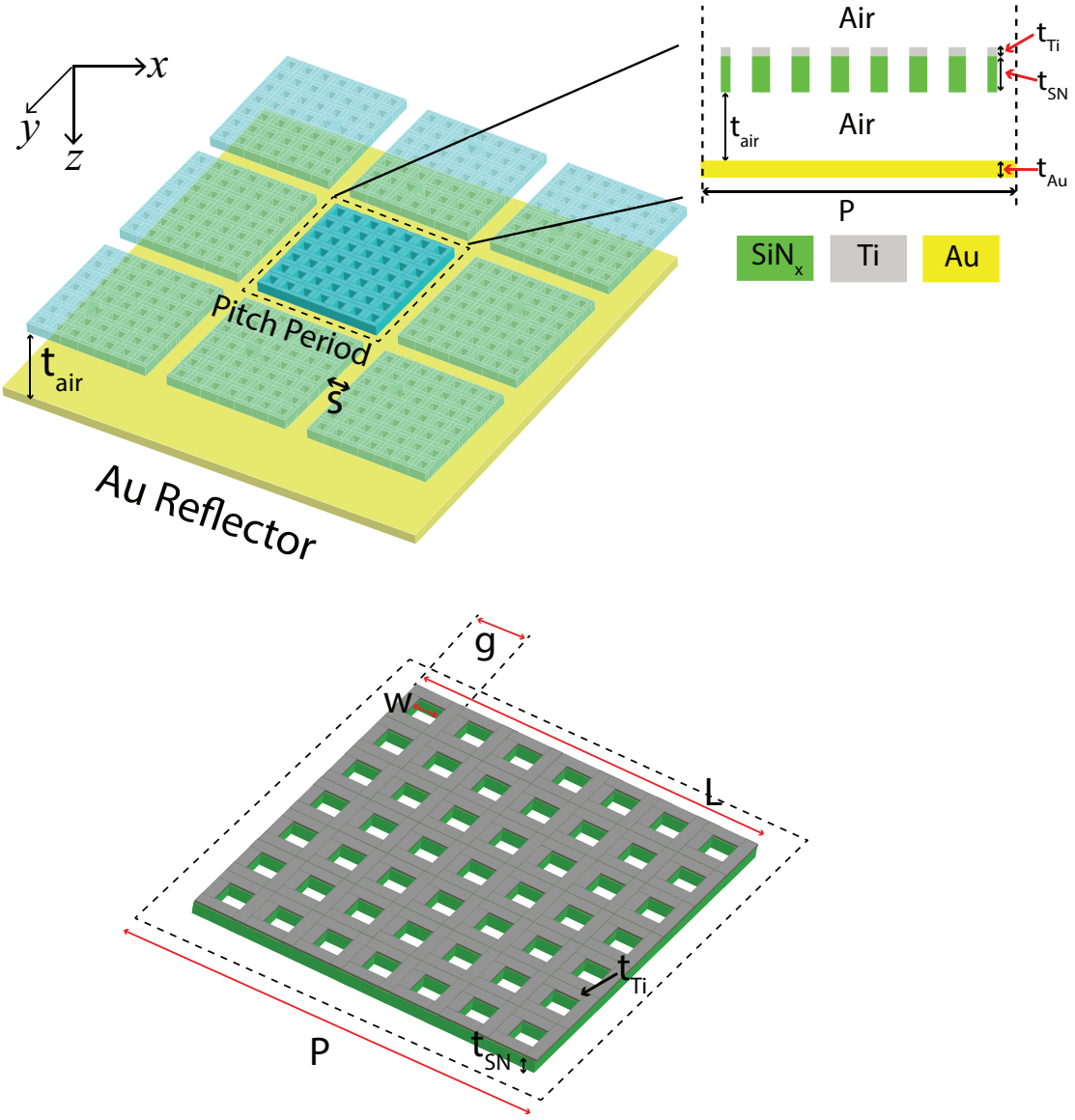

Figure 4.1: Schematic illustration of the subwavelength perforated infrared absorber. Pitch period P, solid pitch length L, grid unit period g, and perforation size w are highlighted along with the Ti and SiN_x thicknesses, t_{Ti} and t_{SN}. A bottom Au reflector (thickness t_{Au}) is placed underneath an air gap of t_{air} ensuring a quarter-wave anti-resonance ($\mathrm{m}\lambda/4$) condition.

couple evanescent LWIR light in the gaps as part of the pixel absorption. The structure is placed above a gold (Au) reflector at a gap distance t_{air} of $\sim$2.3 μm, ensuring a quarter-wave anti-resonance (m$\lambda/4$) condition that boosts the optical absorption across the 8$-$12 μm region. Such backside reflectors have been used in previously reported infrared absorbers [107, 132].

To ensure LWIR broadband absorption with a small mass, the subwavelength grids are formed with lossy metal and dielectric layers. Enhanced absorption due to lossy dielectrics have already been reported in previous articles [102, 133, 134]. Compatibility with common microfabrication technology makes SiO_2 and SiN_x two of the simplest choices for lossy dielectrics in the infrared regime. SiO_2 has a very sharp absorption peak at $\sim$9.22 μm, resulting in highly dispersive characteristics in the LWIR [135]. SiN_x has multiple vibrational phonon peaks in between 8 and 12 μm, which correspond to a comparatively moderate dispersion and broader absorption profile in the LWIR [136]. Therefore, SiN_x is considered as our lossy dielectric. The addition of a thin metal layer on top of the dielectric layer can significantly reduce the quality factor and broaden the entire absorption band [137]. We choose Ti as the metal layer due to its excellent broadband dispersion in the LWIR [138].

The thicknesses of Ti (t_{Ti}) and SiN_x (t_{SN}) layers are taken as 20 nm and 200 nm, respectively. The thicker dielectric layer enhances the evanescent light coupling in the optical waveguide [102]. To realize optical absorption in the perforated structure, we need to perform an effective medium analysis. Note that the grid unit period g and perforation length w are well below the wavelengths of light in consideration, therefore an effective medium approximation can be applied for the subwavelength grids [139]. Moreover, note that the effective medium approximation has been previously reported in analyzing the optical absorption of periodic grating structures [140, 141, 142]. Fig. 4.2(a) presents the schematic of a pitch period with optical permittivities ε_{Ti}, ε_{SN}, ε_{Au}, and ε_{a} for Ti, SiN_x, Au and air, respectively. All necessary parameters are highlighted in the same manner as Fig. 4.1. Optical indices of Ti, SiN_x, and Au in the LWIR, i.e.,

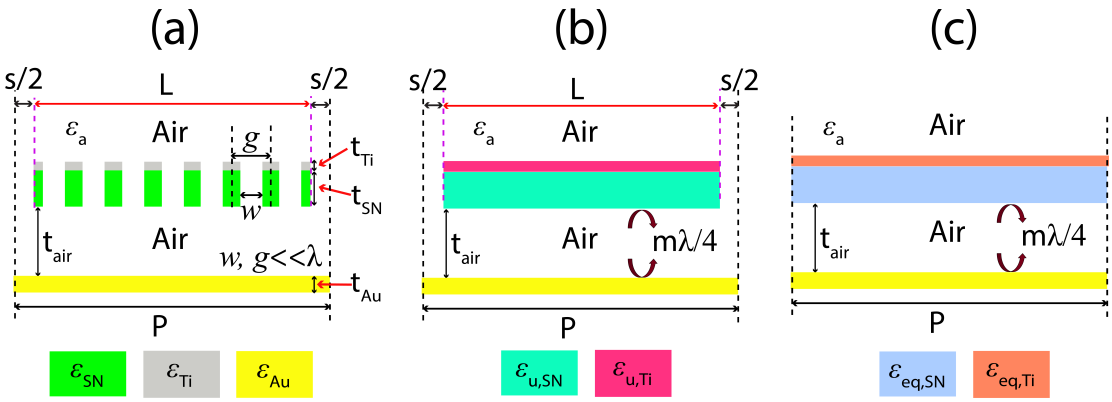

Figure 4.2: (a) Schematic illustration of a pitch period of the Ti-SiN_x perforated absorber. All the necessary parameters are highlighted along with optical permittivities $\varepsilon_{\mathrm{Ti}}$, $\varepsilon_{\mathrm{SN}}$, $\varepsilon_{\mathrm{Au}}$, and ε_{a} for Ti, SiN_x, Au, and air, respectively; Equivalent multilayer models where the Ti and SiN_x layers are portrayed as effective homogeneous layers (b) without and (c) with consideration of the air gap s around solid pitch length L.

8-12 μm are presented in Appendix D. Fig. 4.2(b) shows the homogeneous films of the subwavelength grids, whose optical permittivities can be calculated from the effective medium approximation [143, 144, 145] as,

$$\varepsilon_{\mathrm{u,x}} = f\varepsilon_{\mathrm{x}} + (1-f)\varepsilon_{\mathrm{a}}, \tag{4.1}$$

where $\varepsilon_{\mathrm{u,x}}$ is the effective permittivity of the films, with x=Ti or SiN_x. f corresponds to the linear duty cycle, as if $f = 1 - {}^{w}/_{g}$, which in turn defines the fractional area filled by the solid materials (in other words, fill factor). Note that $\varepsilon_{\mathrm{u,x}}$ only considers grid units within the solid pitch length. If air gap s around solid pitch length L is also considered, the equivalent homogeneous permittivity of the absorber pitch can be modeled from the effective grating theory [146, 147] as (in Fig. 4.2(c)),

$$\varepsilon_{\mathrm{eq,x}} = \varepsilon_{\mathrm{a}} + (\varepsilon_{\mathrm{u,x}} - \varepsilon_{\mathrm{a}}) \left(\frac{L}{P}\right), \tag{4.2}$$

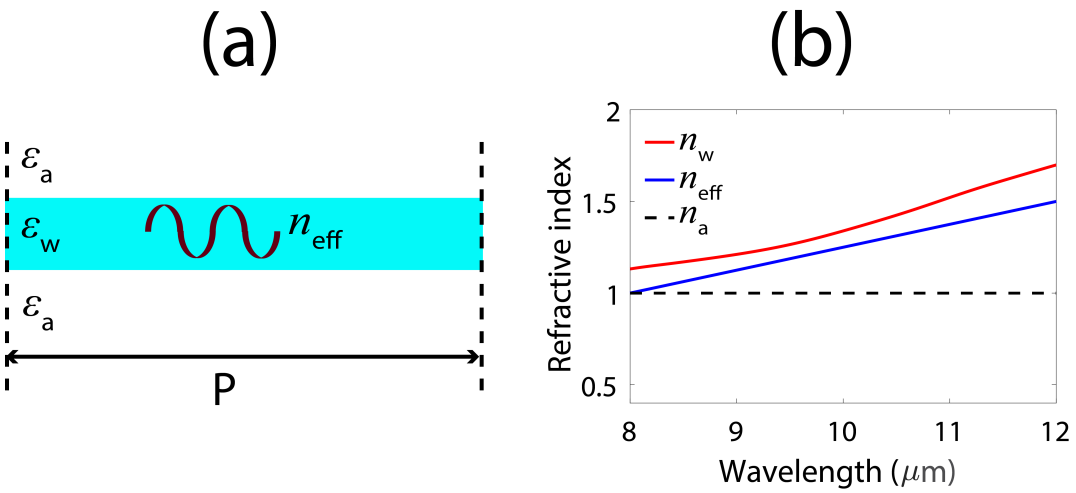

Figure 4.3: (a) Schematic illustration of a single layer absorber model with effective permittivity of ε_{w}. The effective index of the guided modes is presented as n_{eff}. A guided mode can be excited if $\sqrt{\varepsilon_{\mathrm{a}}} \leq |n_{\mathrm{eff}}| < \sqrt{\varepsilon_{\mathrm{w}}}$. (b) Calculated refractive indices of the absorber layer ($n_{\mathrm{w}} = \sqrt{\varepsilon_{\mathrm{w}}}$), surrounding air medium ($n_{\mathrm{a}} = \sqrt{\varepsilon_{\mathrm{a}}}$), and guided mode in the LWIR region.

where $\varepsilon_{\mathrm{eq,x}}$ is the equivalent homogeneous permittivity of the films for the pitch period, with x=Ti or SiN_x. It is noted that effective grating theory applies for pitch periods less than or comparable to the illumination wavelengths [146, 147].

To understand how the light gets coupled inside the effective grating pitches, a common approach is to analyze the guided mode resonance (GMR) techniques. In general, guided resonant modes can be coupled into a waveguide when the mode propagation index is higher than the surrounding medium but lower than the optical index of the waveguide. Fig. 4.3(a) shows a schematic illustration of the Ti-SiN_x absorber as a single layer model. Such a single-layer model can be used in analyzing the optical behavior of perfect absorbers [148]. The overall permittivity of the single layer can be calculated from the thicknesses and equivalent homogeneous permittivity as [149], $\varepsilon_{\mathrm{w}} = \frac{t_{\mathrm{Ti}}}{t_{\mathrm{Ti}}+t_{\mathrm{SN}}}\varepsilon_{\mathrm{eq,Ti}} + \frac{t_{\mathrm{SN}}}{t_{\mathrm{Ti}}+t_{\mathrm{SN}}}\varepsilon_{\mathrm{eq,SN}}$. The surrounding medium is air, so $\varepsilon_{\mathrm{a}} = 1$. The effective index of refraction of the guided modes can be expressed as [150, 151],

$n_{\text{eff}} = \sqrt{\varepsilon_{\text{a}}} \sin\theta_{\text{inc}} - m\frac{\lambda}{P}$, where θ_{inc} is the incident angle of light, m is the diffraction order, P is the absorber period, and λ is the wavelength of light. A guided mode can be excited if the effective index n_{eff} satisfies the condition as [59, 152],

$$\sqrt{\varepsilon_{\text{a}}} \leq |n_{\text{eff}}| < \sqrt{\varepsilon_{\text{w}}}, \tag{4.3}$$

For further illustration, Fig. 4.3(b) presents the refractive index of the absorber from a single-layer model n_{w} (i.e., $n_{\text{w}} = \sqrt{\varepsilon_{\text{w}}}$), surrounding air medium n_{a} (i.e., n_{a}=1), and guided modes n_{eff} for the wavelength ranges from 8−12 μm. We assume the normal incidence of light and first-order diffraction (i.e., $m = \pm 1$) in this calculation. Moreover, optical properties of Ti and SiN_x are taken from Ordal *etal.* [153] and Kischkat *etal.* [154], respectively. It can be clearly observed that n_{eff} satisfies the condition stated in Eq. 4.3, therefore, guided mode coupling is possible in our LWIR absorber.

Based on guided mode resonance (GMR), the propagation waveguide modes in the single layer absorber with permittivity ε_{w} would be equal to the diffracted modes when [150, 151],

$$\tan(\kappa_{\text{i}} t) = \frac{\kappa_{\text{i}} \left(\gamma_{\text{i}} + \delta_{\text{i}}\right)}{{\kappa_{\text{i}}}^2 - \gamma_{\text{i}}\delta_{\text{i}}}, \tag{4.4}$$

where,

$$\begin{cases} \kappa_{\text{i}} = \sqrt{\varepsilon_w {k_0}^2 - {\beta_{\text{i}}}^2} \\ \gamma_{\text{i}} = \sqrt{{\beta_{\text{i}}}^2 - \varepsilon_{\text{inc}} {k_0}^2} \\ \delta_{\text{i}} = \sqrt{{\beta_{\text{i}}}^2 - \varepsilon_{\text{sub}} {k_0}^2} \\ \beta_{\text{i}} = k_0 n_{\text{eff}} \\ k_0 = {}^{2\pi}/_{\lambda} \end{cases} \tag{4.5}$$

where β is the effective wavevector of propagation, t is the total thickness of the waveguide, and ε_{inc} and ε_{sub} are the permittivity of the incident medium and substrate,

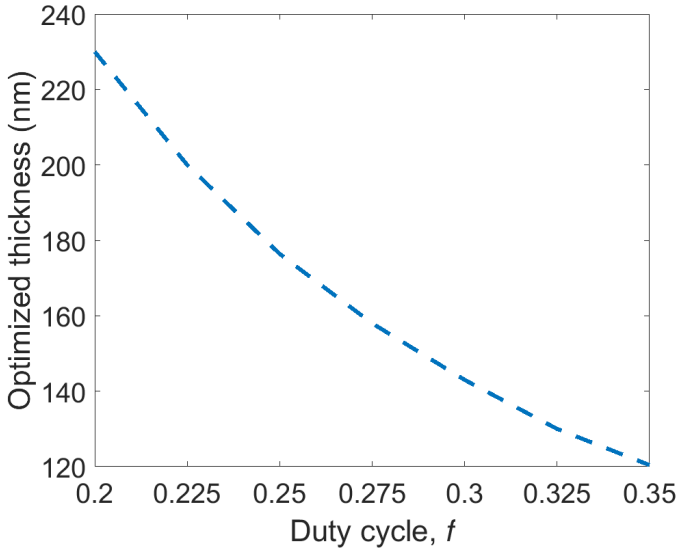

Figure 4.4: Optimum thickness for the fundamental guided modes in the single layer absorber with different duty cycle f.

respectively (for air, ε_{inc}=ε_{inc}=ε_{a}). Using this model, we can calculate the optimum thickness of the waveguide corresponding to the fundamental guided modes. Fig. 4.4 shows the optimum thickness of our single layer absorber (averaged over LWIR) with different duty cycles f (i.e., different perforation ratios $^{w}/_{g}$). It can be observed that a lower duty cycle corresponds to a larger thickness, which is quite evident from a previous article [155]. For a thickness of 220 nm, the optimum duty cycle is found as ∼0.21, which is quite close to our initial design of $^{w}/_{g} = 0.8$ (i.e., f=0.2).

Optical coupling inside the absorber layer can be better understood through a round-trip phase calculation of light. Fig. 4.5 presents the phase calculation throughout the 8−12 μm range. The inset shows a schematic illustration of an absorber with different phase components of light. When incident light gets diffracted and enters the absorber waveguide, it encounters several internal reflections at the interfaces of the waveguide (medium 2)−incident medium (medium 1), and waveguide (medium 2)−substrate (medium 3). Maximum light coupling is achieved when the round-trip phase meets the

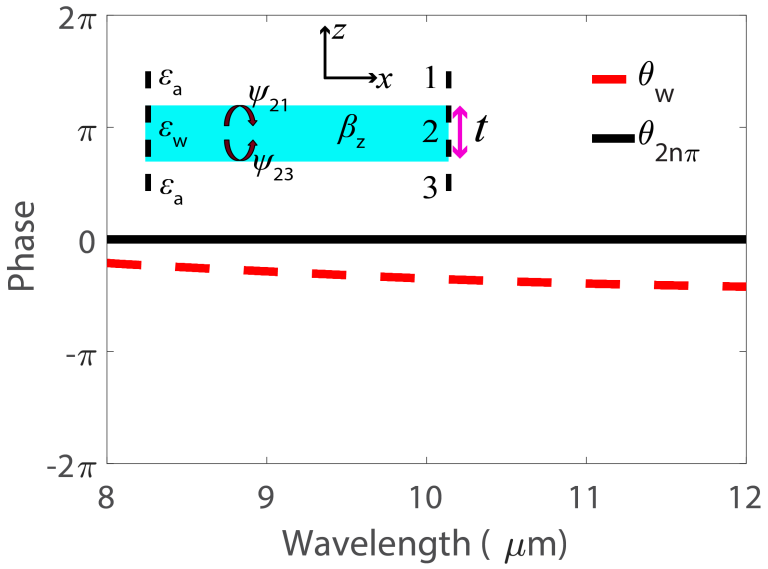

Figure 4.5: Round-trip phase of the light inside the absorber layer throughout the LWIR region.

following condition,

$$\psi = 2\beta_z t + \psi_{21} + \psi_{23} = 2n\pi, \qquad n = 0, 1, 2, \ldots$$
$$\text{where,} \tag{4.6}$$
$$\beta_z = k_0\sqrt{\varepsilon_{\mathrm{w}} - \varepsilon_{\mathrm{eff}}}$$

where, $\varepsilon_{\mathrm{eff}}$ is the effective permittivity of the propagating modes (i.e., $\varepsilon_{\mathrm{eff}} = {n_{\mathrm{eff}}}^2$), ψ_{21} and ψ_{23} are the phases of reflection at the waveguide−incident medium and waveguide−substrate, respectively. When ψ gets nearby to 2nπ, the waves that encounter multiple reflections inside the absorber waveguide get closer to interfere constructively and hence lead to resonant modes. From Fig. 4.5, it is quite evident that the phase gradually gets closer to 0 (i.e., n=0), which suggests for a high absorption in the long-wave infrared. Moreover, the wideband nature of the round-trip phase implies broadband optical absorption.

4.3 Calculation of optical absorption

4.3.1 Transfer matrix method

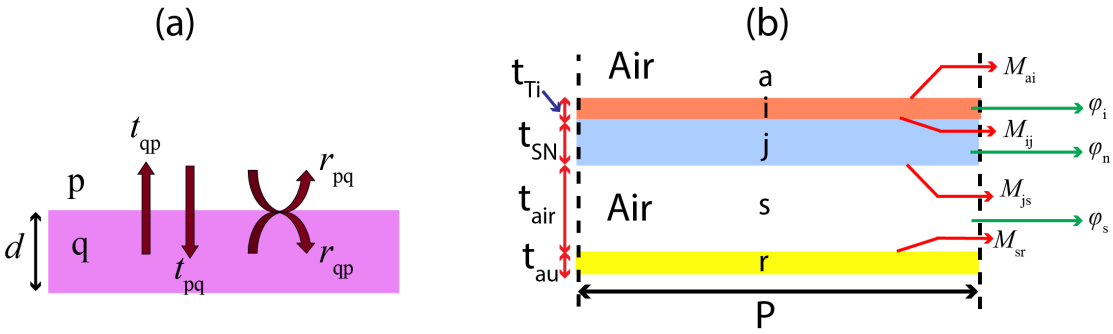

Figure 4.6: (a) Schematic illustration of a single homogeneous layer with thickness d and medium q. Light coming from medium p is incident on the interface between p and q, and reflection and transmission on the interface are described as follows: r_{pq} and t_{pq} are reflection and transmission coefficients from medium p to medium q, and r_{qp} and t_{qp} are reflection and transmission coefficients from medium q to medium p, respectively. Propagation through thickness d introduces a phase term described as, $\phi = \sqrt{\varepsilon_q}\left(\frac{2\pi}{\lambda}\right) d$, where ε_q is the effective permittivity and λ is the incident wavelength. (b) Schematic illustration of multiple layers in the absorber system, with equivalent homogeneous layers of Ti and SiN_x having permittivity of $\varepsilon_{eq,Ti}$ and $\varepsilon_{eq,SN}$, respectively. Incidence air/vacuum environment is described as medium 'a', Ti and SiN_x layers are described as medium 'i' and 'j', the bottom Au reflector is described as medium 'r', and air gap between absorber and reflector is described as medium 's'.

To calculate the optical absorption of the designed structure, we utilized a transfer matrix method through multiple layers of the absorber system (with a back reflector). For this approach, we considered the Ti and SiN_x layers as equivalent homogeneous films with permittivities of $\varepsilon_{eq,Ti}$ and $\varepsilon_{eq,SN}$, as shown in Fig. 4.2(c). Initially, we derived the transfer matrix for the electric field from each individual layer. As in Fig. 4.6(a), the transfer matrix of a homogeneous layer with medium q at an interface with medium p can be determined from the relation between the transfer matrix and reflection-transmission

coefficients as,

$$M_{\mathrm{pq}} = \frac{1}{t_{\mathrm{qp}}} \begin{bmatrix} t_{\mathrm{pq}} t_{\mathrm{qp}} - r_{\mathrm{pq}} r_{\mathrm{qp}} & r_{\mathrm{qp}} \\ -r_{\mathrm{pq}} & 1 \end{bmatrix} \tag{4.7}$$

where, t_{pq}, t_{qp} are forward (medium p to medium q) and backward (medium q to medium p) transmission coefficients and r_{pq}, r_{qp} are reflection coefficients at the front (medium p) and back (medium q) sides of the interface, respectively. In addition, propagation through the homogeneous layer with thickness d can be described through the propagation transfer matrix as,

$$\varphi_{\mathrm{q}} = \begin{bmatrix} e^{j\phi} & 0 \\ 0 & e^{-j\phi} \end{bmatrix}, \qquad \phi = \sqrt{\varepsilon_{\mathrm{q}}} \left(\frac{2\pi}{\lambda} \right) d \tag{4.8}$$

where, ε_q is the permittivity of the individual layer. As shown in Fig. 4.6(b), our multiple-layered system consists of a front air interface (medium a), a Ti layer with permittivity $\varepsilon_{\mathrm{eq,Ti}}$ and thickness t_{Ti} (medium i), a SiN_x layer with permittivity $\varepsilon_{\mathrm{eq,SN}}$ and thickness t_{SN} (medium j), an air spacer with permittivity ε_a and thickness t_{air} (medium s), and an Au film as a back reflector with permittivity $\varepsilon_{\mathrm{Au}}$ (medium r) and thickness t_{Au}. All the individual transfer matrices then can be multiplied to obtain the total transfer matrix as, [156, 157],

$$M^{\mathrm{tot}} = M_{\mathrm{sr}} \varphi_s M_{\mathrm{js}} \varphi_{\mathrm{j}} M_{\mathrm{ij}} \varphi_{\mathrm{i}} M_{\mathrm{ai}} = \begin{bmatrix} M_{11} & M_{12} \\ M_{21} & M_{22} \end{bmatrix} \tag{4.9}$$

The total transfer matrix M^{tot} constitutes a full description of the multiple-layered absorber system, including cavity effects from the back reflector. Using the relation in Eq.‘4.9, the total reflection and transmission coefficients of the absorber model can be calculated as, $r^{\mathrm{tot}} = M_{21}/M_{22}$ and $t^{\mathrm{tot}} = M_{11} + (M_{21}/M_{22})\, M_{12}$, respectively. Then the total absorption can be calculated as, $A_{\mathrm{mul}} = 1 - R_{\mathrm{mul}} - T_{\mathrm{mul}} = 1 - \left|r^{\mathrm{tot}}\right|^2 - \left|t^{\mathrm{tot}}\right|^2$.

4.3.2 Numerical simulation

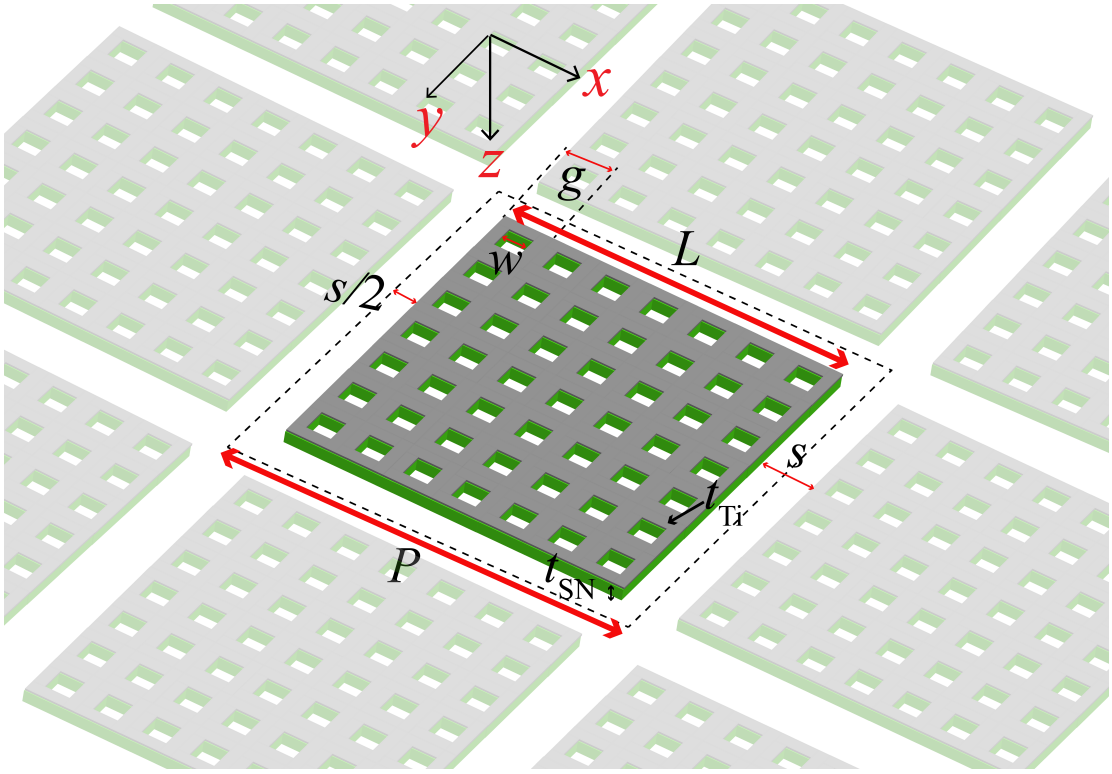

Figure 4.7: Conceptual illustration of 3D array of Ti-SiN_x perforated absorber pixels with all necessary parameters. To avoid large memory allocation for computation, we numerically calculated the optical absorption of a single pixel absorber, with periodic boundary conditions along the horizontal axes (i.e., x- and/or y-axis) and perfectly matched layer condition along the vertical axis (i.e., z-axis).

Figure 4.7 shows a conceptual illustration of a 3D array of Ti-SiN_x perforated absorber pixels with all the spacing parameters. The optical absorption of the structure was numerically analyzed by a finite difference time domain technique (FDTD) in Ansys Lumerical [158]. Both 3D and 2D simulations of the absorber were performed. As an enormous memory allocation was required for simulating the whole array, the optical absorption was calculated considering an absorber pitch period (highlighted in Fig. 4.7), with periodic boundary conditions along the horizontal directions (i.e., x- and/or y-axis)

Table 4.1: Parameters used in the optical simulation

Notation and meaning	**Value of the parameter and unit**
P, pitch period	8 μm
L, solid pitch length	7 μm
g, grid unit period	1 μm
w, perforation width	0.8 μm
s, air gap between pitch periods	1 μm
t_{Ti}, thickness of Ti layer	20 nm
t_{SN}, thickness of SiN_x layer	200 nm
t_{air}, air spacer between absorber and bottom reflector	2.3 μm
t_{Au}, thickness of bottom Au reflector	120 nm

and with perfectly matched layer (PML) condition along the vertical direction (i.e., z-axis). PML implies that no light would be reflected back from the boundaries. For the 2D simulation setup; on the x-axis, a periodic boundary condition was used, and on the z-axis, a PML condition was used. In both cases, the infrared light was a plane wave incident normally on the absorber, with wavelengths ranging from $8-12$ μm. From previous articles [153, 154, 159], the frequency-dependent optical properties (refractive index n and absorption coefficient k) were implemented. In all simulations, a mesh size of 100 nm was employed along the horizontal direction (i.e., x- and/or y-axis), and 1 nm is employed along the propagation direction (i.e., z-axis). Due to the opacity of the Au bottom reflector, optical transmission out of the system was 0, i.e., $T_{\mathrm{num}} \approx 0$. Therefore, the numerical absorption was calculated as $A_{\mathrm{num}} = 1 - R_{\mathrm{num}}$, where R_{num} is the FDTD calculated reflection from the designed absorber.

All the necessary parameters used in the transfer matrix and FDTD methods are presented in Table 4.1. Fig. 4.8 presents the spectral LWIR absorption of our designed structure calculated from both transfer matrix and FDTD techniques. It can be clearly observed that both simulations show broadband absorption throughout the 8-12 μm range are in close proximity to each other. The average absorption from the transfer

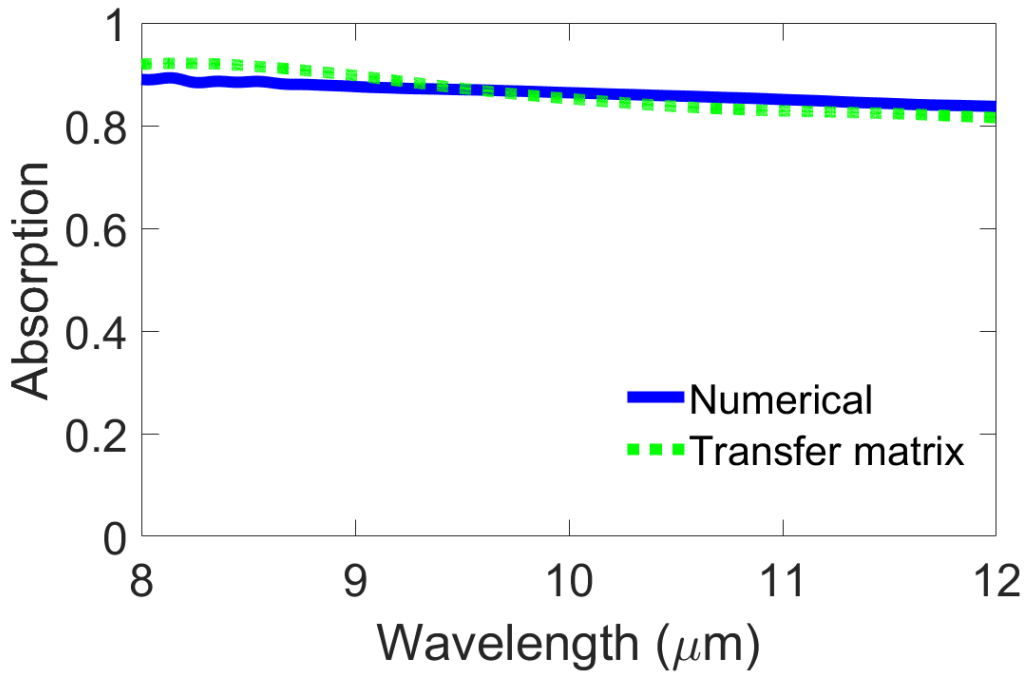

Figure 4.8: Spectral LWIR absorption of designed Ti-SiN$_x$ perforated absorber calculated from transfer matrix method and numerical FDTD technique. All the necessary parameters used in the simulation are presented in Table 4.1.

matrix and FDTD techniques can be found in ∼86% and ∼88%, respectively. It should be noted that parameters presented in Table 4.1 provide a pitch area filled by solid materials of ∼17.6 μm^2, which is quite small compared to the geometrical pitch area of 64 μm^2. Therefore, excellent broadband absorption (>85%) can be possible from our perforated absorber with a fill factor of only ∼27%.

4.4 Analysis of optical absorption

In this section, we investigate the absorption characteristics of our absorber by varying the design parameters of the subwavelength grids. Fig. 4.9 presents the LWIR absorption

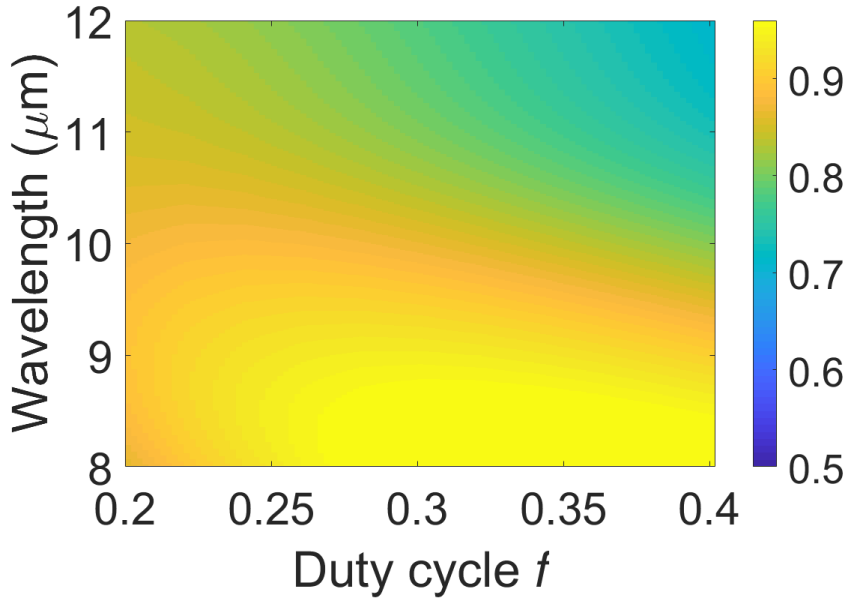

Figure 4.9: Spectral LWIR absorption of designed Ti-SiN$_x$ perforated absorber with different duty cycle f. The grid period g is fixed at 1 μm.

of our Ti-SiN$_x$ absorber with different duty cycle f. With a fixed grid period g of 1 μm, the grid width h and perforation width w would vary as, $h = f \times g$ and $w = (1 - f) \times g$. From Fig. 4.9, it can be observed that higher f gradually lowers the absorption in the upper end of the 8-12 μm range. This can be attributed to the guided mode coupling analysis shown in Fig. 4.4. When the grid width is larger than the optimum dimension, the propagating modes tend to scatter and leak out of the waveguide for particular wavelengths, which results in a degradation of the broadband absorption. This concept also applies for grid unit periods. Fig. 4.10 shows the LWIR absorption of the absorber with different grid periods g, while duty cycle f is fixed at 0.2. Higher g significantly lowers the overall broadband absorption, which implies that different grid periods would require different optimum grid widths (i.e., f). However, from both Figs. 4.9 and 4.10, optimum broadband absorption can be observed when f=0.2 for g=1 μm. Fig. 4.11 shows a spatial Poynting vector ($|S| = |E \times H|$) distribution of

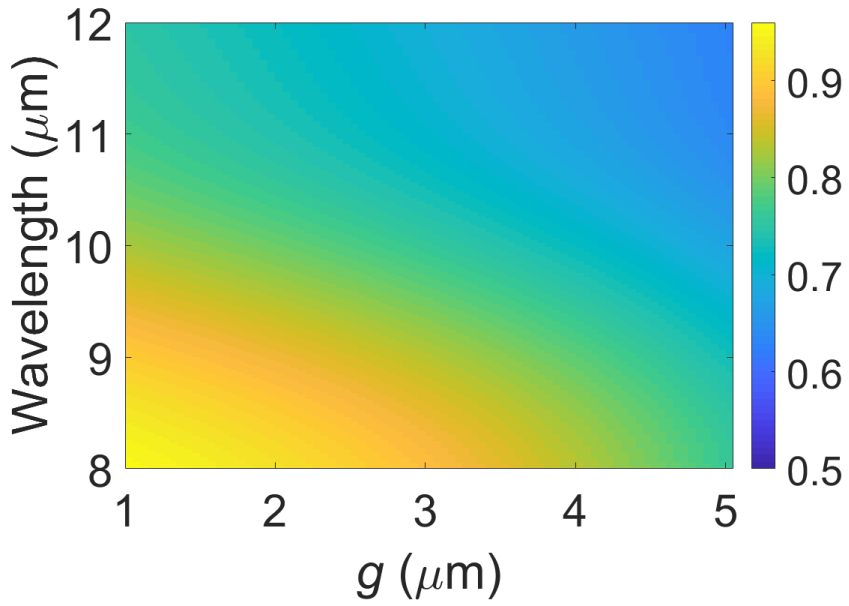

Figure 4.10: Spectral LWIR absorption of designed Ti-SiN$_x$ perforated absorber with different grid period g. The duty cycle f is fixed at 0.2.

the absorber, highlighting the resonant guided modes in the subwavelength grids when f=0.2 for g=1 μm at incident light λ=8 μm.

4.5 Performance analysis with absorption per unit thermal mass

To understand optimum coupling with a minimum amount of material, we performed a comparative analysis of our designed absorber with previously reported LWIR broadband absorbers. It should be noted that when the array of periods or pixels form an absorber area with lateral length L_{abs} (i.e., area is $L_{\text{abs}} \times L_{\text{abs}}$) much larger than the operating wavelengths, the total amount of material proportionately increases with the area, although the total absorption may not increase significantly [161]. Therefore, to analyze the overall quality of the absorber, the absorption may need to be normalized to

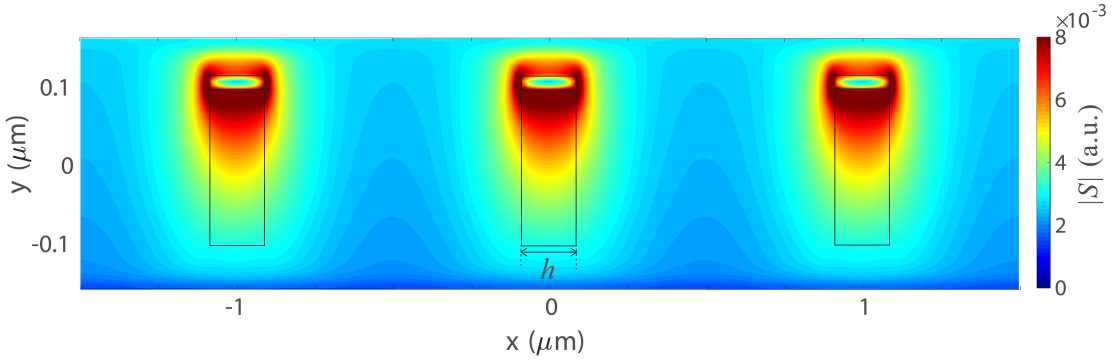

Figure 4.11: Calculated spatial Poynting vector distribution in the perforated absorber, showing the resonant modes in the subwavelength grids when g=1 μm and f=0.2 at λ=8 μm.

Table 4.2: Average absorption, thermal mass, and resultant absorption per unit mass (APM) of our designed absorber with different types of structures

Absorber	A_{avg} (%)	Thermal mass (kg)	Average APM (kg^{-1})	$\frac{APM_{Ti-SiN_x}}{APM_{otherworks}}$	Ref.
Ti-SiN_x	88	1.27×10^{-13}	6.8×10^{12}	1	this work
Al-Si-Al	93	2.38×10^{-12}	3.9×10^{11}	17.4	[121]
Si-SiO_2-Si	90	1.34×10^{-12}	6.7×10^{11}	10.1	[126]
Ti-Ge-Ti	86	1.82×10^{-12}	4.7×10^{11}	14.5	[127]
NiCr (Ge spacer)	80	2.83×10^{-12}	2.83×10^{11}	24	[115]

both thermal mass and area. In other words, performance metric can be defined as 'absorption per unit mass' (APM) for a comparative analysis, when a common absorption area is considered for all of the absorbers.

To compare with state-of-the-art works, we considered different types of structures, including metamaterials, metasurfaces, and plasmonic absorbers. For example, Ustun *et al.* [121] proposed a fully functional double-layer metamaterial nearly perfect absorber, which consists of two pairs of Al−Si−Al films along with a Si substrate. Gorgulu *et al.* [126] reported an ultra-broadband absorber consisting of symmetric square Si gratings on a SiO_2 thin film and Si substrate. Later on, Zhou *et al.* [127] reported a similar absorber structure made from circular Ti gratings, a Ge thin film, and a Ti continuous

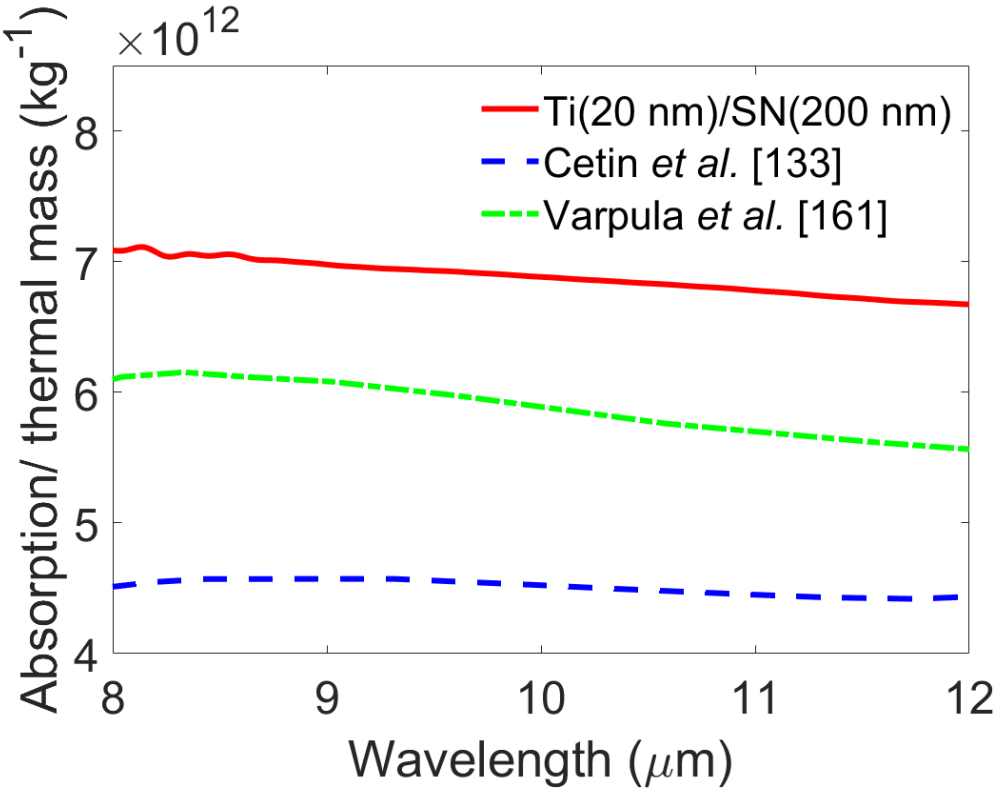

Figure 4.12: Comparative analysis of the absorption per unit thermal mass (APM) of our structure with very recently reported metal-dielectric broadband metastructures by Cetin *et al*. [132] and Varpula *et al*. [160].

film as a back reflector. Both of these works ([126] and [127]) use propagating surface plasmon (PSP) resonances to analyze the optical absorption. Jung *et al*. [115] presented the broadband LWIR absorption in a NiCr perforated metasurface, formed with a Ge spacer and a bottom Ag reflector. To illustrate the overall performance, Table 4.2 shows the average LWIR (λ ~8−12 μm) absorption, amount of thermal mass, and resultant absorption per unit mass (APM) of all of the broadband absorbers. Note that we considered a fixed absorption area of 24 μm × 24 μm for these structures in Table 4.2. It can be observed that all the reported works show an average absorption in between 80−93%, but require a total mass of ~10^{-12} kg. Our Ti-SiN$_x$ structure is designed with

a mass of 1.27×10^{-13} kg while maintaining an average absorption of 88%. As a result, our absorber shows an average APM of 6.8×10^{12} kg^{-1}, which is an order of magnitude larger than other state-of-the-art broadband absorbers.

Recently, a couple of metal-dielectric perforated meta structures have been reported with a m$\lambda/4$ air spacer, which utilizes effective sheet resistance matching for broadband absorption. Cetin *et al.* [132] proposed a NiCr (19 nm) on SiN_x (230 nm) broadband metasurface, with a pitch period of 25 μm, grid unit of 3 μm, and perforation ratio of 0.77. Later on Varpula *et al.* [160] reported a TiN (50 nm) on poly-Si (70 nm) thermoelectric infrared bolometer, with a pitch period of 24.6 μm, a grid unit of 3 μm, and a perforation ratio of 0.8. Details on the optical sheet resistance analysis and its application to our designed absorber have been discussed in Appendix C. To provide a comparative analysis, Fig. 4.12 presents the spectral absorption per unit mass (APM) of our structure in the LWIR range, along with the works of Cetin *et al.* and Varpula *et al.* It can be observed that the NiCr on SiN_x metastructure shows nearly uniform APM with an average value of $\sim4.5\times10^{12}$ kg^{-1}. Due to having a smaller thickness of poly Si, the thermoelectric TiN on poly Si absorber shows comparatively higher APM, with an average value of $\sim6\times10^{12}$ kg^{-1}. With $\sim6.8\times10^{12}$ kg^{-1}, our designed absorber shows average APM $\sim$51% higher than that of the NiCr on SiN_x metastructure and $\sim$13% higher than that of the TiN on poly-Si bolometer.

4.6 Summary

In summary, we reported that enhanced absorption across the LWIR can be possible with a minimum amount of material using pixel designs that incorporate subwaveleg-nth interference and evanescent field coupling in the air holes within and around the pitches or pixels. In effect, the overall absorption area per pitch period becomes much larger than the amount of solid area used to create it. Lossy Ti$-SiN_x$ waveguide grids with low fill factors and periodic open gaps were used to form the perforated pixel.

Through theoretical analysis, we analyzed effective light coupling within the Ti$-$SiN$_x$ films. Using the transfer matrix method and numerical FDTD technique, we calculated the spectral absorption throughout the LWIR region. Excellent broadband absorption is observed, with an average value of $\sim$86% for the transfer matrix method and $\sim$88% for the FDTD technique. Having a thermal mass of $\sim 1.27\times10^{-13}$ kg, our Ti-SiN$_x$ absorber shows at least $\sim$13% higher APM than most recently reported metastructures and around an order of magnitude higher than state-of-the-art metamaterials and plasmonic microstructures.

Chapter 5

Room Temperature Infrared Thermal Detector with High Absorption per unit Mass

This chapter describes the design, fabrication, and characterization of a highly sensitive infrared thermal detector operating at room temperature. With an infrared absorber having absorption per unit thermal mass (APM) higher than the Ti-SiN_x structure (described in the previous chapter), this thermal detector has the highest reported performance amongst the room temperature detectors in the LWIR region. This detector is a significant step towards the ultimate goal of achieving room temperature detectors with broadband detectivities approaching the background photon noise limit [162].

The first section describes the design details of the thermal detector. It also explains why the infrared absorber was slightly modified compared to the Ti-SiN_x design presented in the previous chapter. The second section describes the step-by-step fabrication process of the designed detector, including the difficult engineering challenges and possible solutions. Most of the fabrication works were performed in the Minnesota Nanofabrication Center (MNC) at the University of Minnesota. A small portion of the

fabrication was completed using a laboratory tool at Prof. Sarah Swisher's research facility. In the third section, the optical characterization of the fabricated detector is described in detail, including results and analysis.

5.1 Thermal Detector Design

Figure 5.1 presents a schematic illustration of our uncooled long-wave infrared (LWIR) thermal detector with subwavelength perforated absorber freely suspended by four straight tethers in air. Each tether has a length l of 100 μm and width b of 2 μm. The absorber consists of an array of square pitches with a periodicity P of 7.5 μm. Each pitch contains 16 nano-scale grid units (i.e., solid pitch length L), with each grid having a period g of 1.5 μm and a perforation size w of 1.2 μm (i. e., perforation ratio w/g=0.8 and grid stripe or width $h = g - w = 0.3$ μm). An air space, s of 1.5 μm is utilized around the solid absorber pitches designed to couple evanescent LWIR light in the gaps as part of the detector absorption. Being suspended in the air, the pitches are connected with small supporting legs with length l_c of 3 μm and width b_c of 1 μm. As discussed in chapter 4, the whole absorber array is situated above a gold (Au) reflector (thickness t_{Au} of 120 nm) at a gap distance t_{air} of $\sim$2.3 μm, ensuring quarter-wave anti-resonance (m$\lambda/4$) condition to boost up LWIR absorption [107, 132].

Unlike the metal-dielectric layers (i.e., Ti-SiN$_x$) discussed in chapter 4, the subwavelength grids are formed with three layers: Ti, SiN$_x$, and Ni as in a perforated metal-insulator-metal (M-I-M) configuration. The thicknesses t_{Ti}, t_{SN}, and t_{Ni} of the three layers are taken as 10 nm, 200 nm, and 10 nm, respectively. This is different from the conventional M-I-M absorbers previously reported [118, 119, 120, 121, 122, 126, 127], which utilize a continuous thick metal film as the bottom layer. The perforated Ti-SiN$_x$-Ni structure can enhance the LWIR absorption with even lower amount of mass than that of the Ti-SiN$_x$ structure discussed earlier. To illustrate this, Table. 5.1 presents a comparative analysis of the Ti-SiN$_x$-Ni and Ti-SiN$_x$ absorbers with different design

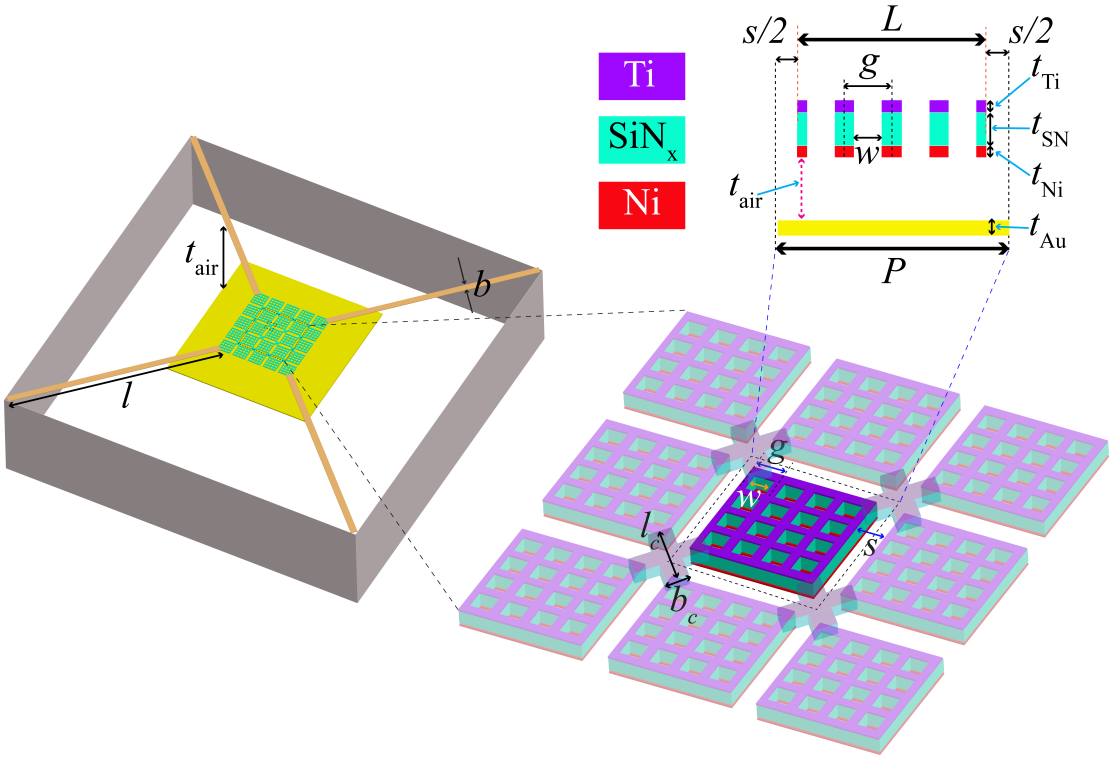

Figure 5.1: Schematic illustration of the long-wave infrared (LWIR) thermal detector with subwavelength perforated absorber suspended by four straight tethers, with length l and width b. The absorber design parameters are highlighted as: pitch period P, solid pitch length L, grid unit period g, perforation of grid w, and air space between pitches s. The subwavelength grids consist of of Ti, SiN_x, and Ni films in a perforated metal-insulator-metal (MIM) configuration, whose thicknesses are presented as t_{Ti}, t_{SN}, and t_{Ni}, respectively. The absorber pitches are connected by small supporting legs, with length l_{c} and width b_{c}. A bottom Au reflector with thickness t_{Au} is placed underneath an air gap of t_{air} ensuring a quarter-wave anti-resonance ($\mathrm{m}\lambda/4$) condition.

Table 5.1: Comparative analysis of proposed Ti-SiN$_x$-Ni and previously discussed Ti-SiN$_x$ absorbers with different design parameters

Notation and meaning	**Ti-SiN$_x$-Ni absorber**	**Ti-SiN$_x$ absorber**
P, pitch period	7.5 μm	8 μm
L, solid pitch length	6 μm	7 μm
g, grid unit period	1.5 μm	1 μm
w, perforation length	1.2 μm	0.8 μm
t_{Ti}, thickness of Ti	10 nm	20 nm
t_{SN}, thickness of SiNx	200 nm	200 nm
t_{Ni}, thickness of Ni	10 nm	0
A_{p}, solid (filled) area of the pitch	12.96 μm^2	17.64 μm^2
M_{p}, mass of the pitch	9.77×10^{-15} kg	1.25×10^{-14} kg

parameters. It can be observed that the Ti-SiN$_x$-Ni absorber has been designed with a pitch mass ∼22% lower than that of the Ti-SiN$_x$ absorber. In addition, the Ti-SiN$_x$-Ni pitch shows a fill factor (i.e., $FF = A_{\mathrm{p}}/P^2$) of 23%, whereas the Ti-SiN$_x$ pitch shows a fill factor of 27%.

Fig. 5.2 presents an LWIR spectrum of the absorption per unit thermal mass (APM) between the Ti-SiN$_x$-Ni and Ti-SiN$_x$ structures. For our comparative analysis, we consider 3×3 arrays with similar absorption areas; 22.5 μm × 22.5 μm for Ti-SiN$_x$-Ni and 24 μm × 24 μm for Ti-SiN$_x$. Note that the absorption profiles in this analysis were calculated using a finite difference time domain (FDTD) technique (discussed in chapter 4), and further details on the optical absorption of the Ti-SiN$_x$-Ni structure will be discussed in the following section. From Fig. 5.2, it is quite evident that the Ti-SiN$_x$-Ni structure shows an overall increase in the APM throughout the LWIR region. An average APM of $\sim7.8\times10^{12}$ kg^{-1} is observed, which is ∼15% higher than that of the Ti-SiN$_x$ structure.

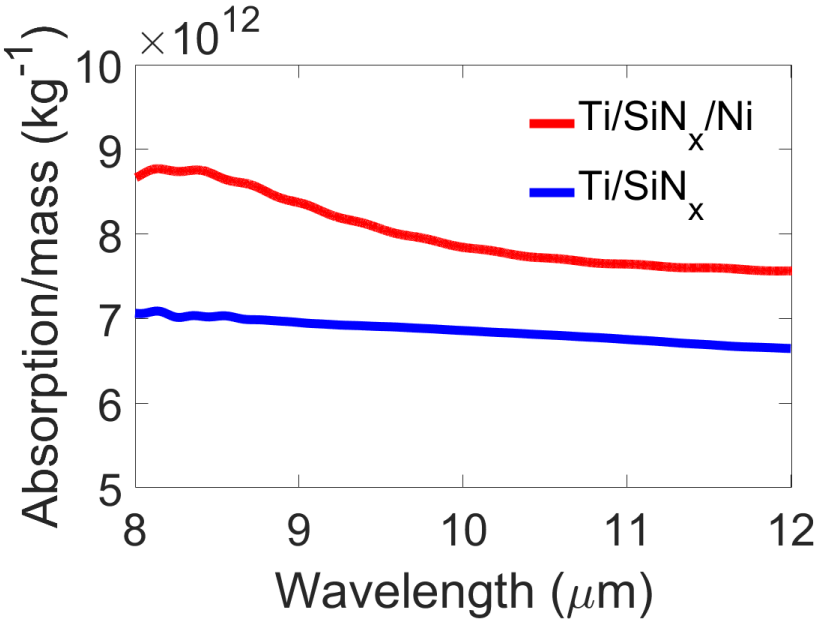

Figure 5.2: Spectral comparison of the absorption per unit thermal mass (APM) between the Ti (10 nm)−SiN_x (200 nm)−Ni (10 nm) design and the previously discussed Ti (20 nm)−SiN_x (200 nm) structure.

5.1.1 Effective Medium Model

To better understand the underlying mechanism for optical absorption in the perforated Ti-SiN_x-Ni structure, we need to perform an effective medium approximation. It should be noted that the grid unit period g, perforation length w, and air space between pitches s (i.e., $s = P - L$) are well below the wavelengths of the incident light in consideration. Therefore, an effective medium approximation can be applied to the subwavelength grids [148], just as described in chapter 4.

Fig. 5.3(a) presents the schematic illustration of a pitch period with optical permittivities $\varepsilon_{\mathrm{Ti}}$, $\varepsilon_{\mathrm{SN}}$, $\varepsilon_{\mathrm{Ni}}$, and ε_{a} for Ti, SiN_x, Ni, and air, respectively, with other necessary parameters same as highlighted in Fig. 5.1. Fig. 5.3(b) presents the equivalent homogeneous films of the subwavelength grids, whose optical permittivities can be calculated from the effective medium approximation [143, 144, 145] shown in Eqs. 4.1 and 4.2.

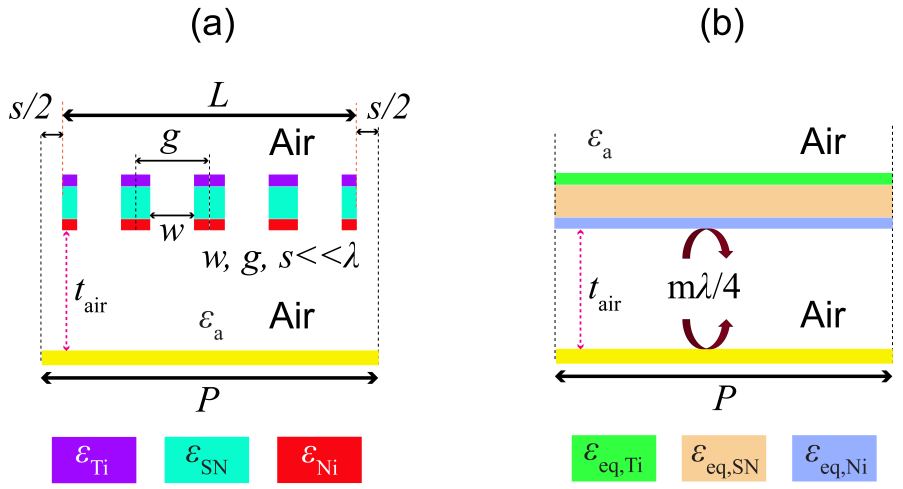

Figure 5.3: (a) Schematic illustration of a pitch period of the Ti-SiN$_x$-Ni perforated absorber. All the necessary parameters are highlighted along with optical permittivities $\varepsilon_{\mathrm{Ti}}$, $\varepsilon_{\mathrm{SN}}$, $\varepsilon_{\mathrm{Ni}}$, and ε_{a} for Ti, SiN$_x$, Ni, and air, respectively. (b) Equivalent multilayer model where Ti, SiN$_x$, and Ni layers are presented with effective homogeneous layers.

Due to their high effective permittivities, the Ti and Ni metal layers can be considered as "mirrors" that would trap the light inside the dielectric SiN$_x$ layer. Upon entering the structure, the incident light would reflect multiple times from each of the two metal films, forming a Fabry-Perot-like cavity. Maximum coupling can be achieved when the round-trip phase θ_{w} of this light meets the following condition [148, 163],

$$\theta_{\mathrm{w}} = \psi_{21} + \psi_{23} + 2\beta_z t_{\mathrm{SN}} = 2n\pi, \qquad n = 0, 1, 2\ldots\ldots, \tag{5.1}$$

where, ψ_{21} and ψ_{23} are phases of reflection at the interfaces of Ti/air and Ni/air, respectively. Considering $t_{\mathrm{Ti}}, t_{\mathrm{Ni}} << t_{\mathrm{SN}}$ and effective light coupling within the dielectric, $\beta = \sqrt{\varepsilon_{\mathrm{eq,SN}}}\left(\frac{2\pi}{\lambda}\right)$ is the propagating phase in the SiN$_x$ layer, where $\varepsilon_{\mathrm{eq,SN}}$ is the effective permittivity of SiN$_x$ and λ is the wavelength of light. When θ_{w} gets close to 2nπ, the waves that encounter multiple reflections inside the absorber waveguide tend to constructive interference and hence, lead to resonant cavity modes. From Fig. 5.4, it is quite evident that the phase gets closer to 0 (i.e., n=0) around 8−9μm, and moves

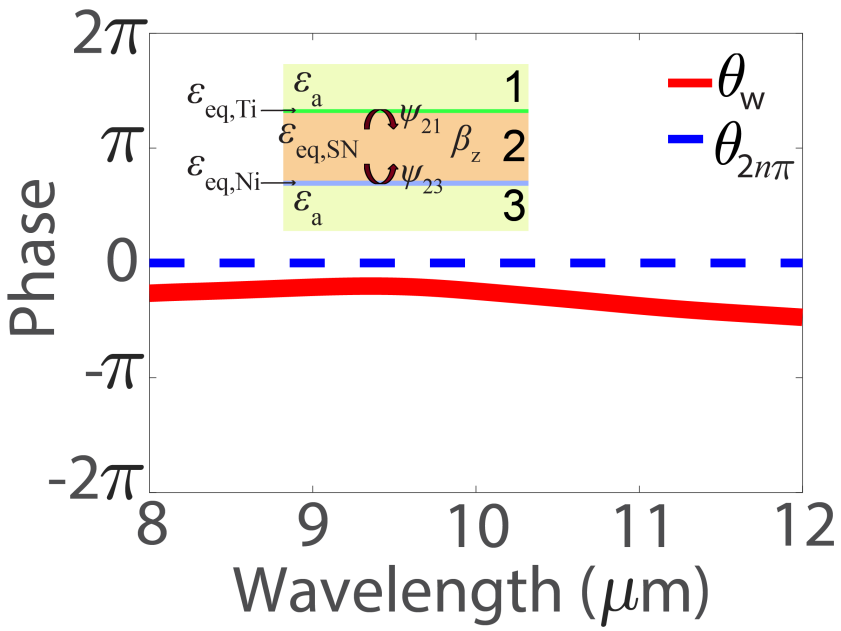

Figure 5.4: Round-trip phase of LWIR light inside the effective medium model of the Ti-SiN$_x$-Ni absorber. Inset depicts phases of reflection ψ_{21} and ψ_{23}, and propagating phase β_z inside the absorber model.

away from the 2nπ line in longer wavelengths. Therefore, higher absorption should be observed in shorter wavelengths. In addition, minimal dependence on wavelengths of the round-trip phase implies broadband optical absorption.

5.1.2 Calculation of optical absorption

To analyze the optical absorption of the Ti-SiN$_x$-Ni detector, we used both theoretical calculations and experimental measurements. For our theoretical analysis, we used the transfer matrix method and numerical FDTD techniques, details of which have been described in chapter 4. For our experimental verification, we used Fourier-transform infrared spectroscopy (FTIR) at the Characterization Facility of the University of Minnesota. A reflection spectrum R_{exp} was measured from the center 37.5 μm $\times$ 37.5 μm absorber membrane (i.e., 5$\times$5 pitch array) in the microscope after appropriate focus

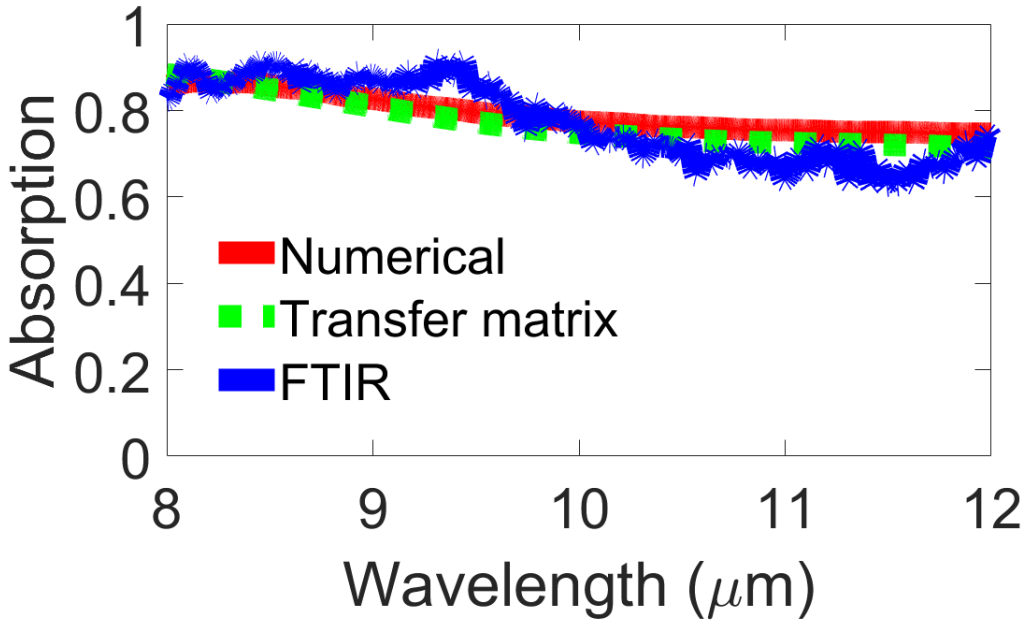

Figure 5.5: Spectral LWIR absorption measurements (FTIR) and simulations (transfer matrix and numerical FDTD) of the Ti-SiN$_x$-Ni detector.

and was referenced to a background spectrum measured from a gold (Au) mirror. The details of the fabrication of the detector will be discussed in the following section. Due to having a bottom Au reflector in the detector, the overall transmission T was assumed as 0. Therefore, the overall absorption A_{exp} was calculated from the reflection measurements as, $A_{\text{exp}} = 1 - R_{\text{exp}}$. Fig. 5.5 presents the absorption spectrum of the detector calculated from both theory (i.e., transfer matrix and numerical FDTD methods) and experiment (FTIR). It can be clearly observed that both simulations and measurements show broadband absorption throughout the $8-12$ μm and are in close proximity to one another. Absorption is found higher (>80%) in shorter wavelengths (i.e., $8-9\mu$m) and gradually gets lower (<80%) in longer wavelengths. This can be attributed to the round trip phase calculations from the Fabry Perot cavity resonance, as shown in Fig. 5.4. The slight discrepancy between simulations and measurements may occur due to scattering

losses in the back Au reflector of the detector.

5.1.3 Optimization of absorption

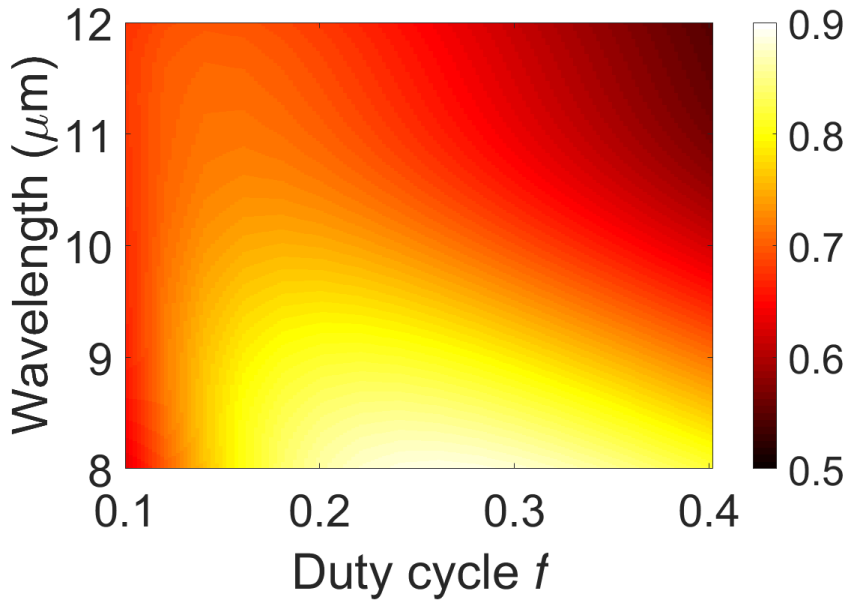

Figure 5.6: Spectral LWIR absorption of the Ti-SiN$_x$-Ni perforated absorber with different duty cycles f. The grid period g is fixed at 1.5 μm.

To extract enhanced performance from the Ti-SiN$_x$-Ni detector, it is important to understand how the detector absorption can be optimized based on different design parameters. Therefore, we analyzed the absorption characteristics using the numerical FDTD technique while varying different design parameters. Fig. 5.6 presents the spectral LWIR absorption of the detector membrane with different duty cycles f. The grid period g is fixed at 1.5 μm and other parameters are the same shown in Table. 5.1. The grid width h and perforation width w would vary as, $h = f \times g$ and $w = (1 - f) \times g$. Fig. 5.6 shows an increase and decrease in the absorption spectra, with optimum broadband absorption reaching near f=0.2. Such absorption characteristics can be attributed to the change in the optical impedance of the detector absorber, which originates from

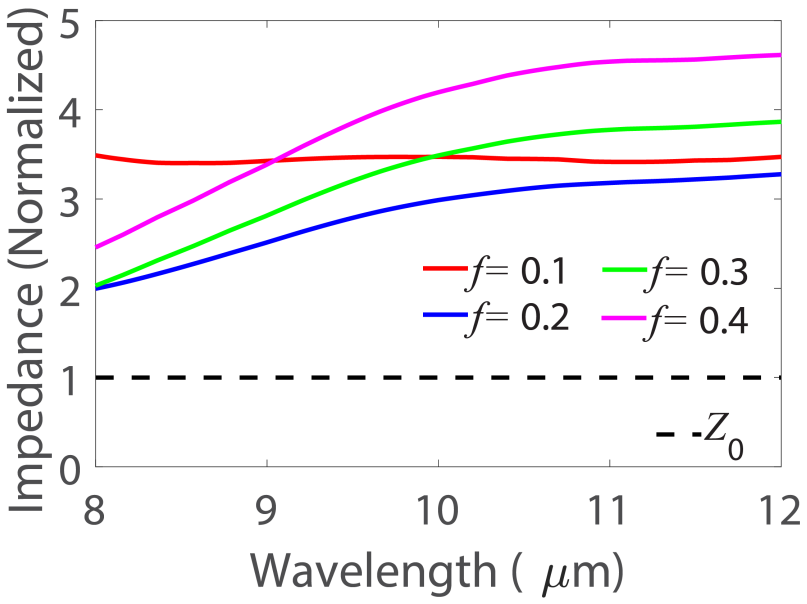

Figure 5.7: Normalized optical impedance of the Ti-SiN$_x$-Ni detector absorber in the LWIR range with different duty cycles f

the change in optical constants (e.g., refractive index and absorption coefficient) due to different f. Any change in the optical constants of materials would change the phase parameters presented in Eq. 5.1, and therefore, change the Fabry Perot resonance condition. To understand the changes in optical constants, Fig. 5.7 shows the effective optical impedance Z_{eff} of the detector absorber with different duty cycles, as calculated by the transfer matrix method. In general, the effective normalized impedance can be calculated from the following equation [164, 165],

$$Z_{\text{eff}} = \sqrt{\frac{(1+S_{11})^2 - {S_{12}}^2}{(1-S_{11})^2 - {S_{12}}^2}}, \tag{5.2}$$

where S_{11} and S_{12} are scattering matrix coefficients for reflection and transmission of the detector absorber. To enhance optical absorption, effective impedance Z_{eff} needs to get closer to the free space impedance Z_0 (here, Z_0=1). From Fig. 5.7, it can be

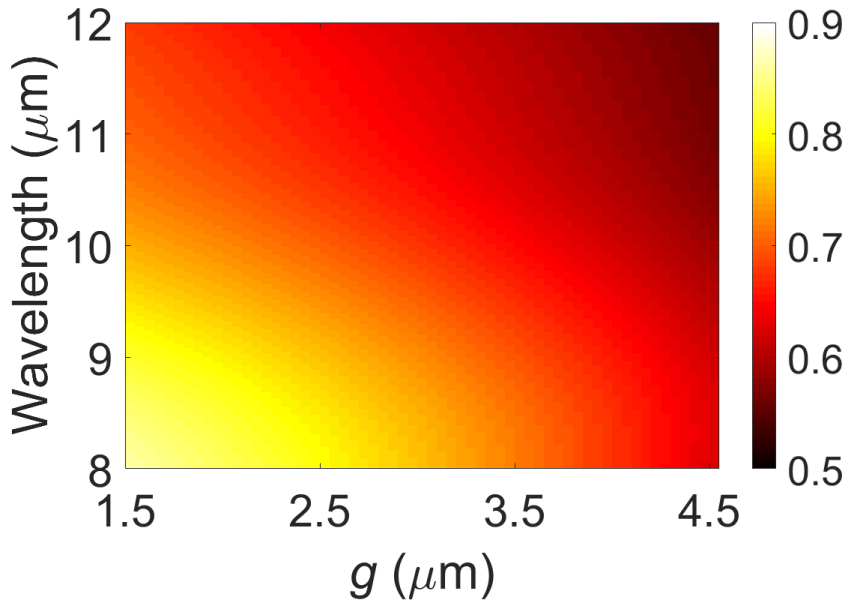

Figure 5.8: Spectral LWIR absorption of the Ti-SiN$_x$-Ni perforated absorber with different grid periods g. The duty cycle f is fixed at 0.2.

observed that Z_{eff} becomes minimum and gets the closest to the Z_0 line at f=0.2, which clearly indicates the optimum broadband absorption. It should be noted that Z_{eff} for f=0.1 appears to be almost indifferent to the LWIR wavelengths, which suggests the absence of Fabry Perot resonance.

At a fixed duty cycle (here, f=0.2), variation of grid periods g can change the optical constants, and hence, Z_{eff} of the MIM absorber. This would alter the Fabry Perot resonance modes by changing the reflection and propagation phases inside the absorber. For illustrating this, Fig. 5.8 shows the spectral LWIR absorption of the detector absorber with different g, when f is fixed at 0.2. Maximum absorption gradually decreases with increasing g, which can be attributed to the Z_{eff} becoming higher than Z_0.

The detector absorption can be optimized with different Ti, SiN$_x$, and Ni thicknesses. Fig. 5.9(a) presents the absorption spectra with different SiN$_x$ thicknesses t_{SN} when Ti

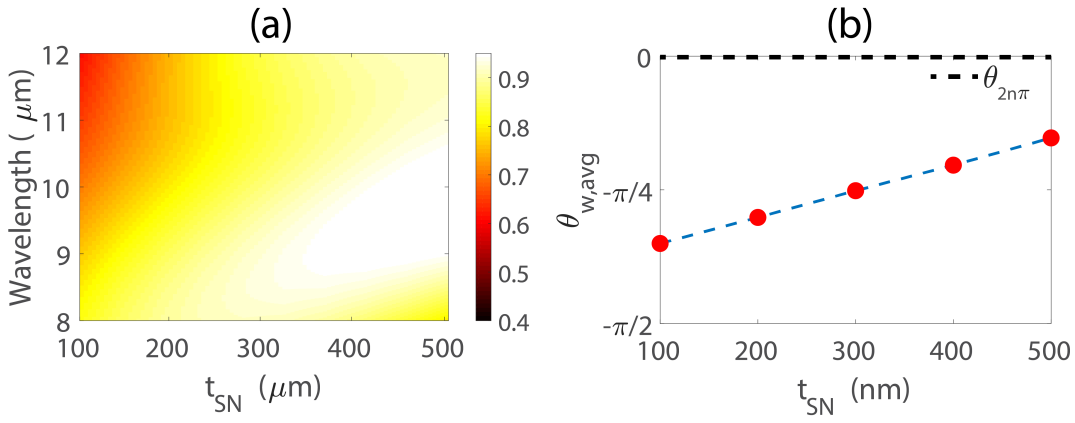

Figure 5.9: (a) Spectral LWIR absorption of the Ti-SiN_x-Ni perforated absorber with different SiN_x thicknesses t_{SN}. (b) Calculated round-trip phase averaged over the LWIR range inside the detector absorber with different SiN_x thicknesses.

and Ni thicknesses are fixed at 10 nm. Higher t_{SN} gradually increases the broadband absorption, which can be attributed to the round-trip phase θ_w of the Fabry Perot cavity modes. Fig. 5.9(b) shows that θ_w averaged over the LWIR range gradually increases with increasing t_{SN} and approaches near $2n\pi$ line, which explains the higher absorption characteristics. In addition, in Fig. 5.9(a) the maximum absorption peak gradually shifts to longer wavelengths. This can be realized from the optical constants of SiN_x in Fig. D.5, showing higher absorption coefficients in longer wavelengths (e.g., 11-12 μm). We wanted to design and fabricate our detector with a minimum amount of mass, therefore we chose t_{SN} as 200 nm.

Figs. 5.10(a) and 5.10(b) show the absorption spectra with different Ti (t_{Ti}) and Ni (t_{Ni}) thicknesses, respectively, when t_{SN} is fixed at 200 nm. From both figures, it is quite evident that higher metal thickness reduces LWIR absorption. However, the effects of t_{Ti} is quite different than those of t_{Ni}. To better understand this, Figs. 5.11(a) and 5.11(b) present the absorption spectra of Ti and Ni perforated films while placed above an Au reflector at $m\lambda/4$ gap. The metal layers would act as nanoscale metasurfaces with a quarter-wave cavity. Fig. 5.11(a) shows that higher t_{Ti} gradually shifts the

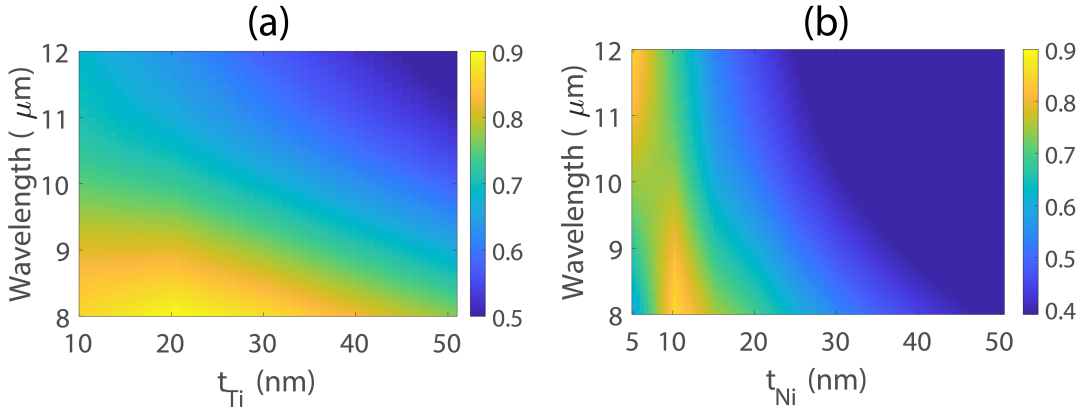

Figure 5.10: Spectral LWIR absorption of the Ti-SiN$_x$-Ni perforated absorber with different thicknesses of (a) Ti (t_{Ti}) and (b) Ni (t_{Ni}). (t_{SN}) is fixed at 200 nm.

metasurface absorption peak to shorter wavelengths (<8 μm), which implies a lesser contribution of Ti to the detector absorption. However, the maximum absorption still remains in the 8−12 μm range till t_{Ti}=20 nm, which explains the high absorption profile in Fig. 5.10(a). Fig. 5.11(b) shows that Ni metasurface reaches the maximum absorption profile in between 8-12 μm when t_{Ni}=10 nm. Below or above 10 nm, the metasurface absorption peak shifts out of the LWIR range. This explains the optimum absorption profile of the detector at t_{Ni}=10 nm in Fig. 5.10(b).

5.2 Detector Fabrication

This section outlines the details of the fabrication of the Ti-SiN$_x$-Ni infrared detector. A small portion of the fabrication process was performed in Prof. Sarah Swisher's research lab at the University of Minnesota Twin Cities. Apart from the step-by-step process, difficult engineering challenges during fabrication and possible solutions have been discussed.

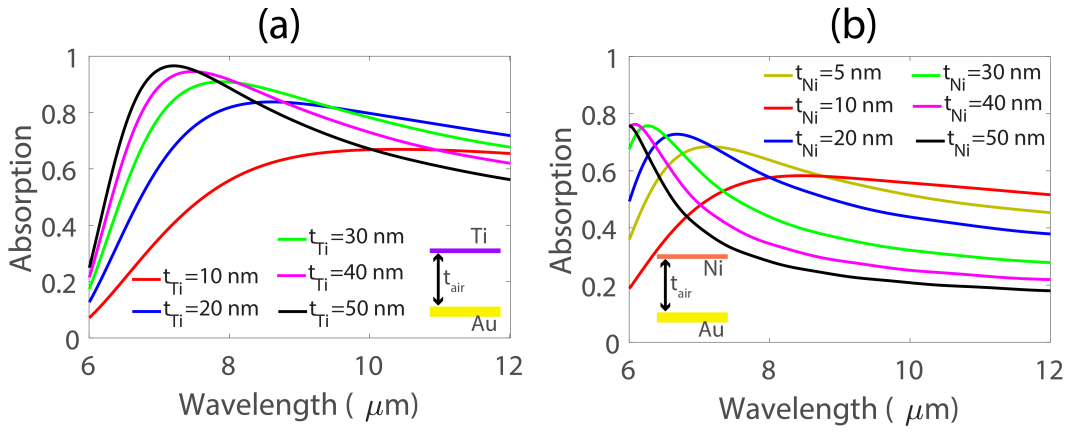

Figure 5.11: Spectral LWIR absorption of the (a) Ti and (b) Ni films with a bottom Au reflector at mλ/4 gap.

5.2.1 Sample Preparation

A 4-inch silicon (Si) wafer was used as the substrate of our infrared detector. Initially, the wafer was cleaned in order to remove any residue or particulates. This involves a 1/2 minute rinse with deionized (DI) water, then a soak with isopropyl alcohol (IPA) followed by a nitrogen dry. The cleaned wafer was soft-baked on a hot plate at a temperature of ~120°C to evaporate any residual solvent.

5.2.2 Fabrication Process

Figure 5.12 presents a schematic illustration of the overall fabrication process of the Ti-SiN$_x$-Ni detector. Fabrication of the detector was completed through a four-mask electron beam (e-beam) lithography process. Due to having nanoscale subwavelength grids (~300 nm), we could not use the conventional optical lithography technique. For e-beam lithography, the resist of choice was polymethyl methacrylate (PMMA), specifically, 950 PMMA C4 (4% diluted in chlorobenzene). We chose PMMA because it patterns easily and holds up well at high substrate temperatures. For each lithography mask, the resist was spin-coated on the Si wafer at a speed of 3000 rpm for 30 s, and

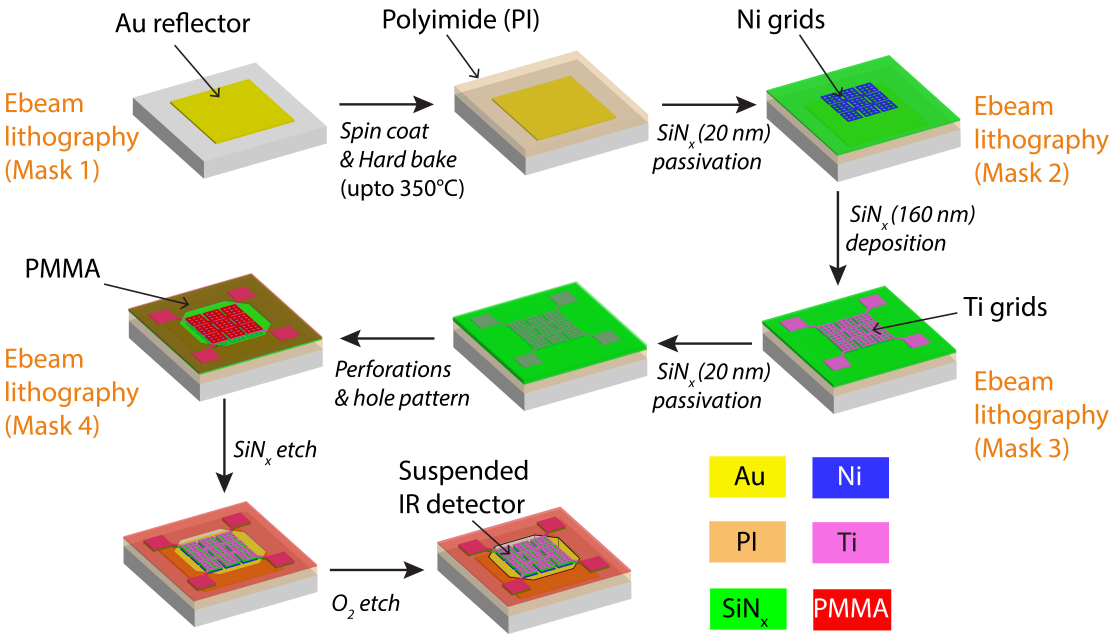

Figure 5.12: Fabrication process flow of the Ti-SiN$_x$-Ni infrared detector.

then baked on a hot plate at a temperature of ∼180°C for ∼8 minutes. This resulted in a resist thickness of ∼500 nm. The wafer was then exposed to high voltage (100 kV) electron beams with a dose of ∼1300 μC/cm^2 to pattern the mask. After each exposure, the wafer was developed in an IPA: MIBK (3:1) solution for ∼30 s.

Step 1: Patterning of the Bottom Au Reflector

In the first step, the bottom reflectors and e-beam markers (∼20 μm) were written on a bare silicon wafer using the 1st mask of e-beam lithography. After developing the PMMA resist, a thin Ni adhesive film (∼15 nm) and a reflector Au film (∼120 nm) were deposited by e-beam evaporation. To ensure uniformity of the metal films, the deposition rates for Ni and Au were maintained at ∼0.1$\mathring{A}$/s and ∼1$\mathring{A}$/s, respectively. During evaporation, the chamber pressure was kept at or below ∼10^{-6} torr (high vacuum). After deposition, the bottom reflector was patterned using a heated lift-off process using MICROPOSIT 1165 remover solution. 1165 remover (from DOW Electronic Materials) is a well-known

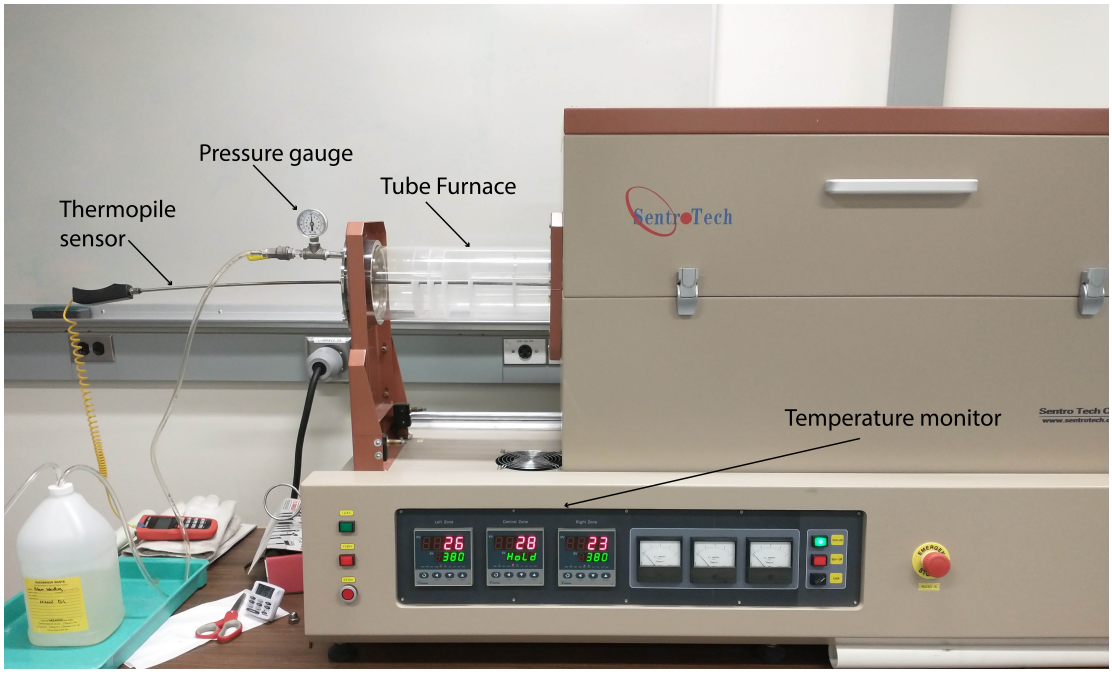

Figure 5.13: Tube furnace system with N_2 gas supply.

resist stripper that requires no intermediate rinse and is fully miscible in water. To expedite the patterning, the 1165 remover was heated to ∼80°C during the lift-off process.

Step 2: Polyimide Deposition and Bake

To form the quarter-wave anti-resonance cavity, a thick polyimide film was deposited on top of the Au reflector as a sacrificial layer. We acknowledge Maryam Jalali-Mousavi, a research assistant professor at Texas A&M Corpus Christi for providing us the specific polyimide (PI 2611, from HD MicroSystems). The polyimide was spin-coated on top of the Au reflector at a speed of 6500 rpm for ∼30 s, resulting in a moderately uniform film. For baking the film, we used a tube furnace with a nitrogen (N_2) gas supply in Prof. Sarah Swisher's research lab, as shown in Fig. 5.13. Polyimide-coated wafers were inserted inside the tube furnace and gradually baked up to ∼350°C with a time span

of ∼2 hours. A temperature monitoring system was used to set up the final baking temperature. Note that the temperature displayed by the monitoring system might not be the same as the wafer temperature. Therefore, a thermopile sensor was placed close to our wafer to measure the actual temperature. For example, when the monitor displayed a temperature of ∼380°C, the temperature near our wafer was found to be ∼350°C from the thermopile. During baking, a pressure gauge was monitored to ensure proper flow of N_2. When baking was completed, the polyimide-coated wafers were left to cool down to room temperature for ∼3/4 hours. The resultant polyimide film was quite uniform with a thickness of ∼2.3 μm, which was resistant to any resist remover (e.g., Acetone or 1165 stripper).

Step 3: Patterning of the Bottom Ni Grids

Initially, 20 nm of SiN_x was initially coated over the hard-baked polyimide using high-density plasma chemical vapor deposition (HDPCVD). The purpose of this thin SiN_x film was to protect the metal grids from erosion and/or contamination. Then, Ni nanoscale grids without supporting tethers were patterned as the bottom metal layer, using the 2^{nd} mask of e-beam lithography. 10 nm of Ni film was deposited using e-beam evaporation, which was followed by stripping of the PMMA resist using 1165 remover. During evaporation, the deposition rate was maintained at ∼0.1$\mathring{A}$/s.

Step 4: Patterning of the Top Ti Grids

160 nm of SiN_x was deposited, using HDPCVD, on top of the Ni grids to form the middle dielectric layer. Then, Ti nanoscale grids with supporting tethers were patterned as the top metal layer, using the 3^{rd} mask of e-beam lithography. Similar to the Ni deposition, e-beam evaporation was used to deposit 10 nm of Ti film, with a deposition rate of ∼0.1$\mathring{A}$/s.

Note that sputtering can be another option for Ni/Ti deposition; however, it would produce conformal coatings, especially in nanoscale patterns. To illustrate this, Fig. 5.14

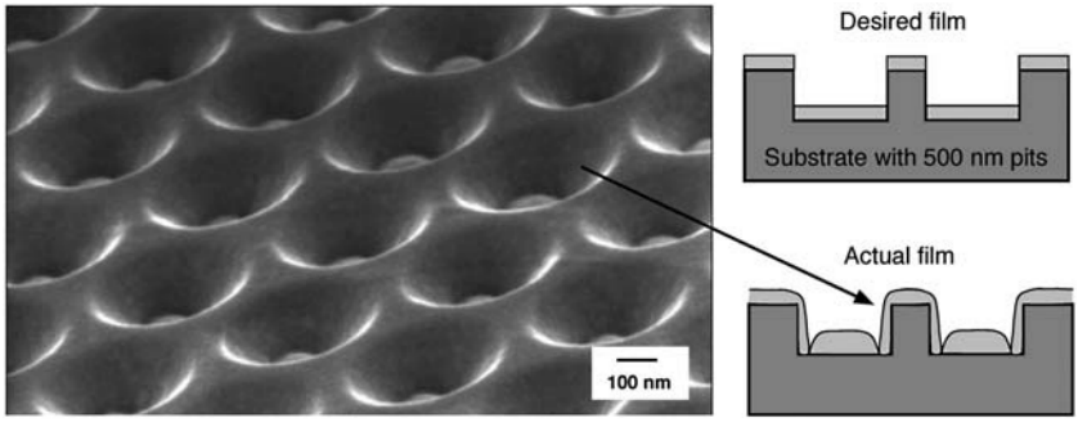

Figure 5.14: Conformal coatings on nanoscale patterns due to sputtering [166].

shows an SEM image of nanoscale patterns coated with a sputtered film, as taken from [166]. Conformal coatings can be clearly visible, which may lead to massive failure during a lift-off process. In addition, note that e-beam evaporation provides better fabrication tolerance, with a thickness of 10±0.3 nm (deviation of ∼3%) for Ni/Ti film deposition.

Step 5: Pattern of Perforations and Air Holes

Ti has a tendency to get oxidized in air, forming TiO_2, which would degrade the optical and physical properties of the thin Ti layer. Therefore, to protect the Ti from oxidation, a thin 20 nm of SiN_x was coated over the nanoscale grids using HDPCVD. Note that SiO_2 can also be used for passivation; however, it may increase the quality factor of the spectral absorption due to its high phonon absorption at ∼9.22 μm. Later, subwavelength perforations and air gaps around the pitches were patterned using the 4^{th} mask of e-beam lithography. Extreme care was taken while aligning the 4^{th} mask on top of the Ti grids, as a slight rotation of the substrate ($>0.2^{\circ}$) could result in misregistration.

Step 6: Etch Releases

The etch release of the structure began with the removal of SiN_x through perforations and holes using reactive ion etching. We used an etch recipe of 10 sccm of CHF_3 and 10 sccm of SF_6, with an RF power of 50 W. The chamber pressure was kept at 5 mTorr to ensure an anisotropic etch. The passivation SiN_x film on top of the Ti grids was not removed as it was protected by the PMMA resist. As a result, Ti-SiN_x bilayer grids were formed. Finally, the perforated structure was successfully suspended by the removal of the sacrificial polyimide using an O_2 isotropic etch. The O_2 recipe used 30 sccm of O_2, with 100 W of RF power and 30−40 mTorr of chamber pressure.

An optical microscopic image of the successfully released Ti-SiN_x-Ni perforated infrared detector is presented in Fig. 5.15.

5.3 Fabrication Challenges

5.3.1 Selection of Sacrificial Layer

Selecting a material for the sacrificial layer was a major challenge. It had to be deposited before the subwavelength nano grid fabrication, had to be chemically resistant to all the etches that followed, and yet had to be easily removed during the release of the detector at the final stage. Table 5.2 summarizes the materials considered and tested, including SiO_2, lift-off resist (LOR) 20B, and polyimide. Among them, polyimide was the most promising material since it could be deposited via spin-coating, could withstand most of the common chemical etchants, and could be removed by at the final fabrication step through O_2 etching.

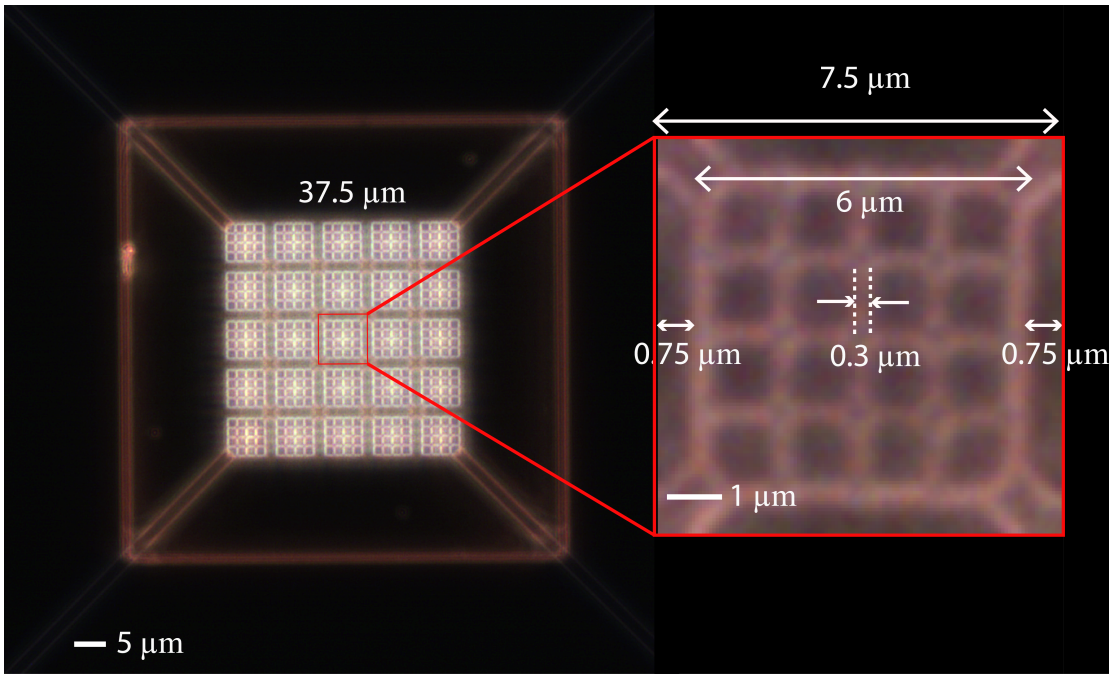

Figure 5.15: Optical microscopic image of the successfully released perforated Ti-SiN$_x$-Ni infrared detector, with an absorption area of 37.5 μm $\times$ 37.5 μm (i.e., 5 $\times$ 5 grating pixel). The inset shows the pitch period, solid pitch length, air space between adjacent pitches, and linewidth of the nano-grids

Table 5.2: Materials tested for the sacrificial layer

Sacrificial material	Deposition technique	Etchant	Result
SiO_2	HDPCVD	BOE	Poor selectivity between SiO_2 and SiN_x during BOE etch
LOR 20B	Spin coat and bake	O_2 plasma etch	Evaporation of LOR due to high temperature (>200°C) bake
Polyimide (PI 2611)	Spin coat and bake	O_2 plasma etch	Successful removal without affecting subwavelength layers

5.3.2 Bake of Sacrificial Layer

High-temperature baking is required for thermal cross-linking within the polyimide layer. Cross-linking forms covalent bonds holding several polymer chains, which provides more rigidity, hardness, and a higher melting point. We found that baking at ∼180°-200°C could not make the polyimide cross-link enough to withstand etchants from subsequent fabrication steps. We eventually baked the polyimide up to ∼350°C for our process. In addition, baking in an air environment can increase the surface roughness of the polyimide due to oxidation. It is not possible to pattern nanoscale grids when the roughness is too high. Therefore, we baked our sample inside a tube furnace with an N_2 gas environment, where N_2 gas flow prevented unnecessary oxidation on the polyimide surface.

5.3.3 Nano-scale grids lift-off

Conformal coatings at the sidewalls of the nano-scale grids can cause critical failure during the lift-off process. Fig. 5.16 shows a microscopic image of failed lift-off process of Ti/Ni grids. It can be observed that the Ti/Ni nano-grids were not patterned well throughout the whole structure, and lifted-off particulates were scattered. This can be attributed to the conformal coatings shown in Fig. 5.14. For proper lift-off, it is necessary to eliminate any sidewall coatings during Ti deposition, which is possible in an e-beam evaporation process.

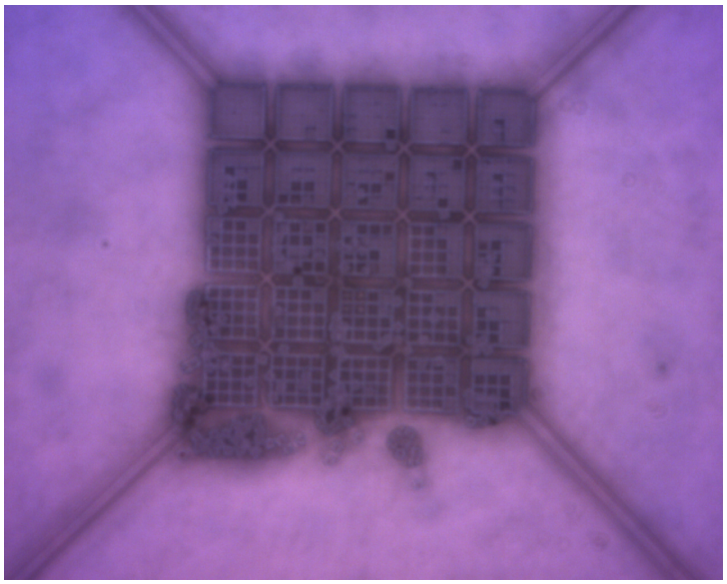

Figure 5.16: Optical microscopic image of the infrared detector after a failed lift-off attempt.

5.4 Detector Characterization

5.4.1 Experimental setup

The fabricated detector was optically read using a Mach-Zehnder interferometer (MZI), a technology chosen because of its ease of integration, as found in fiber optic communications, and its potential to read an entire array simultaneously. Fig. 5.17 presents the schematic illustration of the Mach-Zehnder interferometer (MZI) characterization setup. A He-Ne laser source (λ=632.8 nm) with a power of 10 mW was used for our experiment. The laser beam was divided into two orthogonal linearly polarized beams by a polarizing beam splitter (PBS). One of the beams, mentioned as the "observation" beam, was incident on the pixel gratings of the fabricated detector placed inside a vacuum chamber (pressure $\sim 1.6 \times 10^{-4}$ torr). A micro-scale pinhole ($\sim$50 μm) was used to limit the beam to the detector gratings, and therefore, minimize unnecessary background reflection. Being reflected from the detector, the observation beam was guided towards

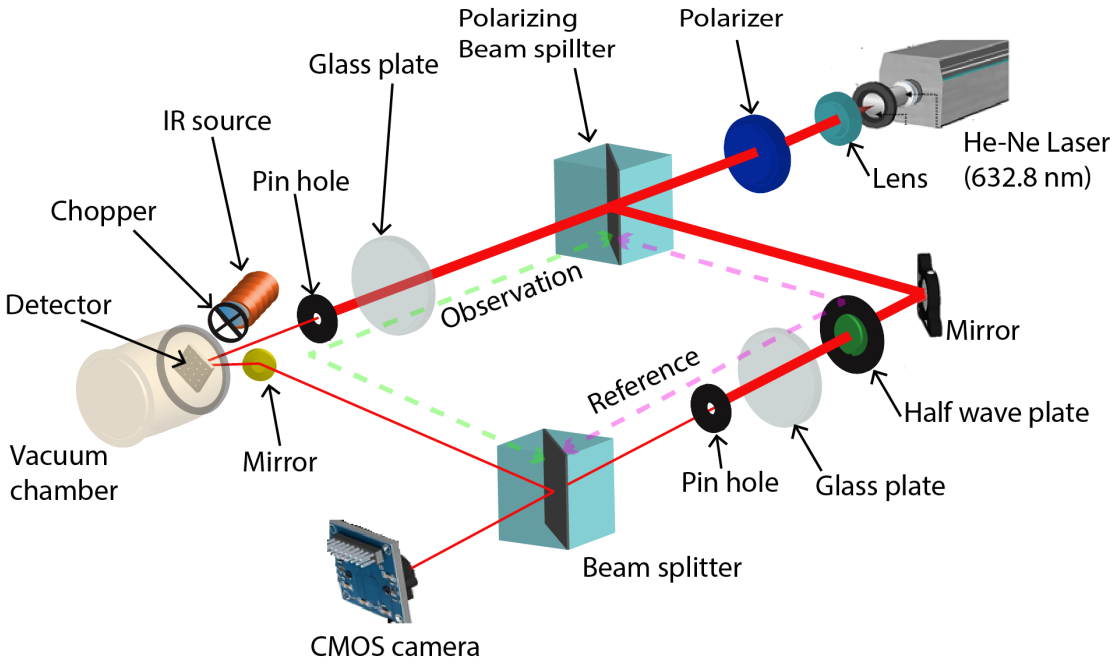

Figure 5.17: Schematic diagram of the Mach-Zehnder interferometer (MZI) with the fabricated detector.

a non-polarizing beam splitter (NPBS) by a small Au mirror. The other orthogonal polarized beam, mentioned as the "reference" beam, got reflected by another Au mirror and traveled to a half-wave plate to become parallel to the polarization state of the observation beam. A similar micro-scale pinhole was used to limit the reference beam. The observation and reference beams interfered with each other at the non-polarizing beam splitter (NPBS), generating interference fringes which were recorded by a CMOS camera. A polarizer was used before the polarizing beam splitter (PBS) to control and equalize the intensity of the reference and observation beams to maximize the contrast of the fringe patterns on the CMOS camera. Glass (SiO_2) plates, with a thickness of $\sim$500 μm, were used along the two beam paths to assess the stability of the interference fringes, meaning whether the fringes shift (i.e., change in optical paths) with a slight rotation (e.g., 0.5°) of any of the plates. To analyze the thermal sensitivity, an IR source (with a chopper) was placed near the vacuum chamber window (i.e., our detector).

It should be noted that at equilibrium, the observation beam travels a slightly larger optical path than the reference beam (in Fig. 5.17), resulting in an optical path difference of ΔL_{OR} in the absence of any IR excitation. To keep the interference fringes visible, the path difference ΔL_{OR} must be smaller than the coherence length L_c of the He-Ne laser beam, which means [167, 168],

$$\Delta L_{\mathrm{OR}} < \frac{c}{\pi \Delta \nu}, \tag{5.3}$$

where, $\Delta\nu$ is the spectral linewidth of the laser (in Hz) and c is the speed of light. With $\Delta\nu$∼0.95 GHz and ΔL_{OR}∼40 mm for our experiment, Eq. 5.3 was satisfied to ensure visible interference fringes.

5.4.2 Optical Input Power

When excited by an IR source, it is important to understand how much IR power gets absorbed by the detector. In our experiment, we used a highly emissive (ε_s=0.95) electrical resistor as the IR source [169], with a circular output aperture area of 19.63 mm^2. We chose a ZnSe window over a SiO_2 window for our vacuum chamber, especially due to the excellent optical transmission of ZnSe in the long-wave infrared (LWIR). To illustrate this, Fig. 5.18 presents the optical transmission of ZnSe [160] and SiO2 [170] between 7 to 12 μm. Due to the phonon absorption peak at ∼9.2 μm, SiO_2 shows very poor transmission in the LWIR region. On the contrary, ZnSe maintains broadband transmission with an average value of ∼71%.

Considering the window transmission, the radiance of the IR source at a temperature T over the LWIR wavelengths (i.e., 8−12 μm) can be computed from Planck's law as [171],

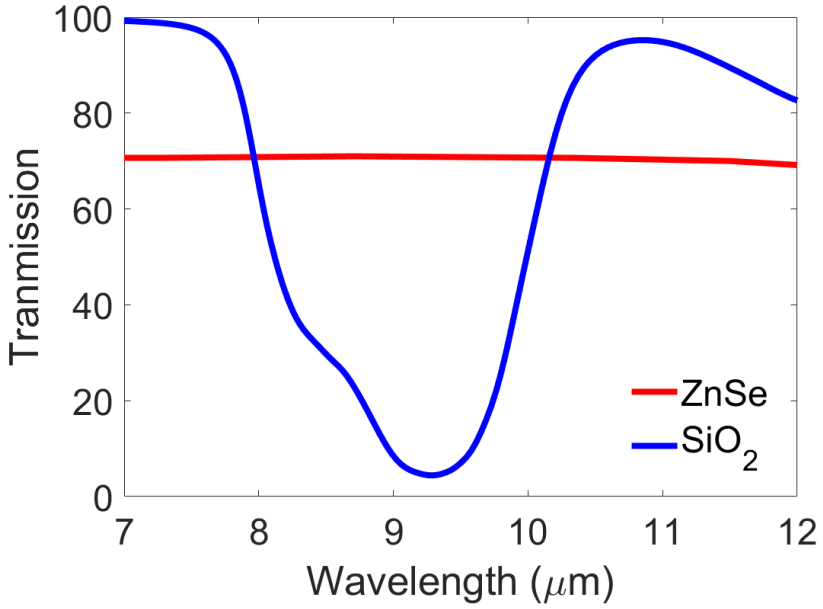

Figure 5.18: Optical transmission of ZnSe [160] and SiO_2 [170] in the long-wave infrared.

$$L_{rad} = \int_{\lambda} \frac{2hc^2 \varepsilon_s T_{\mathrm{w}}(\lambda) d\lambda}{\lambda^5 \left[\exp(hc/\lambda k_{\mathrm{B}} T) - 1\right]}, \tag{5.4}$$

where, h is Planck constant, c is the speed of light, k_{B} is the Boltzmann constant, ε_{s} is the emissivity of IR source, and T_{w} is the spectral transmission of the ZnSe window. The IR radiation subtends onto the detector at a solid angle Ω which can be calculated as [172],

$$\Omega = \int_{\theta_{\mathrm{s}}=0}^{\theta_{\mathrm{s}}} \int_{\phi=0}^{2\pi} \sin\theta d\theta d\phi = 2\pi(1 - \cos\theta_{\mathrm{s}}), \tag{5.5}$$

where, θ_{s} is the semi-cone angle of the radiation, as shown in Fig. 5.19. The angle θ_{s} is

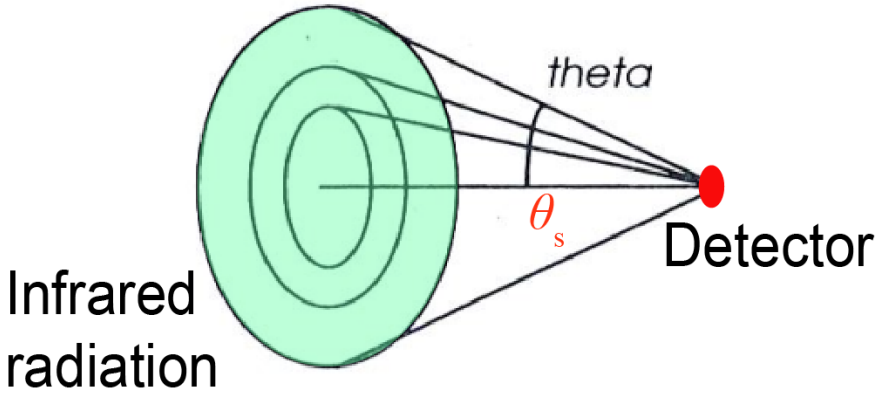

Figure 5.19: Light cone geometry, θ_s semi-cone angle of incident radiation.

related to the F-number F_{no} of the system optics as,

$$F_{no} = \frac{1}{2\sin\theta_s}, \tag{5.6}$$

Considering F_{no}=1, the solid angle Ω of the optical arrangement can be found as $\sim 0.27\pi$.

The corresponding total IR power absorbed by the detector can be calculated as [160],

$$P_{abs} = L_{rad}\Omega A_d \varepsilon_d, \tag{5.7}$$

where, A_d is the absorber area and ε_d is the emissivity of the detector. With A_d=37.5 μm$\times$ 37.5 μm and ε_d $\sim$0.78 (averaged over LWIR measurements), Fig. 5.20 shows the absorbed LWIR power by the detector with small increments of temperature T while operating near room temperature. When the input IR radiation is chopped, the amplitude of the modulated optical power can be given by $2P_{abs}/\pi$ (analyzed by Varpula *et al.* [160]).

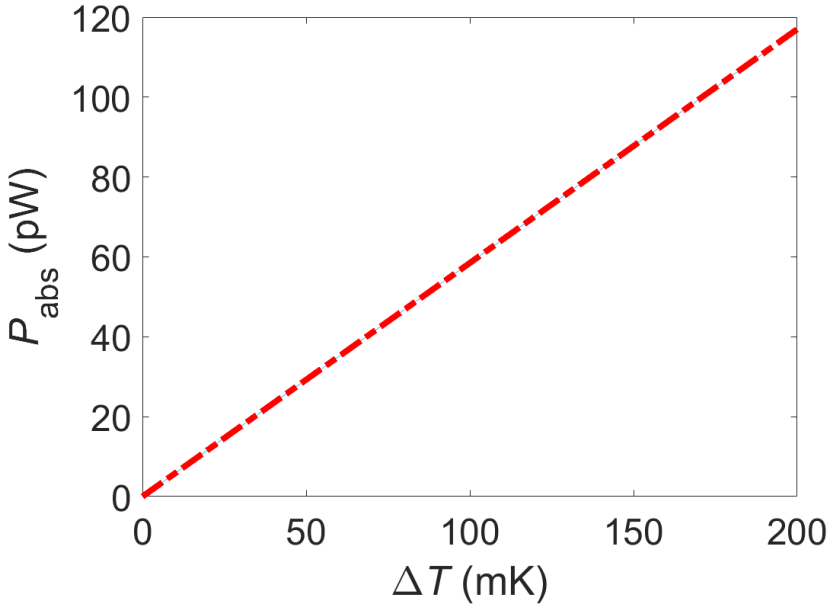

Figure 5.20: Optical IR power absorbed by the detector for different increments of temperature ΔT, while operating near room temperature (T=310 K).

It should be noted that we wanted object or source independence for our thermal detection. Therefore, our calculated solid angle corresponds to a large angular field of view (i.e., $2\theta_s$) of $\sim 0.33\pi$. This means that if the source is positioned far away from the detector, a lens should be placed to maintain the solid angle.

5.4.3 Measurement of Thermal Response

When the thermal detector is excited by an IR source, the input optical power is absorbed and heats up the detector. Due to the thermal expansion mismatch between the Ti and Ni films, the heat-up results in slight deformations δ_v in the shape of the perforated membrane, leading to additional path differences between the observation and reference beams beyond equilibrium, and therefore, distinct phase shifts in the interference fringes. The details of membrane deformation will be explained in the following section. As an example, Fig. 5.21 shows a phase shift of $\sim 2.2\pi$ of the fringes due to

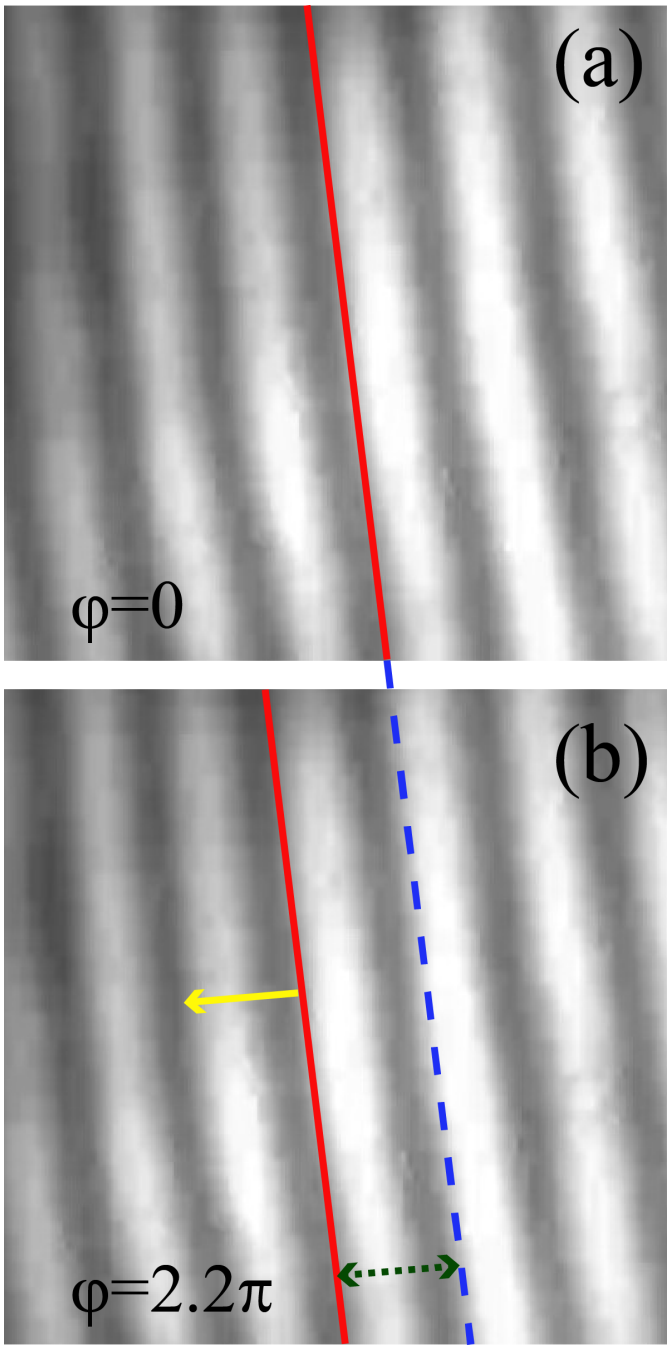

Figure 5.21: Fringe images recorded on a CMOS camera. A solid red and a dashed blue line are used to highlight the distinct phase shift of the fringes. The fringe movement is indicated by a yellow arrow. The fringe shift corresponds to a temperature change ΔT of 101 mK, as measured by a commercial microbolometer camera.

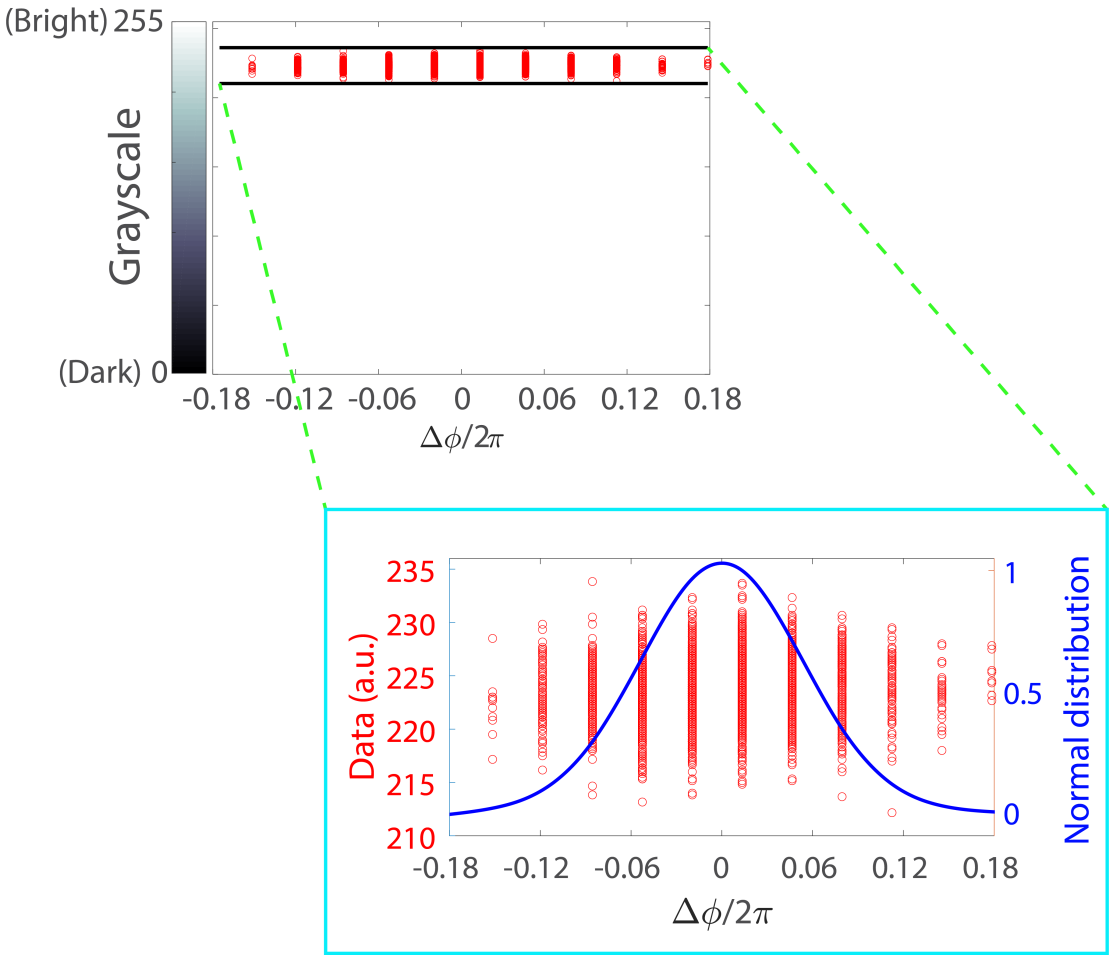

Figure 5.22: Fluctuations of an interference fringe (i.e., a sine peak position) without external IR absorption presented in terms of normalized phase shifts $\Delta\phi/2\pi$, where mean equilibrium is presented as 0. The inset shows a zoomed version of the grayscale data points with a normal fitting distribution, which is used to determine our noise. The standard deviation σ of this distribution (i.e., $\Delta\phi/2\pi\sim0.05$) is compared to the fringe shift created by a known source temperature. Using this method, we found a minimum NETD of $\sim$4.5 mK for our detector.

a chopped (f_c=10 Hz) IR excitation, as recorded by our CMOS camera at room temperature (∼310 K). The frame rate of the camera was 30 Hz during this measurement, which could be varied further with chopper frequencies to maintain the Nyquist condition [173]. This means the camera frame rate has to be twice or greater than the chopping frequency of the IR signal. The heating in this example image corresponds to a source temperature change ΔT of ∼101 mK stabilized over a 1 second duration, as calibrated by a commercial microbolometer camera (Jenoptik IR-TCM 384). The fringe images were further processed with bright and dark colors, converted into a 0-255 data scale, and fitted with sinusoidal curves to measure the amount of phase shift. Details of the fringe analysis and source calibration have been discussed in Appendix D. For an NETD (thermal sensitivity) analysis, fringe fluctuations without IR excitation (i.e., a sine peak position) were recorded for a duration of ∼126 s and analyzed for 3800 frames. The IR source could be turned off or shuttered during this measurement. Fig. 5.22 presents the grayscale data points of the fringe fluctuation (i.e., sine peak) with normalized phase shifts $\Delta\phi/2\pi$, where the mean equilibrium is shown as 0. The inset presents a zoomed version of the data with a normal distribution, which is used to determine our noise. We found that the standard deviation of this distribution is ∼5% of the fringe period (i.e., $\Delta\phi/2\pi\sim0.05$), which corresponds to a temperature difference (NETD) of ∼4.5 mK when compared to the average fringe shift of 2.24π (i.e., $\Delta\phi/2\pi\sim1.12$) created by source excited temperature change ΔT of 101 mK. Note that similar to Fig. 5.21, three sets of measurements were analyzed to calculate the source-excited average shift. The measured NETD is around an order of magnitude lower than most uncooled commercial cameras (∼50 mK) [174] and ∼63% lower than recently reported uncooled infrared detectors [175, 176].

Table 5.3: Material properties used in the thermal detector

Material	**Specific Heat ($Jkg^{-1}K^{-1}$)**	**Thermal conductivity ($Wm^{-1}K^{-1}$)**	**Density (kgm^{-3})**	**Thermal expansion coefficient (K^{-1})**	**Young's modulus (GPa)**
Ti	544.2 [177]	6.7 [178]	4506 [179]	8.5 [180]	104.1 [181]
SiNx	1492.3 [182]	2.1 [183]	3100 [184]	3.3 [185]	300 [186]
Ni	502.4 [177]	60 [187]	8900 [188]	16.3 [189]	205 [190]

5.4.4 Result and Discussion

Calculation of Thermal Parameters

Table. 5.3 shows the material properties of Ti, SiN_x, and Ni, which will be used in our calculation. To analyze the heat transfer in thermodynamics, the thermal capacitance of the infrared detector can be defined as [175, 191],

$$C = C_{\mathrm{Ti}}\rho_{\mathrm{Ti}}V_{\mathrm{Ti}} + C_{\mathrm{SN}}\rho_{\mathrm{SN}}V_{\mathrm{SN}} + C_{\mathrm{Ni}}\rho_{\mathrm{Ni}}V_{\mathrm{Ni}}, \tag{5.8}$$

where, C, ρ, and V correspond to the specific heat, density, and volume of the material of interest, respectively. Considering the solid pitch area and material thicknesses taken from Table. 5.1, the thermal capacitance of the grating pitches C_{P} (i.e., 5×5 array) is $\sim 3.2\times10^{-10}$ JK^{-1}. Moreover, the contribution of the support cross-legs that connect the small absorber pitches together (length l_{c} of 3 μm and width b_{c} of 1 μm) correspond to a thermal capacitance C_{S} of $\sim 8\times10^{-11}$ JK^{-1}. Therefore, the total thermal capacitance $C_{\mathrm{T}} = C_{\mathrm{P}} + C_{\mathrm{S}}$ of the detector is found as $\sim 4\times10^{-10}$ JK^{-1}.

The total thermal conductance G_{T} of the detector can be expressed with the following equation [192, 193],

$$G_{\mathrm{T}} = G_{\mathrm{leg}} + G_{\mathrm{rad}} + G_{\mathrm{air}}, \tag{5.9}$$

where, G_{leg}, G_{rad}, and G_{air} are the heat conduction through the four tether legs (length l and width b), the heat radiation of the detector absorber, and the heat conduction through air, respectively. Fron Deng *et al.* [191], we can calculate the thermal conductance of the support tether legs G_{leg} as,

$$G_{\mathrm{leg}} = 4 \times \left(\eta_{\mathrm{Ti}} \frac{b \times t_{\mathrm{Ti}}}{l} + \eta_{\mathrm{SN}} \frac{b \times t_{\mathrm{SN}}}{l} \right), \tag{5.10}$$

where, η_{Ti} and η_{SN} are thermal conductivities of Ti and SiN_x, respectively. Note that Ni was not deposited in the long tether legs. With l=100 μm and b=2 μm, G_{leg} would be found as $\sim 3.8 \times 10^{-8}$ WK^{-1}. In addition, the radiation-limited thermal conductance G_{rad} can be given by the derivative of the radiation power with temperature as [171],

$$G_{\mathrm{rad}} = \frac{2h^2 c^3 A_{\mathrm{d}}}{k_{\mathrm{B}} T^2} \int\limits_{\lambda,\Omega} \frac{\varepsilon_{\mathrm{d}}(\lambda) \exp(hc/\lambda k_{\mathrm{B}} T) d\lambda d\Omega}{\lambda^6 [\exp(hc/\lambda k_{\mathrm{B}} T) - 1]^2}, \tag{5.11}$$

With spherical radiation around the detector over the LWIR wavelengths (i.e., 8−12 μm), G_{rad} would be calculated as $\sim 1.5 \times 10^{-8}$ WK^{-1}. For the heat transfer through airflow, the thermal conductance G_{air} depends on the chamber pressure P_{ch} as [192],

$$G_{\mathrm{air}} = \left(\frac{1}{\kappa_{\mathrm{hp}}} \frac{t_{\mathrm{air}}}{A_{\mathrm{d}}} + \frac{1}{\gamma_{\mathrm{lp}}} \frac{1}{P_{\mathrm{ch}}} \frac{1}{A_{\mathrm{d}}} \right)^{-1}, \tag{5.12}$$

where, κ_{hp} is the thermal conductivity coefficient of air in the classical theory, which has been reported as 0.0263 WK^{-1} [192], and γ_{lp} is a correction factor when the air molecules are confined in between the detector and bottom Au reflector and the mean-free path is much larger than the air gap t_{air} of 2.3 μm. With a specific heat for air (C_{air}=1005 $\mathrm{Jkg}^{-1}\mathrm{K}^{-1}$) and mass of a single molecule (m_{air}=4.65×10^{-26} kg), $\gamma_{\mathrm{lp}} = \frac{C_{\mathrm{air}}}{3} \sqrt{\frac{8 m_{\mathrm{air}}}{\pi k_{\mathrm{B}} T}}$ at room temperature can be calculated as ~ 1.8 $\mathrm{ms}^{-1}\mathrm{K}^{-1}$. Note that Eq 5.12 indicates an increase in G_{air} when the chamber pressure P_{ch} rises. During the experiment, we

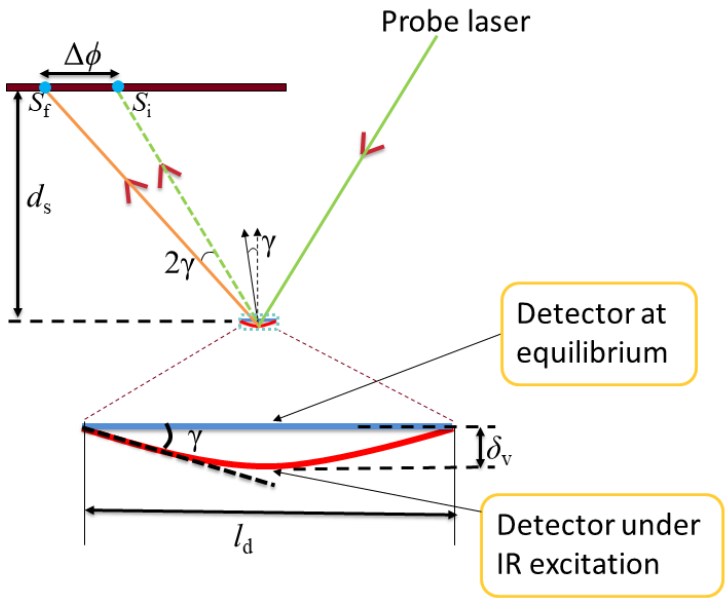

Figure 5.23: Schematic illustration of the detector deflection and resultant phase shift $\Delta\phi$.

achieved a moderately high vacuum (i.e., P_{ch} ~1.6×10^{-4} torr) using a turbomolecular pump. Therefore, using Eq 5.12, G_{air} for our system should be ~5.5×10^{-11} WK^{-1}, which is quite negligible compared to G_{leg} and G_{rad}. With all three parts, the total thermal conductance G_T of our detector would be ~5.3×10^{-8} WK^{-1}.

The thermal response time constant (τ) is one of the most important parameters of the infrared detector. More information can be captured by a quicker response speed, i.e., a smaller time constant. The typical values of (τ) in an infrared detector may vary from 0.5 ms to ~1 s [175]. From C_T and G_T, we can calculate our thermal time constant as $\tau = C_T/G_T$, which would give a value of ~7.5 ms. This is within the range of video frame rate detection.

Analysis of Responsivity

To analyze thermal sensitivity, it is important to understand how a slight deformation in the detector membrane can cause a distinct phase shift in the interference fringes. In this regard, Fig 5.23 presents a schematic illustration of the detector deflection and corresponding change in the probe (He-Ne) beam reflection. When excited by an IR source, the detector membrane starts to deform, mainly due to the large thermal expansion mismatch between the two outer layers (i.e., Ti and Ni), which can be seen from Table 5.3. A linear deflection δ_{v} or angular deflection γ can cause the probe beam to travel an additional optical path, resulting in a shift in the reflection position of the beam from S_{i} to S_{f} at the receiving end. This shift causes a phase change of $\Delta\phi$ of the interference fringes in the CMOS camera. The phase shift $\Delta\phi$ can be related to the angular deflection γ by the following expression [194, 195],

$$\Delta\phi = 2\pi \frac{d_{\mathrm{s}}}{p_{\mathrm{f}}} \tan(2\gamma), \tag{5.13}$$

where d_{s} is the collection distance of the probe beam and p_{f} is the fringe period. The angular deflection γ can be extracted from experimental observations of $\Delta\phi$, d_{s}, and p_{f}, which give the linear deflection δ_{v} as, $\delta_{\mathrm{v}} = (l_{\mathrm{d}}/2)\tan(\gamma)$.

Typically, thermal detectors with electrical readouts, such as microbolometers or thermopile detectors, report the thermal responsivity in terms of output voltage per unit of optical power (V/W). However, in detectors with optical readouts, the responsivity can be described as the deflection per unit power, either linear (m/W) or angular (deg/W) [184]. With experimental observations of fringe shifts and corresponding detector deflections, we analyzed the linear responsivity $\Re_{\mathrm{v}}$ and angular responsivity $\Re_{\gamma}$ with different modulation frequencies when the source excitation temperature increment ΔT was ∼101 mK. Fig 5.24 shows the responsivities $\Re_{\mathrm{v}}$ and $\Re_{\gamma}$ as functions of the modulation frequencies. Details of the experimental point analysis (from measured $\Delta\phi$) are presented in Appendix D. Note that d_{s}=200 mm and p_{f}=1.6 mm from our

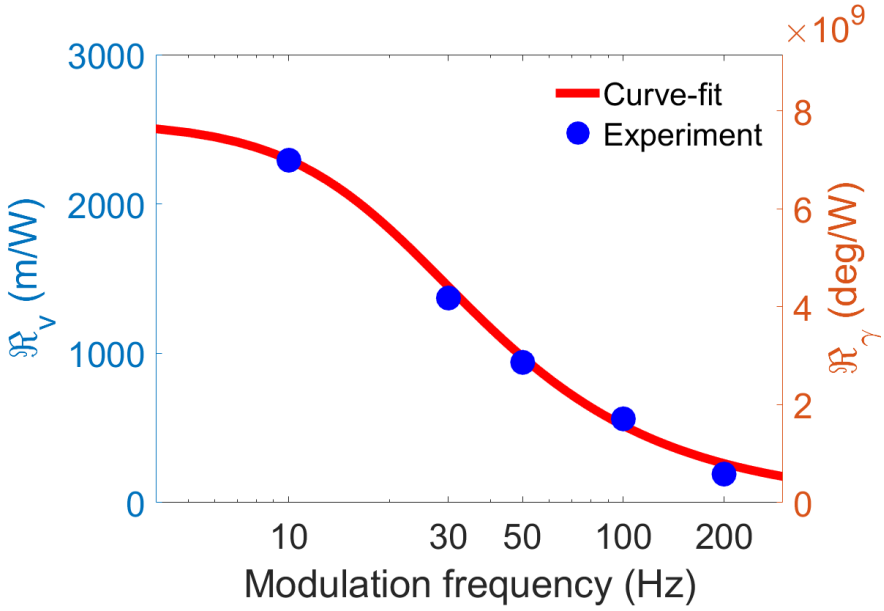

Figure 5.24: Linear and angular responsivities of the detector with different modulation frequencies.

experimental observations. From Fig 5.24, the time constant τ of the detector can be found ~7.4 ms (from the -3 dB cutoff), which is almost the same as observed in our theoretical calculations.

Analysis of Detectivity

The detectivity is often used to describe the performance of an infrared detector and is related to the noise-equivalent power (NEP) by [175, 171],

$$D^* = \frac{\sqrt{A_\mathrm{d}\Delta f}}{NEP}, \tag{5.14}$$

where, Δf is the measurement bandwidth. Unlike typical thermoelectric devices and resistive bolometers, our detector is free from electrical noise (i.e., Johnson or flicker $1/f$). The only noise that limits the performance is the phonon-dominant temperature

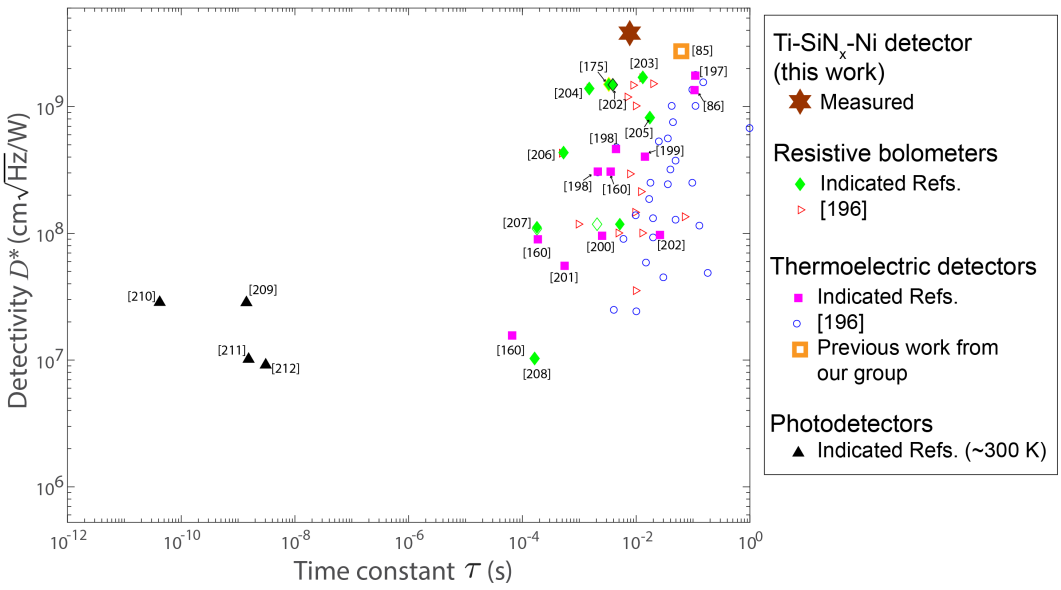

Figure 5.25: Comparative analysis of detectivity D^* and thermal time constant τ of the Ti-SiN$_x$-Ni infrared detector presented in this work with the state-of-the-art resistive micro-bolometers, thermoelectric detectors, and photodetectors. Only uncooled (i.e., room temperature) detectors are considered in this plot.

fluctuations. The details of the noise calculations will be discussed in the following section. The NEP of the detector can be calculated from the measurement of NETD as [172],

$$NETD = \frac{4F_{\mathrm{no}}^2}{A_{\mathrm{d}}\varepsilon_{\mathrm{d}}\pi\left(\Delta L/\Delta T\right)}NEP, \tag{5.15}$$

where F_{no} is the F-number of the system optics and $\Delta L/\Delta T$ is the change in the radiance with temperature. With our measured NETD from Fig.5.22 and other parameters calculated for λ $\sim$8$-$12 μm; i.e., A_{d}=37.5 μm $\times$ 37.5 μm and ε_{d}=0.78 (averaged from measurements), a detectivity D^* of $\sim$3.8$\times$10^9 cm$\sqrt{Hz}$/W was found from the experiment. Note that from theoretical calculations, the temperature fluctuation noise would result in a NEP of 3.05 pW (details in the following section) and hence, a D^* of 3.9$\times$10^9 cm$\sqrt{Hz}$/W, which is pretty close to our measurement. This may be the highest D^* for any fabricated room temperature infrared thermal detector reported to date. To better understand this, Fig 5.25 presents a comprehensive analysis of the uncooled infrared detector technology in terms of detectivity and thermal time constant. In this analysis, we have included all types of detectors, i.e., thermoelectric detectors [85, 86, 160, 196, 197, 198, 199, 200, 201, 202], resistive microbolometers [175, 196, 203, 204, 205, 206, 207, 208], and quantum (uncooled) detectors [209, 210, 211, 212]. It can be clearly observed that our fabricated detector shows the highest detectivity over nearly 70 reported works, with a time constant ($\sim$7.4 ms) relatively faster than the video frame rates.

It should be noted that our optical characterization technique i.e., Mach Zehnder interferometry has been fully integrated into a microelectromechanical system (MEMS) structure [213, 214], with promising possibilities in a number of applications, such as fiber optics communication [215, 216, 217] and optical sensing [218, 219, 220]. Mach

Zehnder interferometry requires very low power consumption and is extremely compatible with ultrasensitive sensing due to its ease of integration. Therefore, an array of pixels can be optically sensed (multiple element sensing) by mapping the phase images using a Mach Zehnder MEMS structure.

5.4.5 Noise Calculation

Being free from electrical noise, e.g., Johnson and $1/f$ (flicker) noise, our thermal detector is still vulnerable to other noise sources, such as temperature fluctuations (i.e., thermo-dynamic noise), mechanical fluctuations (i.e., thermo-mechanical noise), laser pressure induced deflections (i.e., photon pressure noise) and diffraction effects on interference fringes (i.e., diffraction induced noise). This section describes the details of these noise calculations for our detector.

Temperature Fluctuations

One of the important noise sources of our optomechanical detector is temperature fluctuation noise. When quanta of energy enter or leave the detector, they change the device temperature. These fluctuations cause uncertainty in the temperature of the detector. Being independent of the source, these temperature fluctuations depend on the thermal mass of the detector. Quantitatively, the magnitude of the temperature fluctuations can be calculated as [221, 222, 196],

$$\sqrt{\langle \Delta T^2 \rangle} = \sqrt{\frac{k_{\mathrm{B}} T^2}{C_{\mathrm{T}}}}, \tag{5.16}$$

where, k_{B} is the Boltzmann constant, T is the temperature, and C_{T} is the overall heat capacity of the detector. From Eq.5.16, it is quite evident that a smaller heat capacity, i.e., thermal mass will increase the uncertainty in temperature. With $C_{\mathrm{T}} \sim 4.02 \times 10^{-10}$ JK^{-1} (from earlier calculations), the uncertainly can be found as $\sim$0.06 mK. Note that this uncertainty in temperature corresponds to the detector itself, not the actual object

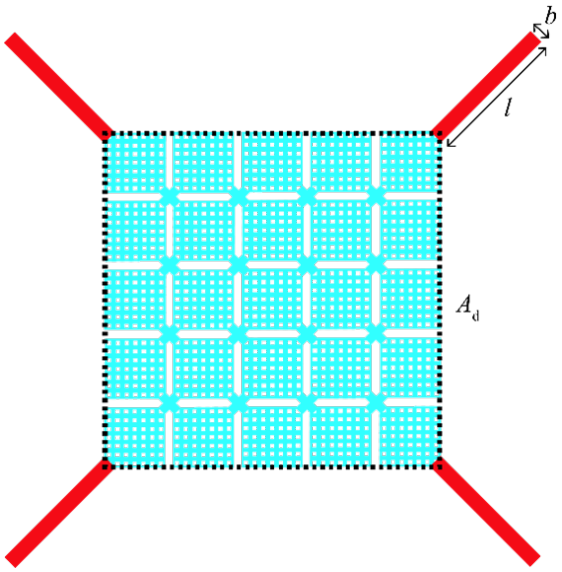

Figure 5.26: 2D Schematic of the infrared detector suspended by straight tethers. The length l and width b of the individual tethers are highlighted, along with the total absorber area A_d.

or background.

Although the magnitude of the temperature fluctuations depends only on the thermal mass of the detector, the amount of infrared signal power required to exceed these fluctuations depends on both thermal mass and heat conduction. The power variance or NEP due to temperature fluctuations can be expressed as [171],

$$\sqrt{\Delta P^2} = G_T \sqrt{\frac{k_B T^2}{C_T}}, \tag{5.17}$$

where G_T is the thermal conductance and C_T is the heat capacitance of the detector. With C_T=4.02×10^{-10} JK^{-1} and G_T=5.3×10^{-8} WK^{-1}, the NEP due to thermal fluctuations can be found to be 3.05 pW.

Mechanical Fluctuations

At room temperature, the mechanical fluctuation of a suspended membrane is primarily dependent on the spring constant of its supporting tethers, as shown in Fig.5.26. The spring constant of an ideally fixed tether or guide-end cantilever can be expressed as [223],

$$k_s^0 = \frac{E_{\text{eff}} b t_{leg}^3}{l^3}, \tag{5.18}$$

where, E_{eff} is the effective Young's modulus, l is the length, b is the width and t_{leg} is the total thickness of the tether leg (i.e., $t_{\text{leg}} = t_{\text{Ti}} + t_{\text{SN}}$). Note that during fabrication the tethers were made from Ti and SiN_x films, and the Ni film was only deposited as a part of the infrared absorber. Therefore, the effective Young's modulus can be calculated from contributions of both the Ti and SiN_x thicknesses (i.e., t_{Ti} and t_{SN}) as [224],

$$E_{\text{eff}} = \frac{E_{\text{Ti}}^2 \left(\frac{t_{\text{Ti}}}{t_{\text{leg}}}\right)^4 + E_{\text{SN}}^2 \left(\frac{t_{\text{SN}}}{t_{\text{leg}}}\right)^4 + 2E_{\text{Ti}}E_{\text{SN}} \left(\frac{t_{\text{Ti}}}{t_{\text{leg}}}\right)\left(\frac{t_{\text{SN}}}{t_{\text{leg}}}\right) K}{E_{\text{Ti}} \left(\frac{t_{\text{Ti}}}{t_{\text{leg}}}\right) + E_{\text{SN}} \left(\frac{t_{\text{SN}}}{t_{\text{leg}}}\right)}, \tag{5.19}$$

where, $K = 2\left(\frac{t_{\text{Ti}}}{t_{\text{leg}}}\right)^2 + 2\left(\frac{t_{\text{SN}}}{t_{\text{leg}}}\right)^2 + 3\left(\frac{t_{\text{Ti}}}{t_{\text{leg}}}\right)\left(\frac{t_{\text{SN}}}{t_{\text{leg}}}\right)$. Here, E_{Ti} and E_{SN} are the Young's modulus of Ti and SiN_x, respectively. Considering t_{Ti}=10 nm and t_{SN}=200 nm from our detector design, and material properties presented in Table5.3, the effective modulus E_{eff} can be found to be 273.8 GPa.

Typically, the spring constant of a suspended membrane is calculated by summing the individual tether spring constants, i.e., k_s^0, assuming that the movable membrane is completely rigid without any local deformation in the joints with the tethers [223]. However, in reality, the membrane itself can also deform and hence, affect the total spring constant. In addition, the deflection also depends on the overall solid area and the gap between the membrane and the ground. Considering a parametric study with different parameters, the overall spring constant of the perforated structure can be

calculated as [225],

$$K_{\text{total}} = \frac{4k_s^0}{\left(1 + 0.15\frac{b}{l^3}A_{\text{d}}FF\right)}, \tag{5.20}$$

where, A_{d} is the total absorber area and FF is the fill factor. With our designed parameters, i.e., A_{d}= 37.5 μm × 37.5 μm, l=100 μm, b=2 μm, and FF=0.28 (considering FF of the 37.5 μm×37.5 μm detector absorber), the overall spring constant K_{total} can be found to be ∼0.02 Nm^{-1}. Then the mechanical fluctuation for our structure can be approximated as $\sqrt{\langle x^2 \rangle} = \sqrt{k_{\text{B}}T/K_{\text{total}}}$, which is ∼4.6×10^{-10} m or ∼0.46 nm. The above equation assumes a low mechanical quality factor for the device, which is appropriate given the very large area-to-thickness ratio. The calculated noise would induce a phase change of only ∼0.08% to the He-Ne laser measurement. Compared to our measurements, this mechanical fluctuation would correspond to a phase shift of ∼0.01π, which would give a NEP of ∼0.38 pW.

Note that the resonant frequency of the mechanical fluctuation is much higher than the video frame rate. Using $f_{\text{res}} = \frac{1}{2\pi}\sqrt{\frac{E_{\text{eff}}}{\rho_{\text{eff}}}}\frac{t_{leg}}{l^2}$, where $\rho_{\text{eff}} = \rho_{\text{Ti}}\frac{t_{\text{Ti}}}{t_{leg}} + \rho_{\text{SN}}\frac{t_{\text{SN}}}{t_{leg}}$ is the effective density, the resonant frequency of the tethers are found to be ∼30 kHz.

Laser Pressure-induced Deflections

The He-Ne laser used as a probe beam in our experiment can exert a small force on the surface of the suspended membrane, resulting in a small deformation. Maxwell described this force as the photon pressure-induced force [226]. When the probe laser impinges on the surface of the detector membrane, the plate would deflect until a balance is reached between the applied photon pressure and the restoring force of the membrane. The resultant deflection due to this laser pressure can be termed photon pressure noise. The magnitude of this deflection would mostly be observed on the support tethers of the detector membrane, as shown in Fig. 5.27. This can be attributed to the fact that the tethers are long cantilever beams with a high aspect ratio (50:1) and the laser-induced

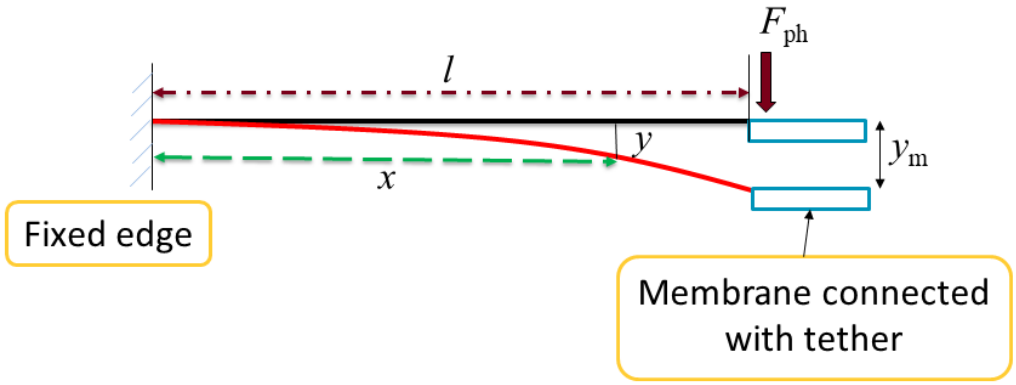

Figure 5.27: Schematic illustration of deflection of the support tether due to laser (He-Ne) induced pressure force.

pressure force (i.e., photon pressure force on the detector plate) acts as a load on their edge. The mechanism of this deflection can be better understood through the following differential equation as [227],

$$E_{\text{eff}} I \frac{d^2y}{dx^2} = -F_{\text{ph}}(l - x), \tag{5.21}$$

where, F_{ph} is the photon pressure force, E_{eff} is effective elastic modulus, and I is the moment of inertia (i.e., $I = bt_{\text{leg}}^3 \big/ 12$) of the tether. By solving the differential equation with proper boundary conditions (i.e., $x = 0, y = 0$ and $x = 0, \frac{dy}{dx} = 0$), the deflection y can be expressed as,

$$y = -\frac{F_{\text{ph}} l x^2}{2E_{\text{eff}} I} + \frac{F_{\text{ph}} x^3}{6E_{\text{eff}} I}, \tag{5.22}$$

At x=l, the maximum deflection y_{m} can be found as $F_{\text{ph}} l^3 / 3E_{\text{eff}} I$. With 10 mW of He-Ne laser beam incident on the detector absorber supported by the four tethers, each tether would experience a photon pressure force F_{ph} of ~0.01 pN. Therefore, considering E_{eff}=273.8 GPa, l=100 μm, b=2 μm, and t_{leg}=210 nm, the photon pressure would

exert a maximum deflection of $\sim 8\times10^{-12}$ m or $\sim$8 pm for our detector. Note that this deflection would induce a phase change of only $\sim$0.001% to the He-Ne laser measurement. Compared to our measurements, this deflection would show a phase shift of only $\sim 2\times10^{-4}\pi$, which would correspond to a NEP of $\sim$0.007 pW.

CMOS readout noise

From experimental measurements, the minimum phase shift due to ΔT from the target IR source was observed as $\sim 0.04\pi$, which can be attributed to the resolution limit of our CMOS camera. This phase shift would correspond to a linear deflection δ_c of $\sim$1.5 nm. The noise in the CMOS readout might originate from a couple of sources. Shot noise in the CMOS camera can contribute to the readout noise equal to $\Delta I/I = 1/\sqrt{N_{\mathrm{e}}}$, where N_{e} is the full-well capacity of the CMOS pixels. With a standard Ne of 1×10^4 electrons for CMOS camera, the shot noise of the CMOS can result in a NETD defined as [228],

$$\Delta T_{\mathrm{shot}} = (\Delta I/I)\,\frac{\delta_{\mathrm{c}}}{S_{\mathrm{T}}}, \tag{5.23}$$

which is $\sim$17.2 μK. Note that the thermomechanical sensitivity of the detector can be defined as $S_{\mathrm{T}} = \delta_{\mathrm{v}}/\Delta T$, where ΔT is the increase in temperature. From our measurements, ΔT of 101 mK corresponds to a linear deflection of 88 nm, which gives an S_{T} of 871.29 nm/K. In addition, digitization of the CMOS camera adds noise to the readout fringes. For an 8-bit digitizer, this error corresponds to a NETD calculated as,

$$\Delta T_{\mathrm{dig}} = \left(\frac{1}{2^8}\right)\frac{\delta_{\mathrm{c}}}{S_{\mathrm{T}}}, \tag{5.24}$$

Which is $\sim$6.7 μK. Note that the dark current in the CMOS is quite small and can be neglected for optical readout [228]. Therefore, the total equivalent temperature noise

due to CMOS readout can be calculated as,

$$NETD_{\text{readout}} = \sqrt{\Delta T_{\text{shot}}^2 + \Delta T_{\text{dig}}^2}, \tag{5.25}$$

which is found to be ∼18.4 μK. This NETD would correspond to a NEP value of ∼0.013 pW.

Diffraction on Interference Fringes

In the Mach Zehnder interferometer, the He-Ne probe beam was shrunk to focus it on the thermal detector. Reducing the beam size can cause diffraction effects on the interference fringes, which can limit the minimum measurable phase shift due to thermal excitation. To illustrate this, let us assume the reference and observation beams as the fundamental Gaussian mode, which is [229, 230],

$$u = A \exp\left[-jkz - jk\frac{r^2}{2R(z)} + j\tan^{-1}\left(\frac{\theta_{\text{diff}} \times z}{\omega_0}\right)\right], \tag{5.26}$$

where, A is the amplitude, r is the beam radius along x-y plane, and $k = \frac{2\pi}{\lambda}$ is the propagation wavevector along z direction. Three distinct phase terms can be observed; propagation phase kz, spherical phase $k\frac{r^2}{2R(z)}$, and Gouy phase $\tan^{-1}\left(\frac{\theta_{\text{diff}} \times z}{\omega_0}\right)$. Here, $R(z) = z\left[1 + \left(\frac{\omega_0}{\theta_{\text{diff}} \times z}\right)^2\right]$ is defined as the radius of curvature along the beam propagation, where ω_0 is the beam waist and $\theta_{\text{diff}} = \frac{\lambda}{\pi\omega_0}$ is the angle of beam diffraction. The propagation phase relates to the optical beam paths, whereas the spherical and Gouy phases correspond to the diffraction of the beams. Therefore, the phase difference induced by the beam diffraction in the interference output can be expressed as [231, 229],

$$\Delta\phi_{\text{diff}} = k\frac{r^2}{2}\left(\frac{1}{R_{\text{ref}}} - \frac{1}{R_{\text{det}}}\right) + \left[\tan^{-1}\left(\frac{\theta_{\text{diff}} \times z_{\text{det}}}{\omega_0}\right) - \tan^{-1}\left(\frac{\theta_{\text{diff}} \times z_{\text{ref}}}{\omega_0}\right)\right], \tag{5.27}$$

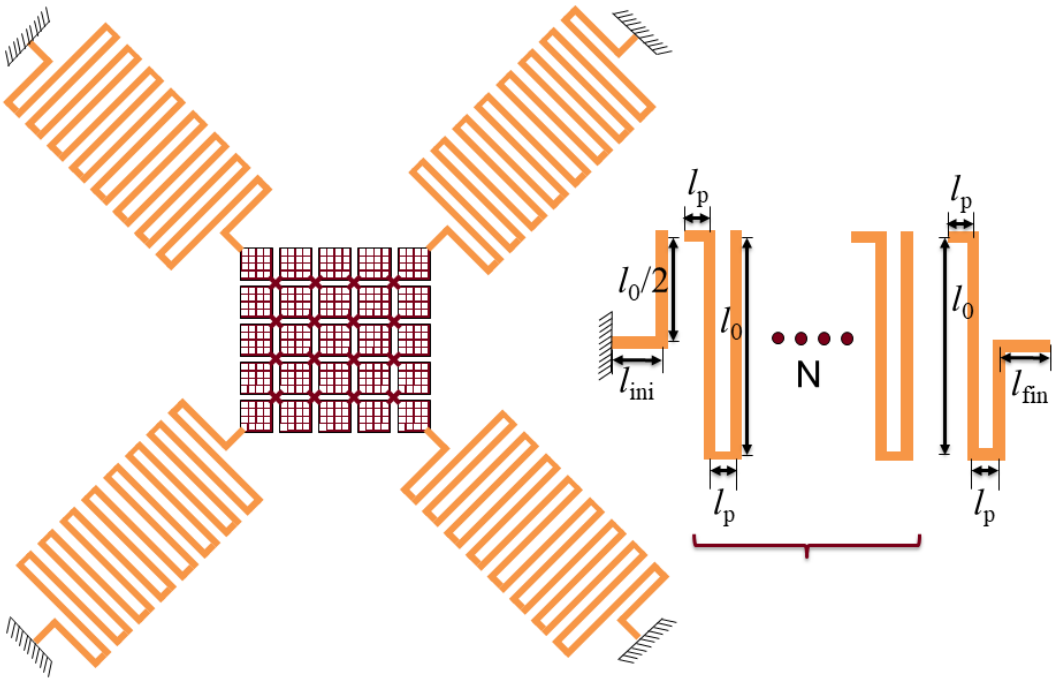

Figure 5.28: Schematic illustration of the perforated thermal detector with four serpentine support tethers. The dimension of a tether has been shown in the inset.

In the interferometer setup, 50 μm pinholes were used to reduce the beam size on both reference and detection (i.e., observation) paths. From the interference output, both the detector and reference pinhole were placed at the same distance z of 200 mm. Assuming ω_0=25 μm at the detector and reference pinhole, r and θ_{diff} can be found to be 1.61 mm and 8.06×10^{-3} rad at the interference output, respectively. When thermal excitation of 101 mK is considered (i.e., z_{ref}=200 mm and z_{det}=200.0001 mm), the diffraction-induced phase change can be calculated as $2.2\times10^{-6}\pi$. This is quite negligible (>0.001%) compared to the measured phase shift of 2.2π observed in the experimental measurements. Note that this phase change of $2.2\times10^{-6}\pi$ would give a NEP of only $\sim6.8\times10^{-5}$ pW.

Table 5.4: NEP and NETD for different noise sources

Noise source	**NEP (pW)**	**NETD (mK)**
Temperature fluctuations	3.05	4.43
Mechanical fluctuations	0.38	0.55
Laser pressure induced deflections	0.007	0.01
CMOS readout	0.013	0.0184
Diffraction	6.8×10^{-5}	1×10^{-4}
Total	**3.07**	**4.5**

Limiting Noise and Detector Improvement

To understand the limiting noise source of our detector, Table 5.4 presents the NEP for different noise sources and the corresponding NETD values calculated from Eq. 5.15. It can be clearly observed that temperature fluctuations dominate over all other noise sources. It should be noted that the heat conduction of our detector is dominated by phonons, therefore, temperature fluctuations noise mostly arises from the thermal conductance noise. Using heat conduction of the four straight tethers, it can be found that out of 3.05 pW, ∼2.2 pW noise originates from the phonons and 0.85 pW comes from the photons.

The thermal conductance noise can be greatly reduced if we can use SiO_2 instead of SiN_x in the support straight tethers, as the thermal conductivity of SiO_2 is lower than that of SiN_x [232]. With the length l of 100 μm and width w of 2 μm for the Ti-SiO_2 tether, support leg thermal conductance G_{leg} can be calculated as $\sim1.8\times10^{-8}$ WK^{-1}, which gives a total thermal conductance G_{T} of $\sim3.3\times10^{-8}$ WK^{-1}. This is ∼37% lower thermal conductance than that of our fabricated structure. With the same absorber design (Ti-SiN_x-Ni perforated structure), the detector with Ti-SiO_2 tethers will show a NEP of ∼2 pW and a detectivity of $\sim6\times10^{9}$ cm$\sqrt{Hz}$/W, which will be an improvement compared to our present design.

The detector performance can be further improved without changing into SiO_2 if we

can increase the length of the support tether legs. This can be achieved by using serpentine cantilevers instead of straight tethers, as shown in Fig. 5.28. Different segments of a serpentine tether are highlighted, along with lengths of l_0, $l_{\rm p}$, $l_{\rm ini}$, and $l_{\rm fin}$. N presents the number of repetition. With a total length l of 900 μm (i.e., l_0=50 μm, $l_{\rm p}$=5 μm, $l_{\rm ini}$=10 μm, $l_{\rm fin}$=10 μm, and N=7) and width w of 2 μm for the Ti-SiN$_x$ serpentine tether, support leg thermal conductance $G_{\rm leg}$ can be calculated as $\sim$4.3$\times$10^{-9} WK^{-1}. This is quite negligible compared to the radiation thermal conductance $G_{\rm rad}$ of $\sim$1.5$\times$10^{-8} WK^{-1} for our Ti-SiN$_x$-Ni detector. With the absorber design remaining the same, a detector with long serpentine tethers will show a NEP of $\sim$1.1 pW and a detectivity of $\sim$7.6$\times$10^9 cm$\sqrt{Hz}$/W, which is even higher than using Ti-SiO$_2$ straight tethers. Note that from [233], the spring constant $K_{\rm serp}$ of a serpentine tether can be calculated as 0.0088 Nm^{-1}, which will give a mechanical fluctuation of $\sim$0.7 nm and photon pressure induced deflection of $\sim$0.68 nm, which quite negligible ($\sim$0.1%) compared to the He-Ne probe laser. The diffraction will also be quite negligible if the probe beam is focused on the detector absorber. The major drawback of this design is the stress breakdown during fabrication, mainly due to its high aspect ratio (450:1). Moreover, there will be additional torsional movements from the serpentine tethers, which might bend the detector absorber at different angles, and hence, affect the overall thermal detection.

5.4.6 Summary

In conclusion, we reported a highly sensitive uncooled infrared detector that shows enhanced performance with a minimum amount of material. Using subwavelength perforations, we designed a Ti-SiN$_x$-Ni (i.e., metal-insulator-metal) infrared absorber that utilizes Fabry-Perot-like cavity coupling to realize excellent broadband absorption (maximum of $\sim$90%) with an overall fill factor of only 28%. The designed absorber shows at least $\sim$30% higher absorption-per-unit-mass compared to the recently reported perforated metastructures [160, 132]. We analyzed the fabricated structure as an uncooled infrared detector using Mach Zehnder interferometer. Operating in high vacuum ($\sim$10^{-4}

torr), our detector demonstrated a minimum NETD of 4.5 mK and a maximum detectivity of 3.8×10^9 cm$\sqrt{Hz}$/W, with a time constant of $\sim$7.4 ms. Having a comprehensive analysis over $\sim$70 previously published works (commercial and non-commercial), we showed that our measured detectivity might be the highest detectivity D^* for any room temperature infrared thermal detector.

Chapter 6

Conclusions

Work on two separate projects has been discussed in this thesis. In the first project, a detailed theoretical and experimental analysis was performed to study the effects of photon diffusion on heat transfer in microscale graphite sheets. An Nd:YAG continuous-wave laser with laser intensities of 10 kW cm^{-2} and 20 kW cm^{-2} was used to heat up 40 μm and 100 μm thick graphite sheets. Temperatures were found to rise up extremely high (2000K and above) within milliseconds, and these temperatures were recorded using a 2-color, high-speed pyrometer. To compare the experimental measurements, a thermal model of heat conduction was developed across the thickness of the graphite sheet. Necessary thermal properties, i.e., thermal conductivity and specific heat were analytically modeled to solve the heat equation across the sheet. When both photon diffusion and lattice vibrations were incorporated into the thermal conductivity of graphite, the results matched well with previous experimental data. However, to have a better understanding, the transient temperatures were numerically solved in two ways; one with only lattice conductivity and the other with combined lattice and photon conductivity. Significant temperature differences were observed between the two simulations with time. However, temperatures simulated with combined conductivity were found in good agreement with our experimental measurements, as expected from our earlier

analysis of thermal conductivity. This validates the contribution of photon diffusion to heat conduction in high-absorbing microscale graphite.

In the second project, a thermal detector was developed based on a new infrared structure technology that minimizes the amount of condensed matter necessary to create a level of absorption. The highest detectivity was reported for any room temperature long-wave infrared (LWIR, $\lambda \sim 8-12$ μm) thermal detector published to date. A sub-wavelength perforated metamaterial membrane was designed and fabricated using three nanoscale films: Ti, SiN_x, and Ni. Due to free carrier absorption of Ti and Ni, and vibrational phonon absorption of SiN_x, the detector membrane realizes excellent absorption per unit thermal mass. Using an optical read-out technique, i.e., Mach Zehnder interferometer, a detectivity of $3.8\times10^{9}\text{cm}\sqrt{Hz}/\text{W}$ and a noise equivalent temperature difference (NETD) of 4.5 mK were observed, with a time constant of $\sim$ 7.4 ms when operating in vacuum (i.e., 1.6×10^{-4} torr). The notable features of this work are as follows:

- Using subwavelength perforations in Ti, SiN_x, and Ni layers, the overall absorption area of our detector was designed with a fill factor of only 28% (hole area of 72%), resulting in an average absorption-per-unit-mass of $\sim 7.8\times10^{12}$ kg^{-1} across the LWIR, which is approximately $1.3-27.6$ times higher than the previously reported infrared absorbers.

- The opto-thermal detector shows the highest detectivity over other excellent state-of-the-art works (nearly 70 works) in a field usually typified by incremental performance advances over decades.

References

[1] M Meschke, W Guichard, and J Pekola. Single-mode heat conduction by photons. *Nature*, 444:187–190, 2006.

[2] C J Durrant. *The Atmosphere of the Sun.* Bristol and Philadelphia: Verlag Adam Hilger, 1988.

[3] S Rosseland. *Theoretical Astrophysics: Atomic Theory and the Analysis of Stellar Atmospheres and Envelops.* Oxford: Clarendon, 1936.

[4] S P J Clarke. Radiative transfer in the earth's mantle. *Trans. Am. Geophys. Union*, 38:931–938, 1957.

[5] J R Aronson, S W Eckroad, A G Emslie, R K McConnell, and P C von Thüna. Radiative thermal conductivity in planetary interiors. *Nature*, 216:1096–1097, 1967.

[6] C Clauser. *Handbook of Terrestrial Heat Flow Density Determination*, page 143–165. Dordrecht: Kluwer, 1988.

[7] B S Kellett. The steady flow of heat through hot glass. *J. Opt. Soc. Am.*, 42(5):339–343, 1952.

[8] L Genzel. Calculation of radiation conductivity of glasses. *Glastech. Ber.*, 26(3):69–71, 1953.

[9] D W Lee and W D Kingery. Radiation energy transfer and thermal conductivity of ceramic oxides. *J. Am. Ceram. Soc.*, 43:594–607, 1960.

[10] O K Dudko and G H Weiss. Photon diffusion in biological tissues. *Diffus. Fundam.*, 2:114.1–21, 2005.

[11] M A Ansari, S Alikhani, E Mohajerani, and R Massudi. The numerical and experimental study of photon diffusion inside biological tissue using boundary integral method. *Opt. Commun.*, 285(5):851–855, 2012.

[12] F Martelli. An ABC of near infrared photon migration in tissues: The diffusive regime of propagation. *J. Near Infrared Spectrosc.*, 20(1):29–42, 2012.

[13] B Wallace and P J Atzberger. Förster resonance energy transfer: Role of diffusion of fluorophore orientation and separation in observed shifts of FRET efficiency. *PLoS ONE*, 12(5):e0177122, 2017.

[14] A F Reis, A F G Monte, and G A Alves. Evidence of resonant energy transfer between CdSe/ZnS quantum dots and neutral red dye molecules. *J. Luminescence*, 204:349–353, 2018.

[15] A R Clapp, I L Medintz, and H Mattoussi. Förster resonance energy transfer investigations using quantum-dot fluorophores. *Chem. Phys. Chem.*, 7:47–57, 2006.

[16] J R Aronson, L H Bellotti, W Eckroad, A G Emslie, R K McConnell, and P C von Thüna. Infrared spectra and radiative thermal conductivity of minerals at high temperatures. *J. Geophys. Res.*, 75:3444–3456, 1970.

[17] C Clauser and E Huenges. *Rock Physics and Phase Relations*, page 105–126. Washington, DC: American Geophysical Union, 1995.

[18] H Keppler, L S Dubrovinsky, O Narygina, and I Kantor. Optical absorption and radiative thermal conductivity of silicate perovskite to 125 gigapascals. *Science*, 322(5907):1529–1532, 2008.

[19] T Mitra, A K Brown, D M Bernot, S Defrances, and J J Talghader. Laser acceleration of absorbing particles. *Opt. Exp.*, 26(6):6639–6652, 2018.

[20] M A Al-Nimr. Heat transfer mechanisms during short-duration laser heating of thin metal films. *Int. J. Thermophys.*, 18:1257–1268, 1997.

[21] W Jiang, X Z Xie, X Wei, W Hu, Q L Ren, and Z S Zou. High contrast patterning on glass substrates by 1064 nm pulsed laser irradiation. *Opt. Mater. Express*, 7(5):1565–1574, 2017.

[22] A S Fialkov. *Carbon Interlayer Compounds and Compositions Thereof.* Moscow: Moscow Press, 1997.

[23] M Becker. *Heat Transfer: a Modern Approach.* New York: Plenum, 1986.

[24] J R Cannon. *The One-Dimensional Heat Equation.* Cambridge: Cambridge University Press, 1984.

[25] J Fourier. *The Analytical Theory of Heat.* Paris: Firmin Didot Father and Son, 1822.

[26] J Stefan. über die beziehung zwischen der w?rmestrahlung und der temperatur. *Wiener Ber. II*, 79:391–428, 1879.

[27] L Boltzmann. Ableitung des stefan'schen gesetzes, betreffend die abhängigkeit der wärmestrahlung von der temperatur aus der electromagnetischen lichttheorie. *Ann. Phys. Chem.*, 22:291, 1884.

[28] M Plank. *The Theory of Heat Radiation.* Philadelphia, PA: M P Blakiston's Sons & Co, 1914.

[29] V I Sapritsky and *et al*. Precision blackbody sources for radiometric standards. *Appl. Opt.*, 36(22):5403–5408, 1997.

[30] V I Sapritsky, B B Khlevnoy, V B Khromchenko, S A Ogarev, S P Morozova, B E Lisiansky, M L Samoylov, V I Shapoval, and K A Sudarev. Blackbody sources for the range 100 k to 3500 k for precision measurements in radiometry and radiation thermometry. *AIP Conf. Proc.*, 684:619, 2003.

[31] A Maurel, M Courty, B Fleutot, H Tortajada, K Prashantha, M Armand, S Grugeon, S Panier, and L Dupont. Highly loaded graphite–polylactic acid composite-based filaments for lithium-ion battery three-dimensional printing. *Chem. Mater.*, 30(21):7484–7493, 2018.

[32] C Hsieh, D Tzou, Z Huang, C Lee, and J Chang. High performance infrared heaters using carbon fiber filaments decorated with alumina layer by microwave-assisted method. *J. Taiwan Inst. Chem. Eng.*, 59:521–525, 2016.

[33] A B Djurišić and E H Li. Optical properties of graphite. *J. Appl. Phys.*, 85:7404–7410, 1999.

[34] T Smausz, B Kondász, T Gera, and *et al*. Determination of uv–visible–nir absorption coefficient of graphite bulk using direct and indirect methods. *Appl. Phys. A*, 123:633, 2017.

[35] P G Klemens. The specific heat and thermal conductivity of graphite. *Aust. J. Phys.*, 6(4):405–409, 1953.

[36] A I Lutcov, V I Volga, and B K Dymov. Thermal conductivity, electric resistivity and specific heat of dense graphites. *Carbon*, 8(6):753–760, 1970.

[37] J W Klett, A D McMillan, N C Gallego, and C A Walls. The role of structure on the thermal properties of graphitic foams. *J. Mater. Sci.*, 39:3659–3676, 2004.

[38] A W Smith and N S Rasor. Observed dependence of the low-temperature thermal and electrical conductivity of graphite on temperature, type, neutron irradiation, and bromination. *Phys. Rev.*, 104:885, 1956.

[39] P G Klemens. Thermal conductivity and lattice vibrational modes. *Sol. Stat. Phys.*, 7:1–98, 1958.

[40] R W Powell and F H Schofeld. The thermal and electrical conductivities of carbon and graphite to high temperatures. *Proc. Phys. Soc.*, 51(1):153–172, 1939.

[41] R W Powell. The thermal and electrical conductivities of a sample of acheson graphite from 0°. to 800°. *Proc. Phys. Soc.*, 49(4):419–426, 1937.

[42] A Radoń and D Lukowiec. Structure of nanographite synthesised by electrochemical oxidation and exfoliation of polycrystalline graphite. *Micro Nano Lett.*, 12:955–959, 2017.

[43] G Chen, W Weng, D Wu, C Wu, J Lu, P Wang, and X Chen. Preparation and characterization of graphite nanosheets from ultrasonic powdering technique. *Carbon*, 42(4):753–759, 2004.

[44] A V Alaferdov, A Gholamipour-Shirazi, M A Canesqui, Y A Danilov, and S A Moshkalev. Size-controlled synthesis of graphite nanoflakes and multi-layer graphene by liquid phase exfoliation of natural graphite. *Carbon*, 69:525–535, 2014.

[45] M Wissler. Graphite and carbon powders for electrochemical applications. *J. Power Sources*, 156(2):142–150, 2006.

[46] P-H Chen and D D L Chung. Thermal and electrical conduction in the compaction direction of exfoliated graphite and their relation to the structure. *Carbon*, 77:538–550, 2014.

[47] C N Hooker, A R J P Ubbelohde, and D A Young. Thermal conductance of graphite in relation to its defect structure. *Proc. Royal Soc. A*, 276:83–95, 1963.

[48] N Nouri, F Panerai, K A Tagavi, N N Mansour, and A Martin. Evaluation of the anisotropic radiative conductivity of a low-density carbon fiber material from realistic microscale imaging. *Int. J. Heat Mass Trans.*, 95:535–539, 2016.

[49] N Nouri. *Radiative conductivity analysis of low-density fibrous materials.* PhD thesis, University of Kentucky, 2015.

[50] B J Stagg and T T Charalampopoulos. Refractive indices of pyrolytic graphite, amorphous carbon, and flame soot in the temperature range 25° to 600°c. *Combust. Flame*, 94(4):381–396, 1993.

[51] E I Zhmurikov, I V Savchenko, S V Stankus, O S Yatsuk, and L B Tecchio. Measurements of the thermophysical properties of graphite composites for a neutron target converter. *Nucl. Instrum. Methods Phys. Res. A*, 674:79–84, 2012.

[52] R Siegel and J R Howell. *Thermal Radiation Heat Transfer vol III.* NASA SP−164, 1971.

[53] M F Modest. *Radiative Heat Transfer.* New York:Academic, 2003.

[54] R Franz and G Wiedemann. Ueber die wärme-leitungsfähigkeit der metalle. *Ann. Phys.*, 165:497–531, 1853.

[55] M Levy and P Wong. The oxidation of pyrolytic graphite at various temperatures and air velocities. Technical report, Report No: AD620005, US Army Materials Research Agency, MA, 1965.

[56] B W Olesen and K C Parsons. Introduction to thermal comfort standards and to the proposed new version of en iso 7730. *Energy Build.*, 34(6):537–548, 2002.

[57] Olesen B W. International standards for the indoor environment. *Indoor Air*, 14:18–26, 2004.

[58] V E Bazhenov, A V Koltygin, Y V Tselovalnik, and A V Sannikov. Determination of interface heat transfer coefficient between aluminum casting and graphite mold. *Russ. J. Nonferr. Met.*, 58:114–123, 2017.

[59] A Magnus. Die spezifische wärme des kohlenstoffs, siliziums und siliziumkarbids bei hohen temperaturen. *Ann. Phys.*, 70:303, 1923.

[60] A G Worthing. Atomic heats of tungsten and of carbon at incandescent temperatures. *Phys. Rev.*, 12(3):199–225, 1918.

[61] W DeSorbo and W W Tyler. The specific heat of graphite from 13° to 300°k. *J. Chem. Phys.*, 21:1660–1663, 1953.

[62] E D West and S Ishihara. In *3rd ASME Symp. on Thermophysical Properties (Purdue Univ., USA).*, page 146, 1965.

[63] P H Jerry. *Chemical Engineering Handbook*. New York: McGraw-Hill, 1950.

[64] R A McDonald. Heat content and heat capacity of an extruded graphite from 341° to 1723° k. *J. Chem. Eng. Data*, 10(3):243, 1965.

[65] A T D Butland and R J Maddison. The specific heat of graphite: An evaluation of measurements. *J. Nucl. Mater.*, 49(1):45–56, 1973.

[66] L F Shampine and M W Reichelt. The matlab ode suite. *SIAM J. Sci. Comput.*, 18(1):1–22, 1997.

[67] R P Shea. *Design and fabrication of state of the art uncooled thermopile infrared detectors with cavity coupled absorption.* PhD thesis, University of Minnesota, Twin Cities, 2013.

[68] C Lavers, K Franks, M Floyd, and A Plowman. Application of remote thermal imaging and night vision technology to improve endangered wildlife resource management with minimal animal distress and hazard to humans. *J. Phys.: Conf. Ser.*, 15:207–212, 2005.

[69] S Liu, M Gao, V John, Z Liu, and E Blasch. Deep learning thermal image translation for night vision perception. *ACM Trans. Intelligent Sys. Tech.*, 12(1):9, 2020.

[70] C Rash, R Verona, and J Crowley. Human factors and safety considerations of night-vision systems flight using thermal imaging systems. *Proc. SPIE*, 1290:142–164, 1990.

[71] K Chrzanowski. Review of night vision technology. *Opto-Electronics Rev.*, 21(2):153–181, 2013.

[72] J A Ratches. Current and future trends in military night vision applications. *Ferroelectrics*, 342(1):183–192, 2006.

[73] J I P Quesada, editor. *Application of Infrared Thermography in Sports Science*. Springer International Publishing, 2017.

[74] G J Tattersall. Infrared thermography: A non-invasive window into thermal physiology. *Comp. Biochem. Physiol., Part A: Mol. Integr. Physiol.*, 202:78–98, 2016.

[75] G Bellisola and C Sorio. Infrared spectroscopy and microscopy in cancer research and diagnosis. *Am. J. Cancer Res.*, 2(1):1–21, 2012.

[76] A Rogalski, M Kopytko, and P Martyniuk. *Antimonide-based Infrared Detectors: A New Perspective*. SPIE Press Book, 2018.

[77] D Landgrebe, C Haake, T Höpfner, S Beutel, B Hitzmann, T Scheper, M Rhiel, and K F Reardon. On-line infrared spectroscopy for bioprocess monitoring. *Appl. Microbiol. Biotechnol.*, 88:11–22, 2010.

[78] F Baldini, A N Chester, J Homola, and S Martellucci, editors. *Optical Chemical Sensors*. Springer, Netherlands, 2006.

[79] G Gerlach and H Budzier. *Thermal Infrared Sensors: Theory, Optimisation and Practice*. Wiley, 2011.

[80] C Li, C J Han, and G Skidmore. Overview of drs uncooled vox infrared detector development. *Opt. Engi.*, 50:061017, 2011.

[81] R A Wood. Uncooled thermal imaging with monolithic silicon focal planes. *Proc. SPIE*, 2020(Infrared Technology XIX.):322–329, 1993.

[82] C Li, G Skidmore, C Howard, E Clarke, and Han C J. Advancement in 17-micron pixel pitch uncooled focal plane arrays. *Proc. SPIE*, 7298(Infrared Technology and Applications XXXV):72980S, 2009.

[83] W A Radford, R Wyles, J Wyles, J B Varesi, M Ray, D F Murphy, A Kennedy, A Finch, E A Moody, F Cheung, R Coda, and S T Baur. Microbolometer uncooled infrared camera with 20-mk NETD. *Proc. SPIE*, 3436(Infrared Technology and Applications XXIV), 1998.

[84] G D Skidmore and C G Howard. Pixel structure having an umbrella type absorber with one or more recesses or channels sized to increase radiation absorption, 2007. US Patent 7,622,717 B2.

[85] A S Gawarikar, R P Shea, and J J Talghader. High detectivity uncooled thermal detectors with resonant cavity coupled absorption in the long-wave infrared. *IEEE Tran. Elec. Dev.*, 60:2586–2591, 2013.

[86] M Foote, E Jones, and T Caillat. Uncooled thermopile infrared detector linear arrays with detectivity greater than $10^9 cmHz^{1/2}/W$. *IEEE Tran. Elec. Dev.*, 45:1896–1902, 1998.

[87] R Shea, A Gawarikar, and J Talghader. Process integration of co-sputtered bismuth telluride/antimony telluride thermoelectric junctions. *IEEE/ASME J. Microelectromechanical Sys.*, 23:681–688, 2014.

[88] J R Vig, R L Filler, and Y Kim. Uncooled ir imaging array based on quartz microresonators. *J. Microelectromech. Sys.*, 5:131–137, 1996.

[89] P Kao and S Tadigadapa. Micromachined quartz resonator based infrared detector array. *Sens. Actuat. A: Phys.*, 149:189–192, 2009.

[90] A Blaikie, D Miller, and B J Alemán. A fast and sensitive room-temperature graphene nanomechanical bolometer. *Nat. Comm.*, 10:4726, 2019.

[91] W C Ang, P Kropelnicki, H Campanella, Y Zhu, A B Randles, H Cai, Y A Gu, K C Leong, and C S Tan. Aln-based piezoelectric resonator for infrared sensing application. In *2014 IEEE 27th International Conference on Micro Electro Mechanical Systems (MEMS)*, pages 688–691. IEEE, 2014.

[92] M Steffanson and I W Rangelow. Microthermomechanical infrared sensors. *OptoElectronics Rev.*, 22(1):1–15, 2014.

[93] B Li. Design and simulation of an uncooled double-cantilever microbolometer with the potential for ∼mK NETD. *Sensors and Actuators*, 112:351–359, 2004.

[94] A Boisen, S Dohn, S S Keller, S Schmid, and M Tenje. Cantilever-like micromechanical sensors. *Rep. Prog. Phys.*, 74:036101, 2011.

[95] L Mao, T Cheng, D Chen, and Q Zhang. A holistic approach performance analysis of substrate-free focal plane array. *J. Appl. Phys.*, 112:074502, 2012.

[96] J R Barnes, R J Stephenson, C N Woodburn, S J O'Shea, M E Welland, T Rayment, J. K. Gimzewski, and C Gerber. A femtojoule calorimeter using micromechanical sensors. *Rev. Sci. Instruments*, 65:3793, 1994.

[97] E A Wachter, T Thundat, P I Oden, R J Warmack, P G Datskos, and S L Sharp. Remote optical detection using microcantilevers. *Rev. Sci. Instruments*, 67:3434, 1996.

[98] M Wagner, E Ma, J Heanue, and S Wu. Solid state optical thermal imagers. *Infrared Tech. and App. XXXIII: Proc. SPIE*, 6542:65421P, 2007.

[99] A N Enemuo, R R Chaudhuri, Y Song, and S-W Seo. Thermo-optic sensor based on resonance waveguide grating for infrared/thermal imaging. *IEEE Sensors J.*, 15:4213–4217, 2015.

[100] A Rogalski. Infrared detectors: status and trends. *Prog. Quantum Electron*, 27:59–210, 2003.

[101] A Rogalski. *Infrared Detectors*. CRC Press, 2010.

[102] K Ustun and G Turhan-Sayan. Wideband long wave infrared metamaterial absorbers based on silicon nitride. *J. Appl. Phys.*, 120:203101, 2016.

[103] H Hajian, A Ghobadi, B Butun, and E Ozbay. Active metamaterial nearly perfect light absorbers: a review [invited]. *J. Opt. Soc. Am. B*, 36:F131– F143, 2019.

[104] P Yu, L V Besteiro, Y Huang, J Wu, L Fu, H H Tan, C Jagadish, G P Wiederrecht, A O Govorov, and Z Wang. Broadband metamaterial absorbers. *Adv. Opt. Mater.*, 7:1800995, 2019.

[105] J Grant, Y Ma, S Saha, A Khalid, and D R Cumming. Polarization insensitive, broadband terahertz metamaterial absorber. *Opt. Lett.*, 36:3476–3478, 2011.

[106] S He and T Chen. Broadband thz absorbers with graphene-based anisotropic metamaterial films. *IEEE Trans. Terahertz Sci. Technol.*, 3:757–763, 2013.

[107] I H Lee, D Yoo, P Avouris, T Low, and S H Oh. Graphene acoustic plasmon resonator for ultrasensitive infrared spectroscopy. *Nat. Nanotechnol.*, 14:313–319, 2019.

[108] S Chen, M Autore, J Li, P Li, P Alonso-Gonzalez, Z Yang, L Martín-Moreno, R Hillenbrand, and A Y Nikitin. Acoustic graphene plasmon nanoresonators for field enhanced infrared molecular spectroscopy. *ACS Photon.*, 4:3089–3097, 2017.

[109] X Hu, M Li, Z Ye, W Y Leung, K M Ho, and S Y Lin. Design of midinfrared photodetectors enhanced by resonant cavities with subwavelength metallic gratings. *Appl. Phys. Lett.*, 93:241108, 2008.

[110] D G Cahill, P V Braun, G Chen, D R Clarke, S Fan, K E Goodson, P Keblinski, W P King, G D Mahan, A Majumdar, H J Maris, S R Phillpot, E Pop, and L Shi. Nanoscale thermal transport. ii. 2003–2012. *Appl. Phys. Rev.*, 1:011305, 2014.

[111] J J Greffet, R Carminati, K Joulain, J P Mulet, S Mainguy, and Y Chen. Coherent emission of light by thermal sources. *Nature*, 416:61–64, 2002.

[112] C Arnold, F Marquier, M Garin, F Pardo, S Collin, N Bardou, J L Pelouard, and J J Greffet. Coherent thermal infrared emission by two-dimensional silicon carbide gratings. *Phys. Rev. B*, 86:035316, 2012.

[113] S Chen, Z Chen, J Liu, J Cheng, Y Zhou, L Xiao, and K Chen. Ultra-narrow band mid-infrared perfect absorber based on hybrid dielectric metasurface. *Nanomaterials*, 9:1350, 2019.

[114] Y J Jen, Y J Huang, W C Liu, and Y W Lin. Densely packed aluminum-silver nanohelices as an ultra-thin perfect light absorber. *Sci. Rep.*, 7:39791, 2017.

[115] J Y Jung, K Song, J H Choi, J Lee, D G Choi, J H Jeong, and D P Neikirk. Infrared broadband metasurface absorber for reducing the thermal mass of a microbolometer. *Sci. Rep.*, 7:430, 2017.

[116] C M Watts, X Liu, and W J Padilla. Metamaterial electromagnetic wave absorbers. *Adv. Opt. Mater.*, 24:OP98–OP120, 2012.

[117] J Tissot, C Trouilleau, B Fieque, A Crastes, and O Legras. Uncooled microbolometer detector: recent developments at ulis. *Opto-Electron. Rev.*, 14:25–32, 2006.

[118] W Ma, Y Wen, and X Yu. Broadband metamaterial absorber at mid-infrared using multiplexed cross resonators. *Opt. Express*, 21:30724–30730, 2013.

[119] T D Dao, K Chen, S Ishii, A Ohi, T Nabatame, M Kitajima, and T Nagao. Infrared perfect absorbers fabricated by colloidal mask etching of al–al_2o_3–al trilayers. *ACS Photon.*, 2:964–970, 2015.

[120] C H Fann, J Zhang, M ElKabbash, W R Donaldson, E M Campbell, and C Guo. Broadband infrared plasmonic metamaterial absorber with multipronged absorption mechanisms. *Opt. Express*, 27:27917–27926, 2019.

[121] K Ustun and G Turhan-Sayan. Ultra-broadband long-wavelength infrared metamaterial absorber based on a double-layer metasurface structure. *J. Opt. Soc. Amer. B*, 34:456–462, 2017.

[122] P Bouchon, C Koechlin, F Pardo, R Haïdar, and J L Pelouard. Wideband omnidirectional infrared absorber with a patchwork of plasmonic nanoantennas. *Opt. Lett.*, 37:1038–1040, 2012.

[123] Y Cui, K H Fung, J Xu, H Ma, Y Jin, S He, and N X Fang. Ultrabroadband light absorption by a sawtooth anisotropic metamaterial slab. *Nano. Lett.*, 12:1443–1447, 2012.

[124] Y Li, B An, L Li, and J Gao. Broadband lwir and mwir absorber by trapezoid multilayered grating and sio_2 hybrid structures. *Opt. Quantum Electron*, 50:459, 2018.

[125] Y K Zhong, S M Fu, N P Ju, M H Tu, B R Chen, and A Lin. Fully planarized perfect metamaterial absorbers with no photonic nanostructures. *IEEE Photon. J*, 8:2200109, 2016.

[126] K Gorgulu, A Gok, M Yilmaz, K Topalli, N Bıyıklı, and A K Okyay. All-silicon ultra-broadband infrared light absorbers. *Sci. Rep.*, 6:38589, 2016.

[127] Y Zhou, Z Liang, Z Qin, E Hou, X Shi, Y Zhang, Y Xiong, Y Tang, Y Fan, F Yang, J Liang, C Chen, and J Lai. Small–sized long wavelength infrared absorber with perfect ultra–broadband absorptivity. *Opt. Express*, 28:1279–1290, 2020.

[128] B M Adomanis, C M Watts, M Koirala, X Liu, T Tyler, K G West, T Starr, J N Bringuier, A F Starr, N M Jokerst, and W J Padilla. Bi-layer metamaterials as fully functional near-perfect infrared absorbers. *Appl. Phys. Lett.*, 107:021107, 2015.

[129] A Ghobadi, H Hajian, M Gokbayrak, S A Dereshgi, A Toprak, B Butun, and E Ozbay. Visible light nearly perfect absorber: an optimum unit cell arrangement for near absolute polarization insensitivity. *Opt. Exp.*, 25:27624–27634, 2017.

[130] J Zhou, A F Kaplan, L Chen, and L J Guo. Experiment and theory of the broadband absorption by a tapered hyperbolic metamaterial array. *ACS Photon.*, 1:618–624, 2014.

[131] M Desouky, A M Mahmoud, and M A Swillam. Silicon based mid-ir super absorber using hyperbolic metamaterial. *Sci. Rep.*, 8:2036, 2018.

[132] R Cetin and O Erturk. Subwavelength perforated absorbers for infrared detectors. *Opt. Exp.*, 28(22):33699–33707, 2020.

[133] K Ustun and G Turhan-Sayan. Broadband lwir and mwir metamaterial absorbers with a simple design topology: almost perfect absorption and super-octave band operation in mwir band. *J. Opt. Soc. Am. B*, 34:D86–D94, 2017.

[134] A A Cruz-Cabreraa, S A Kemmea, M J Cicha, A R Ellisa, J R Wendta, A M Rowena, S Samorab, M J Martineza, D A Scrymgeoura, and D W Peters. Demonstration of thermal emissions control. *Proc. SPIE*, 7591:75910P, 2010.

[135] S R Calhoun, V C Lowry, R Stack, R N Evans, J R Brescia, C J Fredricksen, J Nath, R E Peale, E M Smith, and J W Cleary. Effect of dispersion on metal–insulator–metal infrared absorption resonances. *MRS Commun.*, 8:830–834, 2018.

[136] L H Liu, W J I Debenedetti, T Peixoto, S Gokalp, N Shafiq, J F Veyan, D J Michalak, R Hourani, and Y J Chabal. Morphology and chemical termination of hf-etched si_3n_4 surfaces. *Appl. Phys. Lett.*, 105:261603, 2014.

[137] G Gomard, E Drouard, X Letartre, X Meng, A Kaminski, A Fave, M Lemiti, E Garcia-Caurel, and C Seassal. Two-dimensional photonic crystal for absorption enhancement in hydrogenated amorphous silicon thin film solar cells. *J. Appl. Phys.*, 108:123102, 2010.

[138] E S Awad, N Al-Khalli, M Abdel-Rahman, M Alduraibi, and N Debbar. Comparison of v_2o_5 microbolometer optical performance using nicr and ti thin-films. *IEEE Photon. Tech. Lett.*, 27(5):462–465, 2014.

[139] A Das and J J Talghader. Enhanced absorption per unit mass for infrared arrays using subwavelength metal–dielectric structures. *J. Opt. Soc. Am. B*, 38:183–193, 2021.

[140] H Wang, X Liu, L Wang, and Z Zhang. Anisotropic optical properties of silicon nanowire arrays based on the effective medium approximation. *Int. J. Therm. Sci.*, 65:62–69, 2013.

[141] Y Zhang, Y Cui, W Wang, K H Fung, T Ji, Y Hao, and F Zhu. Effective medium analysis of absorption enhancement in short-pitch metal grating incorporated organic solar cells. *Opt. Exp.*, 24:A1408–A1418, 2016.

[142] X Zhao, C Chen, A Li, G Duan, and X Zhang. Implementing infrared metamaterial perfect absorbers using dispersive dielectric spacers. *Opt. Exp.*, 27:1727–1739, 2019.

[143] K Han and C H Chang. Numerical modeling of sub-wavelength anti-reflective structures for solar module applications. *Nanomaterials*, 4:87–128, 2014.

[144] H J Shin and G Ok. Terahertz guided mode resonance sensing platform based on freestanding dielectric materials: high q-factor and tunable spectrum. *Appl. Sci.*, 10:1013, 2020.

[145] H J Shin, S H Kim, K Park, M C Lim, S W Choi, and G Ok. Free-standing guided-mode resonance humidity sensor in terahertz. *Sens. Actuators A*, 268:27–31, 2017.

[146] M A Golub and A A Friesem. Analytic design and solutions for resonance domain diffractive optical elements. *J. Opt. Soc. Am. A*, 24:687–695, 2007.

[147] M A Golub and A A Friesem. Effective grating theory for resonance domain surface-relief diffraction gratings. *J. Opt. Soc. Am. A*, 22:1115–1126, 2005.

[148] K Bhattarai, S Silva, K Song, A Urbas, S J Lee, Z Ku, and J Zhou. Metamaterial perfect absorber analyzed by a meta-cavity model consisting of multilayer metasurfaces. *Sci. Rep.*, 7:10569, 2017.

[149] G Subramania, A J Fischer, and T S Luk. Optical properties of metal-dielectric based epsilon near zero metamaterials. *Appl. Phys. Lett.*, 101:241107, 2012.

[150] S S Wang and R Magnusson. Theory and applications of guided-mode resonance filters. *Appl. Opt.*, 32:2606–2613, 1993.

[151] G Quaranta, G Basset, O J F Martin, and B Gallinet. Recent advances in resonant waveguide gratings. *Laser Photonics Rev.*, 12:1800017, 2018.

[152] G Basset, G Quaranta, F Lütolf, L Davoine, and M Schnieper. Sub-wavelength gratings for ovds from local interactions to using light-transport. *arXiv:1511.05543*, 17 Nov 2015.

[153] M A Ordal, R J Bell, R W Alexander, L A Newquist, and M R Querry. Optical properties of al, fe, ti, ta, w, and mo at submillimeter wavelengths. *Appl. Opt.*, 27:1203–1209, 1988.

[154] J Kischkat, S Peters, B Gruska, M Semtsiv, M Chashnikova, M Klinkmüller, O Fedosenko, S Machulik, A Aleksandrova, G Monastyrskyi, Y Flores, and W T Masselink. Mid-infrared optical properties of thin films of aluminum oxide, titanium dioxide, silicon dioxide, aluminum nitride, and silicon nitride. *Appl. Opt.*, 51:6789–6798, 2012.

[155] S Boonruang. *Two-dimensional guided mode resonant structures for spectral filtering applications*. PhD thesis, University of Central Florida, 2007.

[156] S J Byrnes. Multilayer optical calculations. *arXiv:1603.02720*, 2016.

[157] M Aalizadeh, A Khavasi, B Butun, and E Ozbay. Large-area, cost-effective, ultra broadband perfect absorber utilizing manganese in metal-insulator-metal structure. *Sci. Rep.*, 8:9162, 2018.

[158] Ansys lumerical fdtd. `https://www.ansys.com/products/photonics/fdtd?utm_source=google&utm_medium=ppc&utm_campaign=brand&utm_content=&utm_term=&campaignid=7013g000000gvjlAAA&creative=&keyword=&matchtype=&network=x&device=c&gclid=Cj0KCQiAyMKbBhD1ARIsANs7rEFn51g4HfOtNvtOevqGHII94iDV5n978sxo_8_s0nSd06eR0k1OJtwaArv7EALw_wcB`.

[159] R L Olmon, B Slovick, T W Johnson, D Shelton, S H Oh, G D Boreman, and M B Raschke. Optical dielectric function of gold. *Phys. Rev. B*, 86:235147, 2012.

[160] A Varpula, K Tappura, J Tiira, K Grigoras, O P Kilpi, K Sovanto, J Ahopeito, and M Prunnila. Nano-thermoelectric infrared bolometers. *APL Photon.*, 6:036111, 2021.

[161] A Tittl, A K U Michel, M Schäferling, X Yin, B Gholipour, L Cui, M Wuttig, T Taubner, F Neubrech, and H Giessen. A switchable midinfrared plasmonic perfect absorber with multispectral thermal imaging capability. *Adv. Mater.*, 27:4597–4603, 2015.

[162] J J Talghader, A S Gawarikar, and R P Shea. Spectral selectivity in infrared thermal detection. *Light: Science Applications*, 1(8):e24, 2012.

[163] A M Shaltout, J Kim, A Boltasseva, V M Shalaev, and A V Kildishev. Ultrathin and multicolour optical cavities with embedded metasurfaces. *Nat. Commmun.*, 9:2673, 2018.

[164] R M H Bilal, M A Saeed, P K Choudhury, M A Baqir, W Kamal, M M Ali, and A A Rahim. Elliptical metallic rings-shaped fractal metamaterial absorber in the visible regime. *Sci. Rep.*, 10:14035, 2020.

[165] F Ding, J Dai, Y Chen, J Zhu, Y Jin, and S I Bozhevolnyi. Broadband near-infrared metamaterial absorbers utilizing highly lossy metals. *Sci. Rep.*, 6:39445, 2016.

[166] L F Francis. *Materials Processing: a Unified Approach.*, chapter Ch. 7: Vapor Processes, pages 513–588. Academic Press, 2016.

[167] PROPERTIES OF HELIUM–NEON LASERS. `https://web.physics.ucsb.edu/~phys128/experiments/laser/LaserFall06.pdf`.

[168] He-Ne lasers: Pros and Cons. https://integratedoptics.com/hene-lasers.

[169] P Kcovsk. Electric circuits as seen by thermal imaging cameras. *The Phys. Teacher*, 57:597, 2019.

[170] Refractive index database: Optical transmission calculator. https://refractiveindex.info/?shelf=main&book=SiO2&page=Kischkat.

[171] A S Gawarikar. *Spectrally Selective High Detectivity Uncooled Detectors for the Long Wave Infrared*. PhD thesis, University of Minnesota Twin Cities, 2013.

[172] R A Wood. *Semiconductors and Semimetals*, chapter 3, pages 43–121. Academic Press, New York, 1997.

[173] Camera Resolution- Teledyne Photometrics. https://www.photometrics.com/learn/camera-basics/camera-resolution.

[174] Noise equivalent temperature difference (NETD)- MH TECH. http://www.mh-elec.com/news-x.php?id=560.

[175] C Chen, Y Huang, K Wu, T G Bifano, S W Anderson, X Zhao, and X Zhang. Polarization insensitive, metamaterial absorber-enhanced longwave infrared detector. *Opt. Exp.*, 28(20):28843–28857, 2020.

[176] Y Shang, X Ye, L Cao, P Song, and J Feng. Coaxial Dual-wavelength Interferometric Method for a Thermal Infrared Focal-plane-array with Integrated Gratings. *Sci. Rep.*, 6:25993, 2016.

[177] Specific heat capacity of metals table chart. https://www.engineersedge.com/materials/specific_heat_capacity_of_metals_13259.htm.

[178] Using the thermal properties of titanium to improve power and reduce aero drag. https://www.highpowermedia.com/Archive/using-the-thermal-properties-of-titanium-to-improve-power-and-reduce-aero-drag.

[179] Titanium− Royal Society of Chemistry. https://www.rsc.org/periodic-table/element/22/titanium#:~:text=Its%20density%20is%204.5%20grams,important%20in%20the%20aerospace%20industry.

[180] P Hidnert. Thermal expansion of titanium. *J. Research of the National Bureau of Standards*, 30:101105, 1943.

[181] YOUNG'S MODULUS OF TITANIUM ALLOYS− AmesWeb. https://amesweb.info/Materials/Youngs-Modulus-of-Titanium.aspx.

[182] Q Song, Z Cui, S Xia, Z Chen, and J Zhang. Measurement of sinx thin film thermal property with suspended membrane structure. *Sensors and Actuators A: Physical*, 112(1):122–126, 2004.

[183] J L Braun, S W King, E R Hoglund, M A Gharacheh, E A Scott, A Giri, J A Tomko, J T Gaskins, A Al-kukhun, G Bhattarai, M M Paquette, G Chollon, B Willey, G A Antonelli, D W Gidley, J Hwang, J M Howe, and P E Hopkins. Hydrogen effects on the thermal conductivity of delocalized vibrational modes in amorphous silicon nitride (a-sin$_x$:h). *Physical Review Materials*, 5:035604, 2021.

[184] L Vicarelli, A Tredicucci, and A Pitanti. Micromechanical bolometers for subterahertz detection at room temperature. *ACS Photonics*, 9:360367, 2022.

[185] C L Tien and T W Lin. Thermal expansion coefficient and thermomechanical properties of sin(x) thin films prepared by plasma-enhanced chemical vapor deposition. *Appl Opt.*, 51(30):72297235, 2012.

[186] X J Xu, Z C Deng, and B Wang. Closed solutions for the electromechanical bending and vibration of thick piezoelectric nanobeams with surface effects. *J. Phys. D: Appl. Phys.*, 46(8):405302, 2013.

[187] R W Powell, R P Tye, and M J Hickman. The thermal conductivity of nickel. *International Journal of Heat and Mass Transfer*, 8(5):679–688, 1965.

[188] Nickel– Lenntech. https://www.lenntech.com/periodic/elements/ni.htm.

[189] P Hidnert. Thermal expansion of some nickel alloys. *J. Research of the National Bureau of Standards*, 58:8992, 1957.

[190] J K Luo, A J Flewitt, S M Spearing, N A Fleck, and W I Milne. Young's modulus of electroplated ni thin film for mems applications. *Materials Letters*, 58(1718):23062309, 2004.

[191] Y Z Deng, S F Tang, H Y Zeng, Z Y Wu, and D K Tung. Experiments on temperature changes of microbolometer under blackbody radiation and predictions using thermal modeling by COMSOL multiphysics simulator. *Sensors*, 18:2593, 2018.

[192] Y Feng, Y Zhao, L Dong, M Liu, X Li, W Ma, X Yu, L Kong, and X Liu. High-speed infrared imaging by an uncooled optomechanical focal plane array. *Appl. Opt.*, 54(34):10189–10195, 2015.

[193] Y Zhao. *Optomechanical uncooled infrared imaging system.* PhD thesis, University of California, 2002.

[194] W Zhao and L Li. The optical surface defect inspection by fringe reflection. *Proc. SPIE*, 9282:928210, 2014.

[195] J Hailong, S Xianyu, L Yuankun, and W Fan. Specular surface measurement based on fringe reflection and analysis of 3D shape reconstruction technique. *Opto-Electronic Engineering*, 35(10):3742, 2008.

[196] U Dillner, E Kessler, and H G Meyer. Figures of merit of thermoelectric and bolometric thermal radiation sensors. *J. Sens. Sens. Syst.*, 2:85–94, 2013.

[197] F Haenschke, E Kessler, U Dillner, A Ihring, U Schinkel, and H G Meyer. New high detectivity linear array for analytical measurement in the room temperature range. *Proc. SPIE*, 8353:83531L, 2012.

[198] M C Foote, M Kenyon, T R Krueger, T A McCann, R Chacon, E W Jones, M R Dickie, J T Schofeld, D J McCleese, S Gaalema, and W Hu. Thermopile detector arrays for space science applications. In *Proceedings of International Thermal Detectors Workshop (TDW'03) (NASA Center for AeroSpace Information)*, pages 2–16—-2–20, 2003.

[199] C Lei, H Mao, Y Yang, W Ou, C Xue, Z Yao, A Ming, W Wang, L Wang, J Hu, and J Xiong. A double-end-beam based infrared device fabricated using CMOS-MEMS process. *Sens. Rev.*, 36:240–248, 2016.

[200] W Ke, Y Wang, H Zhou, T Li, and Y Wang. Design, fabrication, and characterization of a high-performance CMOS-compatible thermopile infrared detector with self-test function. *J. Micromech. Microeng.*, 28:125017, 2018.

[201] W Li, Z Ni, J Wang, and X Li. A front-side microfabricated tiny-size thermopile infrared detector with high sensitivity and fast response. *IEEE Trans. Electron Devices*, 66:2230—-2237, 2019.

[202] T W Shen, K C Chang, C M Sun, and W Fang. Performance enhance of CMOS-MEMS thermoelectric infrared sensor by using sensing material and structure design. *J. Micromech. Microeng.*, 29:025007, 2019.

[203] L Dong, R F Yue, and L T Liu. An uncooled microbolometer infrared detector based on polycrystalline silicon germanium thin film. *Int. J. Nonlinear Sci. Numer. Simul.*, 3:303–306, 2002.

[204] W Schnelle, U Dillner, B Scheike, and L Albrecht. Infrared radiation sensors based on thin flm bolometers. In *Proceedings of 11th International Symposium of the Technical Committee on Photon-Detectors*, page 147–149, 1984.

[205] L Dong, R Yue, and L Liu. An uncooled microbolometer infrared detector based on poly-sige thermistor. *Sens. Actuators A*, 105:286–292, 2003.

[206] S Karanth, M A Sumesh, V Shobha, H G Shanbhogue, and C L Nagendra. Infrared detectors based on thin flm thermistor of ternary mn–ni–co–o on micro-machined thermal isolation structure. *Sens. Actuators A*, 153:69–75, 2009.

[207] M Almasri, D P Butler, and Z Celik-Butler. Self-supporting uncooled infrared microbolometers with low-thermal mass. *J. Microelectromech. Syst.*, 10:469–476, 2001.

[208] W Zhou, Y Yin, J Wu, Y Gao, and Z Huang. Improvements in electrical properties, low frequency noise and detection performance of a mn-based bilayer thin film infrared detector. *Sens. Actuators, A*, 283:196–203, 2018.

[209] Hamamatsu. Data of photovoltaic inassb detector P13894-211MA, n.d. `https://www.hamamatsu.com/us/en/product/optical-sensors/infrared-detector/inassb-photovoltaic-detector.html` and `https://www.hamamatsu.com/content/dam/hamamatsu-photonics/sites/documents/99_SALES_LIBRARY/ssd/p13894_series_kird1133e.pdf`.

[210] D Palaferri, Y Todorov, A Bigioli, A Mottaghizadeh, D Gacemi, A Calabrese, A Vasanelli, L Li, A G Davies, E H Linfeld, F Kapsalidis, M Beck, J Faist, and C Sirtori. Room-temperature 9-μm-wavelength photodetectors and GHz frequency heterodyne receivers. *Nature*, 556:85–88, 2018.

[211] VIGO System S. A. Photovoltaic multiple junction mct detector data in catalog 2018/2019, p. 14, n.d. `https://vigo.com.pl/wp-content/uploads/2017/06/VIGO-Catalogue.pdf`.

[212] VIGO System S. A. Photoconductive mct detector data in catalog 2018/2019, p. 6, n.d. `https://vigo.com.pl/wp-content/uploads/2017/06/VIGO-Catalogue.pdf`.

[213] H Omran, M Medhat, B Saadany, and D Khalil. Mach-zehnder mems interferometer with two Si/air beam splitters. In *IEEE 4th International Design and Test Workshop (Riyadh, Saudi Arabia)*, page 11135959, 2009.

[214] H M Nguyen, M A Dundar, R W van der Heijden, E W J M van der Drift, H W M Salemink, S Rogge, and J Caro. Compact mach-zehnder interferometer based on self-collimation of light in a silicon photonic crystal. *Opt. Exp.*, 18:6437–6446, 2010.

[215] J Tratnik and B Batagelj. Fiber interferometric communications using mach-zehnder interferometer topology. In *IEEE Eurocon (St. Petersburg, Russia)*, page 10798902, 2009.

[216] N M R Hoque and L Duan. A mach-zehnder fabry-perot hybrid fiber-optic interferometer operating at the thermal noise limit. *Sci. Rep.*, 12:12130, 2022.

[217] L Zhang, Y Tang, and L Tong. Micro-/nanofiber optics: Merging photonics and material science on nanoscale for advanced sensing technology. *iScience*, 23:100810, 2020.

[218] B Ouyang, Y Li, M Kruidhof, R Horsten, K W A van Dongen, and J Caro. On-chip silicon mach–zehnder interferometer sensor for ultrasound detection. *Opt. Lett.*, 44:1928–1931, 2019.

[219] Y Gao, Q Gan, Z Xin, X Cheng, and F J Bartoli. Plasmonic machzehnder interferometer for ultrasensitive on-chip biosensing. *ACS Nano*, 5:9836–9844, 2011.

[220] L X C Zhao and L Liu. Ultrahigh sensitivity Mach-Zehnder interferometer sensor based on a weak one-dimensional field confinement silica waveguide. *Sensors*, 21(19):6600, 2021.

[221] H Kroemer and C Kittel. *Thermal Physics*. W. H. Freeman and company, 1980.

[222] E L Dereniak and G D Boreman. *Infrared Detectors and Systems.* Wiley-Interscience, 1996.

[223] G M Rebeiz. *RF MEMS: Theory, design, and technology.* Wiley Hoboken, 2003.

[224] S W Kang, J Fragala, S H Kim, and D Banerjee. Design and electro-thermo-mechanical behavior analysis of Au/Si_3N_4 bimorph microcantilevers for static mode sensing. *Sensors*, 17:2510, 2017.

[225] M Lishchynska, N Cordero, O Slattery, and C Mahony. Spring constant models for analysis and design of MEMS plates on straight or meander tethers. *Sensor Letters*, 4:200–206, 2006.

[226] J C Maxwell. *A treatise on electricity and magnetism.* Clarendon Press, 1873.

[227] R K Bansal. *Strength of Materials.* Laxmi Publications, 2009.

[228] Y Zhao, M Mao, R Horowitz, A Majumdar, J Varesi, P Norton, and J Kitching. Optomechanical uncooled infrared imaging system: Design, microfabrication, and performance. *J. Microelectromechanical Sys.*, 11:136–146, 2002.

[229] A Yariv and P Yeh. *Photonics—Optical Electronics in Modern Communication.* Oxford University Press, 2007.

[230] B E A Saleh and M C Teich. *Fundamentals of Photonics.*

[231] T A Al-Saeed and D A Khalil. Diffraction effects in optical microelectromechanical system Michelson interferometers. *App. Opt.*, 49(20):3960–3966, 2010.

[232] W Zhu, G Zheng, S Cao, and H He. Thermal conductivity of amorphous sio_2 thin film: A molecular dynamics study. *Sci. Rep.*, 8:10537, 2018.

[233] G Barillaro, A Molfeso, A Nannini, and F Pieri. Analysis, simulation, and relative performances of two kinds of serpentine springs. *J. Micromech. Microeng.*, 15:736–746, 2005.

Appendix A

Numerical method for 1D heat transfer

The 1D heat transfer along the x−direction can be expressed as [23, 24],

$$\frac{\partial T}{\partial t} = D\frac{\partial^2 T}{\partial x^2}, D = \frac{K}{\rho C_{\mathrm{P}}}, \tag{A.1}$$

where ρ is the density, C_{P} is the specific heat at constant pressure, and K is thermal conductivity of graphite. This heat equation can be solved using implicit finite difference method, where the first order time-derivative and second order space-derivative can be written as,

$$\frac{\partial T}{\partial t} = \frac{T_i^{l+1} - T_i^l}{\Delta t}, \tag{A.2}$$

$$\frac{\partial^2 T}{\partial x^2} = \frac{T_{i-1}^{l+1} - 2T_i^{l+1} + T_{i+1}^{l+1}}{(\Delta x)^2}, \tag{A.3}$$

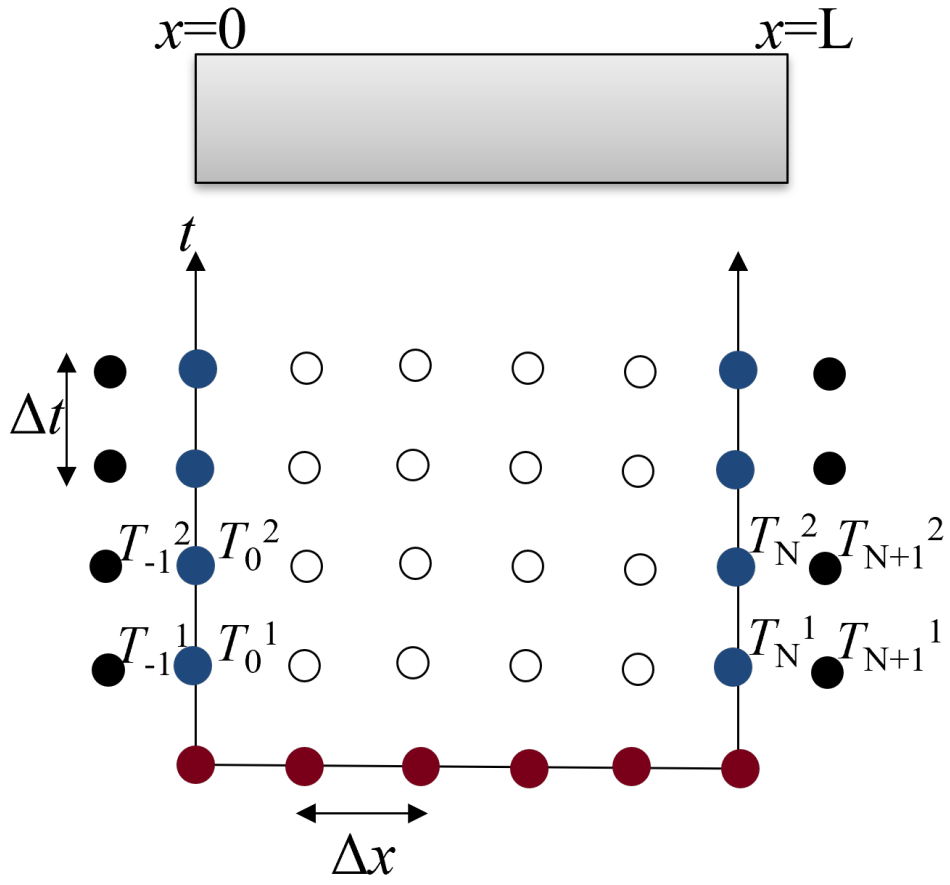

Figure A.1: Space-time grid for one-dimensional parabolic partial differential equation.

Replacing the derivatives in Eq. (A.1)

$$\frac{T_i^{l+1} - T_i^l}{\Delta t} = D\frac{T_{i-1}^{l+1} - 2T_i^{l+1} + T_{i+1}^{l+1}}{(\Delta x)^2}, \tag{A.4}$$

Putting $\lambda = \frac{D\Delta t}{(\Delta x)^2}$ we get

$$-\lambda_{i-1}^{l+1}T_{i-1}^{l+1} + (1 + 2\lambda_i^{l+1})T_i^{l+1} - \lambda_{i+1}^{l+1}T_{i+1}^{l+1} = T_i^l, \tag{A.5}$$

Arranging the equations for i=0 to i=N we get the following system:

$$\begin{bmatrix} -\lambda_{-1}^{l+1} & (1+2\lambda_0^{l+1}) & -\lambda_1^{l+1} & & & & \\ & -\lambda_0^{l+1} & (1+2\lambda_1^{l+1}) & -\lambda_2^{l+1} & & & \\ & & -\lambda_1^{l+1} & (1+2\lambda_2^{l+1}) & -\lambda_3^{l+1} & & \\ & & & \cdots & \cdots & \cdots & \\ & & & & & & \\ & & & & & & \\ & & & & & & \end{bmatrix} \begin{bmatrix} T_{-1}^{l+1} \\ T_0^{l+1} \\ T_1^{l+1} \\ T_2^{l+1} \\ \cdots \\ T_{N-1}^{l+1} \\ T_N^{l+1} \\ T_{N+1}^{l+1} \end{bmatrix} = \begin{bmatrix} T_0^l \\ T_1^l \\ T_2^l \\ \cdots \\ T_{N-1}^l \\ T_N^l \end{bmatrix}, \tag{A.6}$$

The resulting system is a tri-diagonal matrix that can be solved efficiently. But it involves two imaginary nodes, namely T_1 and $T_{\mathrm{N+1}}$ To get rid of these two nodes, finite divided difference for the 1st space derivative according to central difference formula can be used at the end points.

$$\left.\frac{\partial T}{\partial x}\right|_{x=x_i} = \frac{T_{i+1} - T_{i-1}}{2\Delta x}, \tag{A.7}$$

Applying left boundary condition:

$$\left.\frac{\partial T}{\partial x}\right|_{x_i=x_0=0} = \frac{T_1^{l+1} - T_{-1}^{l+1}}{2\Delta x} \Rightarrow T_{-1}^{l+1} = T_1^{l+1} - \left(\frac{\partial T}{\partial x}\right)_0 2\Delta x, \tag{A.8}$$

Applying right boundary condition:

$$\left.\frac{\partial T}{\partial x}\right|_{x_i=x_N=L} = \frac{T_{N+1}^{l+1} - T_{N-1}^{l+1}}{2\Delta x} \Rightarrow T_{N+1}^{l+1} = T_{N-1}^{l+1} + \left(\frac{\partial T}{\partial x}\right)_L 2\Delta x, \tag{A.9}$$

The modified system can be expressed as:

$$\begin{bmatrix} (1+2\lambda_0^{l+1}) & a & & & & & \\ -\lambda_0^{l+1} & (1+2\lambda_1^{l+1}) & -\lambda_2^{l+1} & & & & \\ & -\lambda_1^{l+1} & (1+2\lambda_2^{l+1}) & -\lambda_3^{l+1} & & & \\ & & & \cdots & \cdots & \cdots & \\ & & & -\lambda_{N-2}^{l+1} & (1+2\lambda_{N-1}^{l+1}) & -\lambda_N^{l+1} & \\ & & & & b & (1+2\lambda_N^{l+1}) & \end{bmatrix} \begin{bmatrix} T_0^{l+1} \\ T_1^{l+1} \\ T_2^{l+1} \\ \cdots \\ T_{N-1}^{l+1} \\ T_N^{l+1} \end{bmatrix} = \begin{bmatrix} T_0^{l} \\ T_1^{l} \\ T_2^{l} \\ \cdots \\ T_{N}^{l} \\ T_N^{l} \end{bmatrix}, \tag{A.10}$$

where,

$a = -2\lambda_1^{l+1} + \lambda_1^{l+1}\left(\frac{\partial T}{\partial x}\right)_0 2\Delta x$

$b = -2\lambda_{N-1}^{l+1} - \lambda_{N-1}^{l+1}\left(\frac{\partial T}{\partial x}\right)_N 2\Delta x$

Appendix B

Exothermic heat analysis in graphite microsheet

At temperatures above 700 K, the oxidation of graphite is likely to occur in the ambient air atmosphere. As graphite reacts with oxygen producing carbon monoxide (CO) and carbon dioxide (CO_2), the chemical reaction can release additional exothermic heat. Naturally, this heat release largely depends on the oxidation reaction rate of graphite at elevated temperatures. In previous literature, it has been found that the oxidation rate is dependent on the air velocity when the temperature exceeds 1150 K [55]. Moreover, there is a proportional increase in the oxidation rate at elevated temperatures (1150 K and above) when the air velocity is fixed. As the standard air velocity of the indoor environment (i.e., office, research space) lies between 15 cm/s to 22 cm/s, we have considered this range to calculate the oxidation rates at temperatures 1150 K and above. With the calculated rates, however, we have analyzed the exothermic heat intensity produced in the graphite samples, with the formation of CO and CO_2 gases. In Table. B.1, a detailed analysis of oxidation reaction rates and exothermic heat intensities are shown with different indoor air velocities. The analysis is shown for an elevated temperature of 2800 K. From the table, it is obvious that the exothermic heat

Table B.1: Analysis of exothermic heat intensity in the graphite sheet during oxidation

Standard air velocity (cm/s)	**Oxidation rate (mg/cm^2-min)**	**Exothermic heat intensity I_{ex} (W/cm^2)**		**Percentage=$\frac{I_{ex}}{10 kW/cm^2}$**	
		with CO	with CO_2	with CO	with CO_2
15	7.935	1.15	4.33	0.0115%	0.0433%
18	8.029	1.16	4.38	0.0116%	0.0438%
22	8.212	1.19	4.48	0.0119%	0.0448%

intensities, due to the formation of CO and CO_2 gases, are quite negligible compared to the laser intensities (10 kW/cm^2 and 20 kW/cm^2) used in the experiment. Therefore, the exothermic heat release, and hence the oxidation effects are not included in our thermal model.

Appendix C

Effective surface resistance approximation for Ti-SiN$_x$ absorber

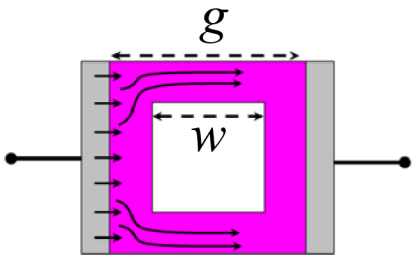

Figure C.1: Schematic illustration of a grid unit cell with distribution of surface currents at the corners of the surface.

To analyze the optical absorption of the subwavelength structure, many articles utilize the concept of optical surface impedance (or simply, resistance) matching with the free space impedance (i.e., 377 Ω). As the thickness of the top metal (t_{Ti}) is smaller than the operating LWIR wavelength λ and skin depth δ, the electromagnetic behavior of

the absorber is assumed to be described by the quasi-static approximation (dc approximation) with an effective sheet resistance [115, 132]. Figure C.1 shows the quasi-static approximation of a grid unit cell of the perforated absorber structure, with grid unit period g and perforation width w. The dc approximation assumes redistribution of the surface current crowding around the corners of the perforated cell, where effective surface resistance can be analytically calculated as [115],

$$R_{\mathrm{f}} = \frac{\rho}{t}\left(\frac{1}{1 - {}^{w}\!/_{g}}\right), \tag{C.1}$$

where ρ is the resistivity and t is the thickness of the top metal (Ti in our case). Considering our design parameters, i.e., w=0.8 μm, g=1 μm, and t_{Ti}=20 nm, the effective surface resistance would be found as 200 $\Omega/\square$.

Appendix D

Supplemental Information on Infrared Absorber and Detector

D.0.1 Analysis of Interference Fringes

Figure 5.21 in chapter 5 shows a spatial image of the interference fringes, as being observed in our CMOS camera. To analyze the fringe patterns, we took linear cross-sections of the fringes and converted the bright and dark colors into 0-255 data scale in MATLAB. Fig. D.1 shows the processed data extracted from the interference fringes. It can be observed that the data measurements are well-fitted to a sinusoidal curve, which can be useful to analyze the amount of phase change, i.e., the shift in the fringes as a measurement of the temperature change.

For thermal excitation, we calibrated the IR source with a commercial microbolometer camera (Jenoptik IR-TCM 384). Fig. D.2 presents the observed temperatures of the IR source over 60 s (1 minute) while operating near room temperature. The increase in temperature can be compared to a linear fit, with a slope $\Delta T/\Delta t$ of $\sim$101 mK/s. This implies that with a stabilized power supply of 1 full second, the average temperature increase ΔT in the IR source would be 101 mK.

We excited the thermal detector by a chopped IR power (f_c=10 Hz) over 1 full second

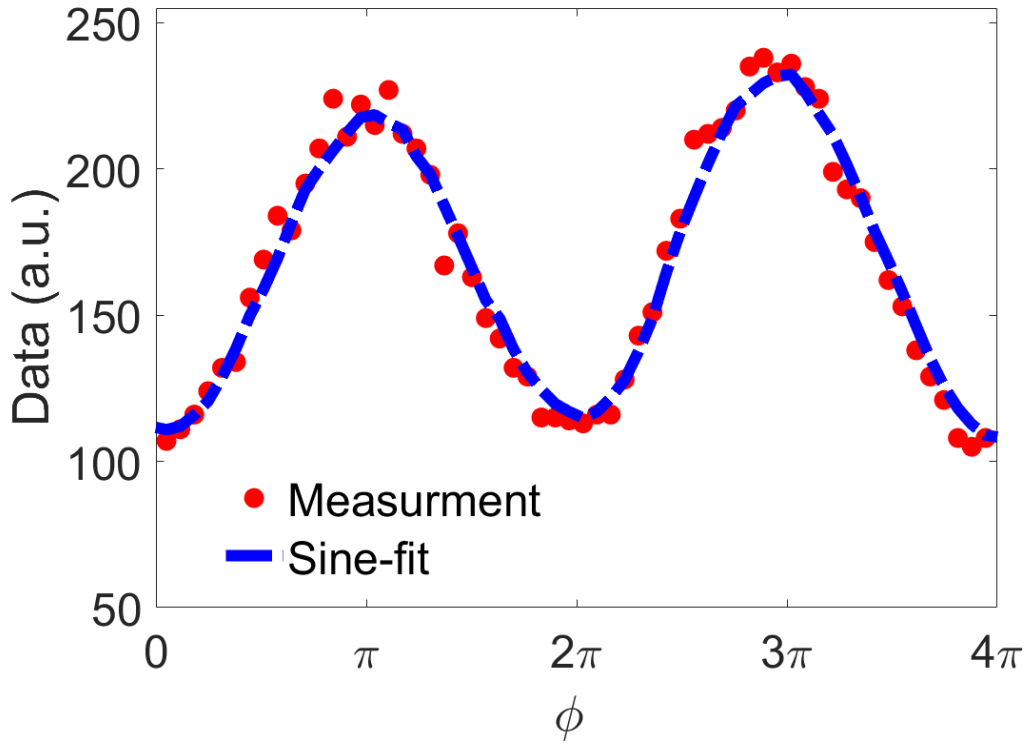

Figure D.1: Data processed from a linear cross-section of two fringes and fitted with a sinusoidal curve.

(i.e., removing/shuttering the source after 1 second) and recorded the fringe images in our CMOS camera. The frame rate of the camera was kept at 30 Hz; therefore, the Nyquist condition was satisfied. Through programming in MATLAB, we tracked the peak of one sinusoidal period from the fringe images, which provides the phase shift measurements due to ΔT of 101 mK. Fig.D.3 presents the tracking of the peak of a sinusoidal period. Although there are over 30 measurement points, only 5 points are highlighted to portray the shift properly. It can be observed that the overall normalized phase shift $\Delta\phi/2\pi$ is $\sim$1.1 (i.e., $\Delta\phi$ $\sim$2.2π) with ΔT=101 mK. By analyzing three different data sets for the same ΔT, the average normalized phase shift was found as $\sim$1.12 (i.e., $\Delta\phi$ $\sim$2.24π), with a root mean square (RMS) error of $\sim$13%.

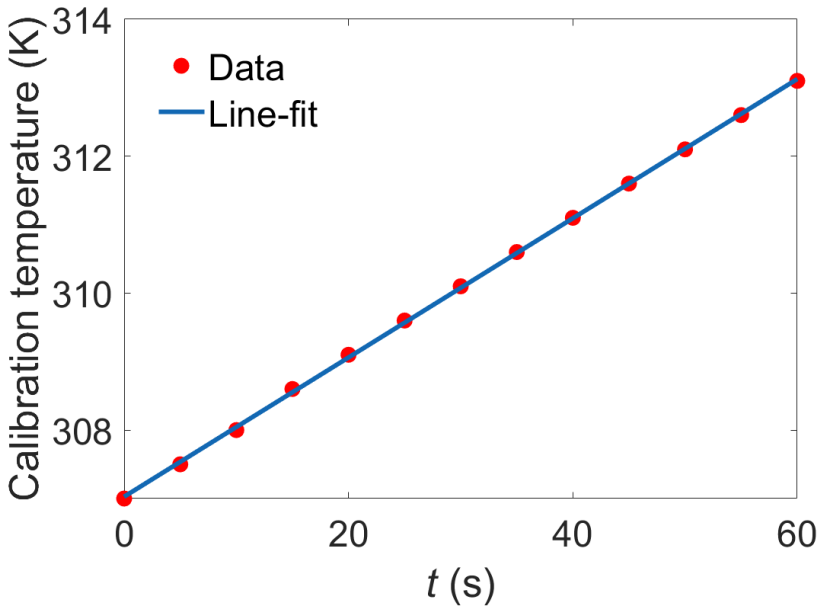

Figure D.2: Calibration of the IR source over 60 s time duration.

D.0.2 Responsivity and NEP

Table D.1 presents the linear and angular responsivities, i.e., $\Re_v$ and $\Re_\gamma$ calculated from experimental measurements of phase shifts (ϕ) due to thermal excitation of 101 mK. The phase shifts were measured at different modulation frequencies. All the equations are presented in the "Analysis of responsivity" section in Chapter5.

Fig. D.4 shows the measurements of noise equivalent power with different modulation frequencies.

D.0.3 Optical indices of materials

Fig. D.5 presents the optical constants i.e., refractive index n and absorption coefficient k of Ti, SiN_x, Ni, and Au used in theoretical analysis.

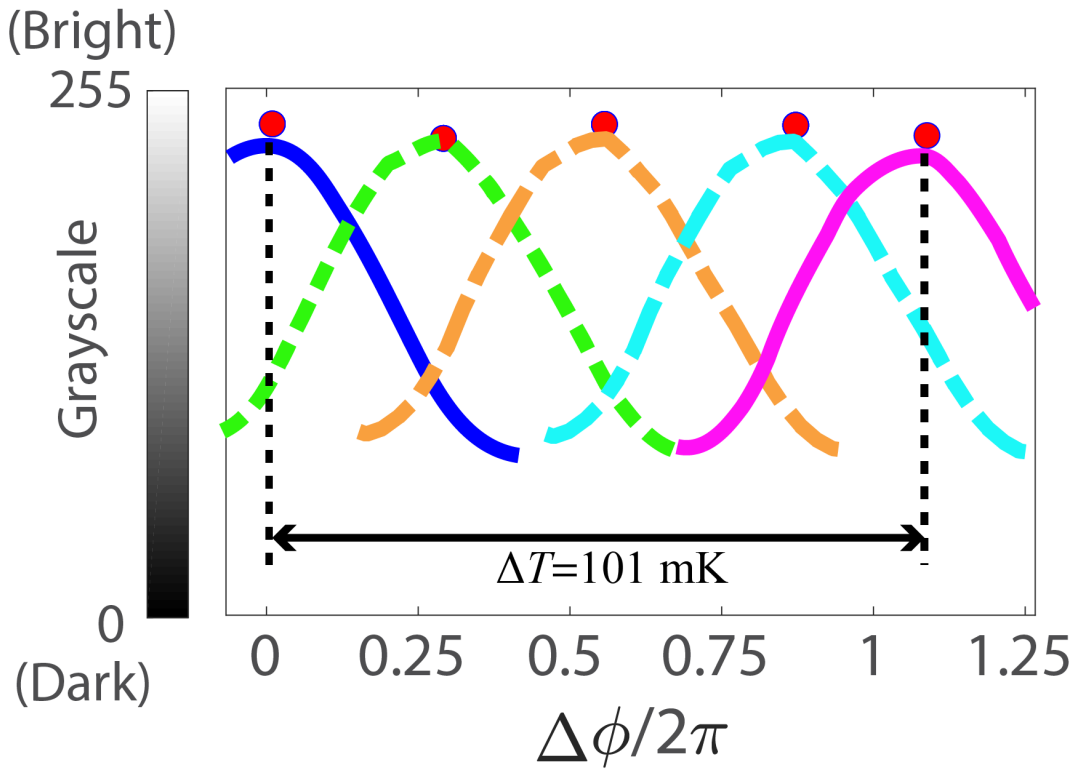

Figure D.3: Tracking of the peak of a sinusoidal period due to a thermal excitation ΔT of 101 mK, which corresponds to an overall phase shift of $\sim 2.2\pi$ (i.e., $\Delta\phi/2\pi$ $\sim$1.1). Please note that there are over 30 measurement points, we highlighted 5 points to portray the shift properly.

Table D.1: Linear and angular responsivity from experimental data

Modulation frequency (Hz)	**Phase shift ($\phi/2\pi$)**	**Angular deflection (deg)**	**Linear deflection (nm)**	$\Re_\gamma$ **(deg/W)**	$\Re_v$ **(m/W)**
10	1.1	0.252	88	6.8×10^9	2371.8
30	0.45	0.103	36	2.8×10^9	970.3
50	0.27	0.062	21.6	1.7×10^9	582.2
100	0.136	0.031	10.9	0.8×10^9	293.8
200	0.09	0.021	7.2	0.6×10^9	194.06

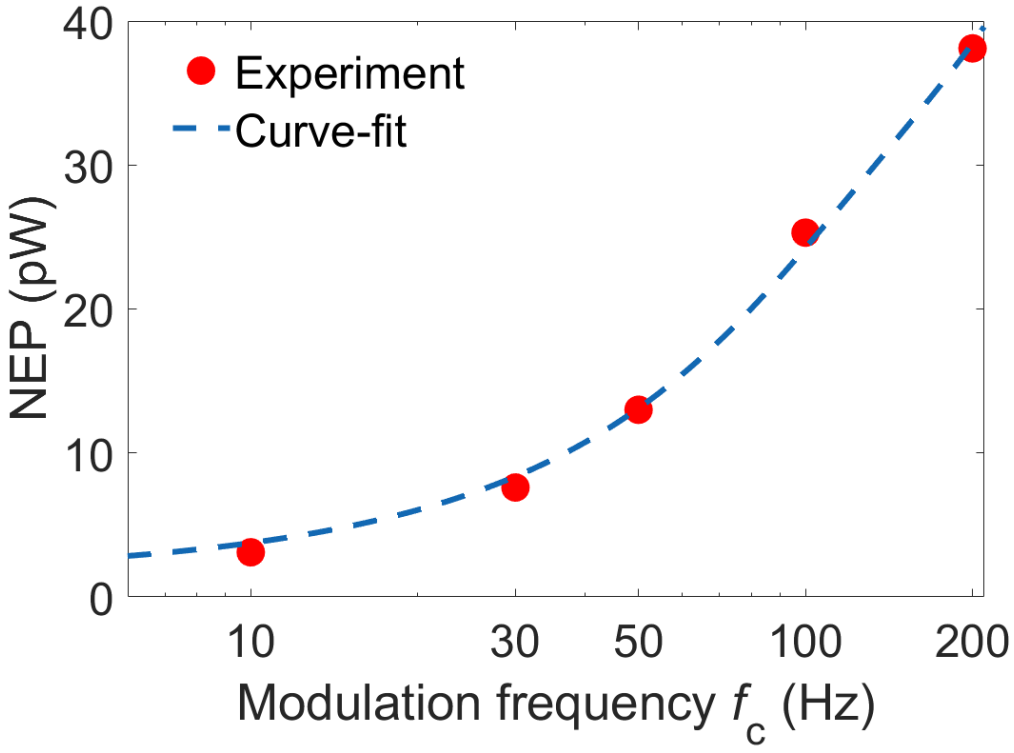

Figure D.4: Experimental measurements of noise equivalent power (NEP) with different modulation frequencies.

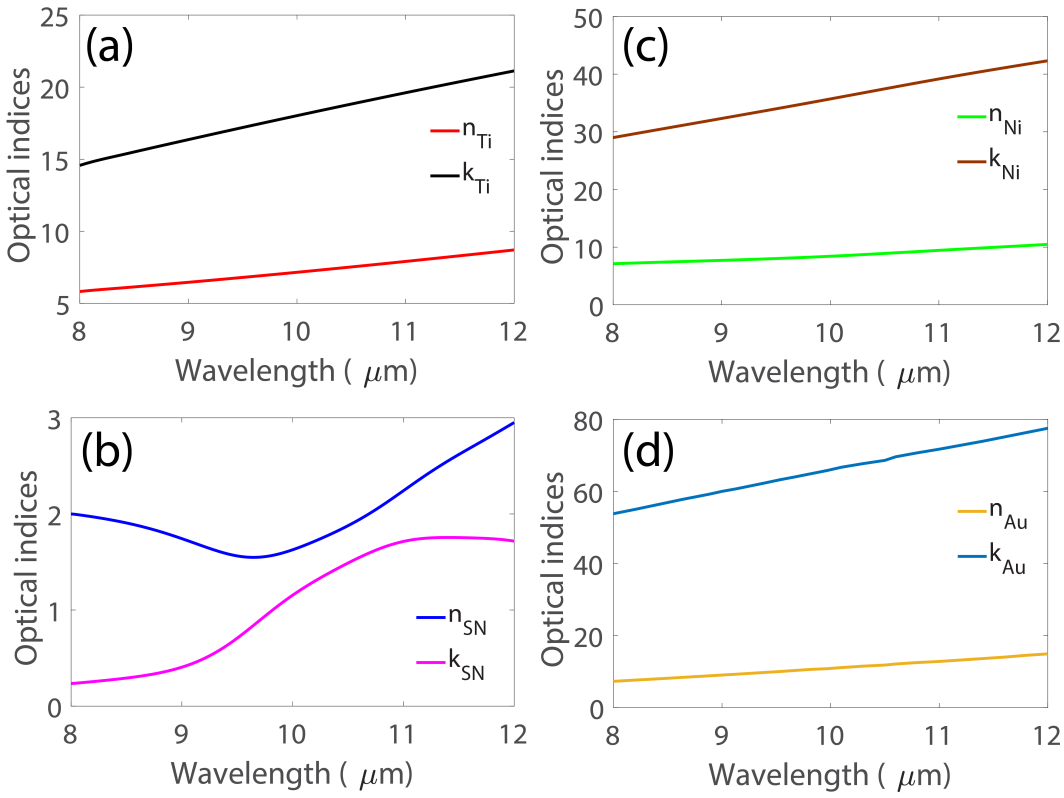

Figure D.5: Refractive index and absorption coefficient of (a) Ti, (b) SiN_x, (c) Ni, and (d) Au in the LWIR, i.e., 8-12 μm.